Search for Supersymmetric Particles from VBF-like processes with two Tau-Leptons with same sign charges at CMS

Dissertation

zur Erlangung des Doktorgrades

des Departement Physik der Universität Hamburg

vorgelegt von

Daniele Marconi

Hamburg

2017

Tag der Disputation 02. März 2018

Gutachter der Dissertation:	Dr. Christian Sander
	Prof. Dr. Peter Schleper
Gutachter der Disputation:	Dr. Christian Sander
	Prof. Dr. Peter Schleper
	Prof. Dr. Dieter Horns
	Prof. Dr. Gudrid Moortgat-Pick
	Dr. Isabell Melzer-Pellmann

Abstract

Despite the Standard Model's success in describing subnuclear phenomena over the last decades, it is not a complete theory of particle physics. Many theories have been formulated in order to address the issues of this model. Among them, Supersymmetry has the potential to link gravity with the other fundamental forces of nature by proposing a relationship between two basic classes of elementary particles: bosons and fermions. Under Supersymmetry, each particle from one group has an associated particle in the other, called its superpartner, the spin of which differs by a half-integer. These superpartners would be new and undiscovered particles.

This thesis presents one of the first searches for supersymmetry in the vector-boson fusion topology. The search targets final states with at least two hadronically decaying tau leptons, large missing transverse momentum, and two jets with a large separation in pseudo-rapidity. The data sample corresponds to an integrated luminosity of 19.7 fb^{-1} of proton-proton collisions at a center-of-mass energy of 8 TeV collected with the CMS detector at the CERN LHC. The observed di-jet invariant mass spectrum is found to be consistent with the expected standard model prediction. Upper limits are set on the cross sections for chargino and neutralino production with two associated jets, assuming the supersymmetric partner of the tau lepton to be the lightest slepton and the lightest slepton to be lighter than the charginos.

The second part of this thesis gives an outlook into the possible analysis strategies for the second phase of data taking. A sensitivity study is performed using 13 TeV simulated data and an integrated luminosity of 85 fb^{-1} with the aim of establishing the most optimal and realistic event selection.

Abriss

Trotz des großen Erfolgs des Standardmodells bei der Beschreibung subatomare Phänomene ist es keine vollständige Theorie der Teilchenphysik. Viele neue Theorien wurden formuliert mit dem Ziel, Lsungsansätze für dessen Mängel zu bieten. Eine dieser neuen Theorien, Supersymmetrie, hat das Potential eine Verbindung zwischen der Gravitation und den anderen fundamentalen Kräften der Natur herzustellen, indem ein Zusammenhang zwischen zwei Arten von Elementarteilchen, Fermionen und Bosonen, eingeführt wird. Dieser Zusammenhang besteht darin, dass jedes Teilchen aus der einen Gruppe mit einem sogenannten Superpartner aus der anderen Gruppe assoziiert ist, dessen Spin sich um eine Halbzahl unterscheiden.

Diese Arbeit beschreibt eine der ersten Suchen nach Supersymmetrie, die im Kanal mit Vektor-Boson-Fusion durchgeführt wurde. Die Suche zielt auf Endzustände ab, bei denen mindestens zwei hadronisch zerfallenden Tau-Leptonen, hoher fehlender Transversalimpuls und zwei Jets mit großem räumlichen Abstand bzgl. der Pseudo-Rapidität vorhanden sind. Der verwendete Datensatz entspricht einer integrieren Luminosität von 19.7 fb^{-1}, der bei Proton-Proton-Kollisionen mit einer Schwerpunktsenergien von 8 TeV am CMS-Detektors am LHC gesammelt wurde. Die beobachtete Verteilung der Di-Jet-Masse ist konsistent mit der erwarteten Vorhersage durch das Standardmodell. Folglich wurden Ausschlussgrenzen auf den Wirkungsquerschnitt der Chargino- und Neutralino-Produktion in Assoziation mit Jets gesetzt, unter der Vorraussetzung, dass der supersymmetrische Partner des Tau-Leptons das leichteste Slepton ist und dieses wiederum leichter als die Charginos ist.

Der zweite Teil dieser Arbei gibt einen Ausblick in die möglichen Analysestrategien für eine zweite Phase in der Datennahme bei einer Schwerpunktsenergie von 13 TeV. Basierend auf einem simulierten Datensatz von 85 fb^{-1} wurde eine Sensitivitätsstudie durchgeführt, die das Ziel hat eine optimale und realistische Selektion von Ereignissen zu studieren.

Contents

1 Introduction

The Standard Model of particle physics synthesizes our current understanding of nature [1]. For decades, this model has managed to predict and lead to the discovery of several elementary particles and has provided a guiding framework for the experimental and theoretical scientific communities.

Even after the many successful discoveries, most recently that of the Higgs Boson discovered in 2012 at the Large Hadron Collider [2,3], the Standard Model is not considered the final theory of particle physics. First of all, the theory is not complete. For example, it incorporates neither general relativity nor neutrino oscillations, and does not provide a dark matter candidate. Furthermore, the Standard Model suffers from a variety of problems. One of the most significant ones is the so-called hierarchy problem and relates to the Higgs boson mass, whitch has been measured at a value of around 125 GeV and is considered very low regarding the huge radiative corrections at the Planck scale ($\approx 10^{19}$ GeV). Many of these defects and tensions motivate both theoretical and experimental physicists to formulate theories beyond the Standard Model. One model in particular tries to solve the above mentioned problems through a new symmetry into the Lagrangian formulation of particle physics, a so-called supersymmetry (SUSY). This symmetry relates bosons and fermions by new fermionic generators and leads to the prediction of a supersymmetric partner particle for each of the particles contained in the Standard Model. If the new particles have mass near the electroweak scale, then this would lead to very drastic phenomenological implications. A very large number of searches has been performed over the last decays in many high energy physics experiment.

With the successful operation of the Large Hadron Collider, numerous results placing constraints on extensions to the Standard Model have been established by the ATLAS and CMS experiments. In particular, in SUSY models, limits in excess of 1 TeV have been placed on the masses of the strongly produced gluinos and first and second generation squarks. In contrast, mass limits on the weakly produced charginos ($\tilde{\chi}_1^{\pm}$) and neutralinos ($\tilde{\chi}_2^0$), with much smaller production cross sections, are much less severe. The limits for charginos and neutralinos are especially weak in so-called compressed mass spectra, in which the mass of the lightest supersymmetric particle (LSP) is only slightly less than the masses of other SUSY states. The chargino-neutralino sector plays a crucial role in the connection between dark matter and SUSY: in SUSY models with R-parity conservation, the lightest neutralino $\tilde{\chi}_1^0$ often takes the role of the LSP and is a dark matter candidate. Several searches on the chargino/neutralino system have been performed and showed a limited sensitivity in case the $\tilde{\chi}_1^{\pm}$ and $\tilde{\chi}_1^0$ are nearly mass degenerate. Electroweak SUSY particles can be also produced in pairs along with two jets in in pure electroweak processes through vector-boson-fusion. This topology is characterized by the presence of two forward jets, in opposite hemispheres of the detector, leading to a large dijet invariant mass (m_{jj}). A search in the VBF topology offers a new and complementary mean to directly probe the electroweak sector of SUSY, especially in compressed-mass-spectrum scenarios.

After an introduction to the theoretical and experimental background, this PhD thesis presents two different studies. The first part consist in a search for supersymmetric par-

ticles using 19.7 fb^{-1} of proton-proton collision data, collected in the year 2012 at 8 TeV of center-of-mass energy at the CMS detector. The second part shows a sensitivity and limit setting study performed with 85 fb^{-1} of simulated data at 13 TeV.

2 Theory

This chapter covers the theoretical background for the research presented in this thesis. Starting with the description of the Standard Model, this chapter will analyze its limits and introduce one possible theoretical extension, supersymmetry. This additional theory can explain some of the phenomena in nature that the Standard Model cannot describe.

2.1 The Standard Model

The Standard Model is a gauge theory with the gauge group $SU(3)_{\mathrm{c}} \otimes SU(2)_{\mathrm{L}} \otimes U(1)_Y$ in which color charge, weak isospin (T_3) , electric charge (Q), and weak hypercharge are conserved. This theory also describes three of the forces existing in nature, the electromagnetic, the weak and the strong force and defines the fundamental constituents of matter [1]. It was developed in the second half of the twentieth century as combined theoretical and experimental effort by the international research communities. Since the first formulation at the beginning of the 1970s the Standard Model successfully predicted all the particles that were discovered later throughout the decades. The most recent particle discoveries such as the top quark [4] (1995), the tauonic neutrino [5] and finally the Higgs boson [2, 3](2012) have given further credence to the Standard Model.

According to this theoretical model the basic constituents of matter are the fermions, characterized by Fermi-Dirac statistics. Fermions include leptons and quarks, which are divided into three generations of identical structure and are of half integer spin. Figure 2.1 shows all the fermions of the Standard Model and their charges, arranged in the three generations. Bosons are characterized by Bose-Einstein statistics and all have integer spins. Bosons may be either elementary, like photons and gluons, or composite, like mesons. Elementary bosons are responsible for the fundamental forces of nature and are called force particles (gauge bosons). As shown in Table 2.1 the strong interaction is mediated by the gluon g, the weak interaction is mediated by the W and Z bosons, the electromagnetic force is mediated by the photon γ.

2.1.1 Standard Model limitations

Over the decades the Standard Model has been successful in predicting existence of particles and their properties at the electroweak scale. However several questions remain open:

- The Standard Model does not include gravity, therefore it cannot be a complete description of nature;
- Although the representation of the strong and electroweak force by $SU(2)_L \otimes U(1)_Y \rightarrow U(1)_{EM}$ is successful, the Standard Model does not have the unification of the force coupling constants at a high energy scale.

	1st Generation	2nd Generation	3rd Generation	interaction
leptons	$\begin{pmatrix} \nu_e \\ e \end{pmatrix}_{\mathrm{L}}$	$\begin{pmatrix} \nu_\mu \\ \mu \end{pmatrix}_{\mathrm{L}}$	$\begin{pmatrix} \nu_\tau \\ \tau \end{pmatrix}_{\mathrm{L}}$	weak weak, electromagnetic
	e_{R}	μ_{R}	τ_{R}	electromagnetic
quarks	$\begin{pmatrix} u \\ d \end{pmatrix}_{\mathrm{L}}$	$\begin{pmatrix} c \\ s \end{pmatrix}_{\mathrm{L}}$	$\begin{pmatrix} t \\ b \end{pmatrix}_{\mathrm{L}}$	weak, electromagnetic, strong
	$u_{\mathrm{R}}, d_{\mathrm{R}}$	$c_{\mathrm{R}}, s_{\mathrm{R}}$	$t_{\mathrm{R}}, b_{\mathrm{R}}$	electromagnetic, strong

Figure 2.1: Fermions of the Standard Model and their interactions, arranged in the three generations. Only the left-handed fermions interact weakly and are arranged in doublets. The right-handed fermions are singlets. The right-handed neutrinos are not present in this table, as they do not interact with one of the forces of the Standard Model and are not a part of it.

bosons	interaction	range [m]	spin [$\hbar$]	Q [e]	mass [GeV/c^2]
8 gluons	strong	10^{-15}	1	0	0
$W^{\pm}$, Z	weak	10^{-18}	1	± 1, 0	$\approx$ 80.4, 91.2
photon γ	electromagnetic	∞	1	0	0
higgs h	–	–	0	0	$\approx$ 125

Table 2.1: The twelve gauge bosons or force carriers of the Standard Model and the corresponding force and force range, and the Higgs field vacuum expectation value $\langle v \rangle \neq 0$ which breaks the electroweak symmetry [6]. The graviton, which is not included in the Standard Model and hence not included here, is a hypothetical spin-2, zero mass, zero electromagnetic charge, and infinite-range mediator of the gravitational force.

- Astrophysical observations give evidence to the existence of a much greater amount of matter in the universe that can be explained by baryonic matter [7], known also under the name of *dark matter*. There are theoretical models that associate the Standard Model neutrinos with "hot Dark Matter" [8], however experimental observations are more consistent with "cold Dark Matter" models which have a non-Standard Model particle candidate [9].
- Neutrinos are considered massless in the Standard Model. Studies over neutrino oscillations prove that neutrinos have masses [10];
- In the Standard Model, the quantum corrections to the Higgs mass are quadratically divergent. Unless explicitly forbidden by a given symmetry, every form of interaction possible by a particle will happen and will contribute to the total mass of the particle.

Therefore the mass of the Higgs boson is

$$\mu_{\text{eff}}^2 = \mu_0^2 + \delta\mu_0^2 \approx 125 \text{ GeV} \tag{2.1}$$

where μ_0^2 is the bare mass of the particle, and $\delta\mu_0^2$ is its total correction. Taking into account the assumption that Standard Model is correct up to the Plank scale, the total correction would be of the order $\delta\mu_0^2 \sim \Lambda^2 \sim M_{\text{Planck}}^2 \sim 10^{28} M_{\text{EW}}^2$ requiring huge cancellation terms to explain the observed Higgs boson mass of around 125 GeV by the experiments ATLAS [2] and CMS [3]. This conceptual problem is the so-called the *Hierarchy Problem*.

2.2 Supersymmetry

Supersymmetry is one of the most intriguing and fundamental concepts in modern theoretical particle physics. It arises naturally from the combination of the two cornerstones of 20th century physics: quantum field theory and relativity [11]. Supersymmetry is the unique symmetry that relates the two fundamental kinds of particles: bosons, which act as the carriers of forces, and fermions, which act as the constituents of matter. Supersymmetric quantum field theories have very special, improved properties, compared to ordinary relativistic quantum field theories. If supersymmetry is realized in nature, every fermion in the SM must have a bosonic partner particle. No such superpartner particle has been observed so far and nowadays the chances for a discovery at the LHC are getting smaller [12].

The most important aspect of supersymmetry is the transformation that turns a bosonic state into a fermionic state, and vice versa. The operator responsible for the transformation Q must be an anti-commuting spinor with:

$$Q\,|\text{Bosons}\rangle = |\text{Fermions}\rangle\,, \quad Q\,|\text{Fermions}\rangle = |\text{Bosons}\rangle\,. \tag{2.2}$$

Supersymmetry is defined as a space-time symmetry given that the Q and $Q^\dagger$ conserve spin and angular momentum. The supersymmetric generator also commutes with the gauge transformation generators, therefore each of the Standard Model particle and its superpartner have the same electric charges, weak isospin, and color degrees of freedom. Each supermultiplet also contains an equal number of fermionic and bosonic degrees of freedom [13].

2.2.1 Particle content

In the supersymmetric extension of the Standard Model each of the known fundamental particles belongs to a chiral or gauge multiplet, and has a superpartner with spin differing by 1/2. The way particles fit into multiplets starts with observing that only chiral supermultiplets can contain fermions for the reason that their left-handed parts transform differently under the gauge group rules than their right-handed parts. All of the Standard Model fermions have those transformation properties, therefore they are members of chiral supermultiplets. On the other hand their superpartners must be spin 0 and not spin 1 vector bosons [13].

The names for the spin-0 superpartners are constructed by adding the letter *s*, as scalar, at the beginning of the fermion names. So generically they are called squark and sleptons (short form for *scalar quark* and *scalar lepton*). Each of the two-component Weyl fermions has its own scalar partner. The symbol convention for squarks and sleptons is the same as the corresponding fermion with the addition of the tilde ($\sim$) symbol, e.g. $\widetilde{e}$ for the selectron. It is very important to denote that a sfermion given "handedness" does not refer to its helicity, being a spin-0 particle, but to its superpartner helicity. A similar nomenclature is applied to smuons and staus: $\widetilde{\mu}_L$, $\widetilde{\mu}_R$, $\widetilde{\tau}_L$, $\widetilde{\tau}_R$. The Standard Model neutrinos are always left-handed and their superpartners are generically denoted as $\widetilde{\nu}$. The gauge interactions of squarks and sleptons are the same as for the corresponding Standard Model fermions; for instance the left handed squarks $\widetilde{u}_L$ and $\widetilde{d}_L$ couple to the W bosons, while $\widetilde{u}_R$ and $\widetilde{d}_R$ don't.

The Higgs boson is a spin-0 particle, so it must reside in a chiral supermultiplet. However, with the presence of a single Higgs boson in the supermultiplet the electroweak gauge symmetry would suffer a gauge anomaly, and would be inconsistent as a quantum theory. The conditions for the cancellations of this anomaly include the matrix trace $\mathrm{Tr}[\mathrm{T}_3^2\mathrm{Y}] = \mathrm{Tr}[\mathrm{Y}_3] = 0$, where T_3 and Y are the third component of weak isospin and the weak hypercharge, respectively, in a normalization where the ordinary electric charge is $Q = T_3 + Y$. In the Standard Model, these conditions are already satisfied by the known quarks and leptons. The fermionic partner of a Higgs chiral supermultiplet has to be a weak isodoublet with weak hypercharge of $Y = \pm 1/2$. In both cases such fermion would give a non-zero contribution to the traces and consequently spoil the anomaly cancellation. This can however be avoided by imposing two Higgs supermultiplets, one with each of $Y = \pm 1/2$, so that they cancel each other's contribution to the traces out. Another reason to justify the existence of two Higgs boson chiral multiplets is the structure of the supersymmetric theory itself: only the $Y = +1/2$ Higgs chiral supermultiplet can have the Yukawa couplings necessary to give masses to charge $+2/3$ up-type quarks (up, charm, top), and only a $Y = -1/2$ Higgs can have the Yukawa couplings necessary to give masses to charge $-1/3$ down-type quarks (down, strange, bottom) and to the charged leptons.

The $\mathrm{SU}(2)_L$ scalar fields are defined as $\mathrm{H}_u(Y = +1/2)$ and $\mathrm{H}_d(Y = -1/2)$. The weak isospin components of H_u with $T_3 = (1/2, -1/2)$ have electric charges 1 and 0 respectively, and are denoted (H_u^+, H_u^0). Similarly, the remaining doublet H_d has $T_3 = (1/2, -1/2)$ components (H_d^0, H_d^-). The lightest CP-violating Higgs has Standard Model-like properties, within the limit of the decoupling. The standard nomenclature for a spin 1/2 superpartner is to add the suffix "-ino" to the name of the original Standard Model particle, e.g. the fermionic partners of the Higgs Scalars are called higgsinos. They are defined as $\widetilde{H}_u$, $\widetilde{H}_d$ for the $\mathrm{SU}(2)_\mathrm{L}$-doublet left-handed Weyl spinor fields, with weak isospin components $\widetilde{H}_u^+$,$\widetilde{H}_u^0$ and H_d^0,$\widetilde{H}_d^-$.

All the chiral multiplets are summarized in Table 2.2, classified according to their transformation properties under the Standard Model gauge group $\mathrm{SU}(3)_C \times \mathrm{SU}(2)_L \times \mathrm{U}(1)_Y$.

chiral supermultiplets		spin 0	spin 1/2	$\mathrm{SU}(3)_\mathrm{c}$, $\mathrm{SU}(3)_\mathrm{L}$, $\mathrm{U}(1)_\mathrm{Y}$
squarks, quarks (3 families)	Q	$(\widetilde{u}_\mathrm{L},\ \widetilde{d}_\mathrm{L})$	$(u_\mathrm{L},\ d_\mathrm{L})$	**3**, **2**, 1/3
	$\bar{u}$	$\widetilde{\bar{u}}_\mathrm{L}$ $(\widetilde{u}_\mathrm{R}^*)$	$\bar{u}_\mathrm{L} \sim (u_\mathrm{R})_\mathrm{c}$	$\bar{\mathbf{3}}$, **1**, -4/3
	$\bar{d}$	$\widetilde{\bar{d}}_\mathrm{L}$ $(\widetilde{d}_\mathrm{R}^*)$	$\bar{d}_\mathrm{L} \sim (d_\mathrm{R})_\mathrm{c}$	$\bar{\mathbf{3}}$, **1**, 2/3
sleptons (3 families)	L	$(\widetilde{\nu}_{e\mathrm{L}},\ \widetilde{e}_\mathrm{L})$	$(\nu_\mathrm{L},\ e_\mathrm{L})$	**1**, **2**, -1
	$\bar{e}$	$\widetilde{\bar{e}}_\mathrm{L}$ $(\widetilde{e}_\mathrm{R}^*)$	$\bar{e}_\mathrm{L} \sim (e_\mathrm{R})_\mathrm{c}$	**1**, **1**, 2
higgs, higgsinos	H_u	$\left(H_\mathrm{u}^+,\ H_\mathrm{u}^0\right)$	$\left(\widetilde{H}_\mathrm{u}^+,\ \widetilde{H}_\mathrm{u}^0\right)$	**1**, **2**, 1
	H_d	$\left(H_\mathrm{d}^0,\ H_\mathrm{d}^-\right)$	$\left(\widetilde{H}_\mathrm{d}^0,\ \widetilde{H}_\mathrm{d}^-\right)$	**1**, **2**, -1

Table 2.2: Chiral supermultiplets in the Minimal Supersymmetric Standard Model. The spin-0 fields are complex scalars, and the spin-1/2 fields are left-handed two-component Weyl fermions. The right-handed neutrinos superpartners are not

The vector bosons of the Standard Model belong to the so called gauge multiplets. Their fermionic superpartners are called gauginos. In the Standard Model the color gauge interactions are mediated by the gluon g, whose spin-1/2 superpartner is the gluino $\widetilde{g}$. The electroweak symmetry breaking is associated with the $\mathrm{W}^\pm$, W^0 and γ bosons, whose

superpartners are the winos $\widetilde{\mathrm{W}}^{\pm}$, $\widetilde{\mathrm{W}}^{0}$ and bino $\widetilde{\mathrm{B}}^{0}$.

Table 2.3 summarizes the gauge supermultiplets of a minimal supersymmetric extension of the Standard Model. From the mixing of the neutral gauginos $\widetilde{\mathrm{W}}^{0}$ and $\widetilde{\mathrm{B}}^{0}$ and higgsinos $\widetilde{\mathrm{H}}_u^0$ and $\widetilde{\mathrm{H}}_d^0$ come the four neutralinos $\widetilde{\chi}_i^0$ with $i \in 1, 2, 3, 4$. Neutralinos couple to the gauge bosons, allowing for example a neutralino pair production through Drell-Yan processes. The mixing of the charged gauge bosons $\widetilde{\mathrm{W}}^{\pm}$ and higgsinos $\widetilde{H}_u^+$ and $\widetilde{H}_d^-$ creates the four charginos $\widetilde{\chi}_i^+$ and $\widetilde{\chi}_i^-$ with $i \in 1, 2$. Because these particles are mixed states of other particles, if a particle is dominantly one of the states, one could call it like that particle state. Bino-like and higgsino-like describe similar situations for particles consisting of mixed states that are largely bino and higgsinos, respectively, for example, a neutralino can be winolike if its mixed state comes mostly from the wino.

gauge supermultiplets	spin 1/2	spin 1	$\mathrm{SU(3)_c}$, $\mathrm{SU(3)_L}$, $\mathrm{U(1)_Y}$
gluinos, gluons	$\widetilde{g}$	g	**8**, **1**, 0
winos, W bosons	$\widetilde{W}^{\pm}$, $\widetilde{W}^{0}$	$W^{\pm}$, W^{0}	**1**, **3**, 0
bino, B boson	$\widetilde{B}$	B	**1**, **1**, 0

Table 2.3: Gauge supermultiplets in the Minimal Supersymmetric Standard Model.

2.2.2 The MSSM

The chiral and gauge supermultiplets in Tables 2.2 and 2.3 constitute the particle content of a model of SUSY called Minimal Supersymmetric Standard Model (MSSM). Up to now none of the superpartners of the Standard Model has been discovered. If supersymmetry is unbroken, then all the sparticles would be extremely easy to detect; there would have to be for example selectrons with masses exactly equal to the electron mass. A similar statement can be applied to all the others superpatners of the known Standard Model particles. The experimental evidence collected so far shows clearly that supersymmetry is a broken symmetry in the vacuum state chosen by Nature [13].

Supersymmetry can be broken by introducing extra terms into the Lagrangian that explicitly break the symmetry. A way to break supersymmetry is defined as *soft* [14]: the extra terms should be of positive mass dimension in order to maintain naturally a hierarchy between the electroweak scale and the Planck scale [13]. Soft also means the theory is still renormalizable and the cancellation of quadratic divergences is preserved.

The MSSM is often characterized by the choice of a superpotential which includes all the gauge invariants and renormalizable term, but on the other hand takes into account the softly broken supersymmetry and the conservation of the R-parity.

In supersymmetric processes, the baryon number and the lepton number are not preserved automatically. This would allow the proton to decay, in contrast with the experimental evidence of a lifetime of $> 10^{32}$ years [13]. This theoretical impasse is simply solved by introducing a new quantity, the so-called R-Parity defined as:

$$P_R = (-1)^{3(B-L)+2s} \tag{2.3}$$

where B, L and s are the particle baryonic, lepton number and spin respectively.

Is it possible to rewrite the scalar potential for the MSSM using the Higgs doublets [13]:

$$W_{\mathrm{MSSM}} = \bar{u}\mathbf{y_u}QH_u - \bar{d}\mathbf{y_d}QH_d - \bar{e}\mathbf{y_e}LH_d + \mu H_u H_d. \tag{2.4}$$

The object Q contains the left-handed squark and quark doublets, whereas the objects $\bar{u}$ and $\bar{d}$ contain $\widetilde{u}^*_{\mathrm{R}}$, $u^\dagger_{\mathrm{R}}$ and $\widetilde{d}^*_{\mathrm{R}}$, $d^\dagger_{\mathrm{R}}$, respectively. Similarly L and $\bar{e}$ contain the slepton and lepton $\mathrm{SU}(2)_{\mathrm{L}}$ doublets and singlets, respectively. The Yukawa matrices $\mathbf{y_u}$, $\mathbf{y_d}$, and $\mathbf{y_e}$ are dimensionless coupling parameters in the family space.

The symmetry breaking is exclusively coming from the soft SUSY-breaking terms [13]. The soft MSSM Lagrangian $\mathcal{L}^{\mathrm{MSSM}}_{\mathrm{soft}}$ is built combining the MSSM superpotential shown in Equation 2.4 with the soft breaking terms and finally the kinetic mass terms [13]:

$$\begin{aligned}
\mathcal{L}^{\mathrm{MSSM}}_{\mathrm{soft}} \;=\; & -\frac{1}{2}\left(M_3\widetilde{g}\widetilde{g} + M_2\widetilde{W}\widetilde{W} + M_1\widetilde{B}\widetilde{B} + \mathrm{c.c.}\right) \\
& -\left(\widetilde{\bar{u}}\mathbf{a_u}\widetilde{Q}H_u - \widetilde{\bar{d}}\mathbf{a_d}\widetilde{Q}H_d - \widetilde{\bar{e}}\mathbf{a_e}\widetilde{L}H_d + \mathrm{c.c.}\right) \\
& -\widetilde{Q}^\dagger\mathbf{m^2_Q}\widetilde{Q} - -\widetilde{L}^\dagger\mathbf{m^2_L}\widetilde{L} - \widetilde{\bar{u}}\mathbf{m^2_u}(\widetilde{\bar{u}})^\dagger - \widetilde{\bar{d}}\mathbf{m^2_d}(\widetilde{\bar{d}})^\dagger - \widetilde{\bar{e}}\mathbf{m^2_e}(\widetilde{\bar{e}})^\dagger \\
& -m^2_{H_u}H^*_u H_u - m^2_{H_d}H^*_d H_d - (bH_u H_d + \mathrm{c.c.}).
\end{aligned} \tag{2.5}$$

The Yukawa couplings y_f are replaced by the mass matrices a_f [13]. The parameters M_1, M_2, and M_3 are the bino, wino, and gluino mass terms. Denoting the soft supersymmetry breaking scale as m_{soft} [13], the masses should be of the order of

$$\begin{aligned}
M_1, M_2, M_3, \mathbf{a_u}, \mathbf{a_d}, \mathbf{a_e} &\sim m_{\mathrm{soft}} \\
\mathbf{m^2_Q}, \mathbf{m^2_L}, \mathbf{m^2_{\bar{u}}}, \mathbf{m^2_{\bar{d}}}, \mathbf{m_{\bar{e}}}, m^2_{H_u}, m^2_{H_d}, b &\sim m^2_{\mathrm{soft}},
\end{aligned} \tag{2.6}$$

with the only constraint that m_{soft} should not be much larger than 1000 GeV [13]. The introduction of the symmetry breaking mechanism leads to a model with 105 parameters among which masses, phases, and mixing angles that cannot be rotated away by redefinitions, nor have a counterpart in the Standard Model [15]. MSSM is the benchmark for the construction of further models. The assumptions taken in to account in those model could reduce the total number of parameters.

2.2.3 Motivations

Supersymmetry gives an elegant solution to some of the previously shown problems which the Standard Model fails to explain. The most important are:

- **Dark Matter candidate**: The assumption of R-parity (Equation 2.3) conservation prevents the lightest of the SUSY particles, also called LSP, to decay any further into lighter Standard Model particles. In order to fit into the profile of a Dark Matter candidate this particle cannot interact with matter any further, therefore the best choice for the LSP is the lightest neutralino $\tilde{\chi}^0_1$.
- **Hierarchy problem solution**: the previously mentioned corrections to the Higgs mass are canceled by the superpartners of the Standard Model particles with opposite sign. An example of the top quark correction to the Higgs mass being canceled by a supersymmetric scalar top $\widetilde{t}$ correction is shown in Figure 2.2.

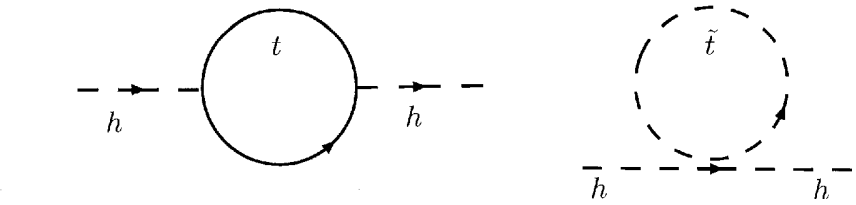

Figure 2.2: In SUSY, the correction to Higgs mass by the top quark (left) is inherently canceled by the contribution from the top quark's supersymmetric partner, the stop (right).

- **Naturalness**: Along with the hierarchy problem solution many scientific observations made during the first run of LHC suggest a supersymmetric theory that more naturally explains the weak scale [16]. A summary of the given SUSY particles mass scales is shown on Figure 2.3.

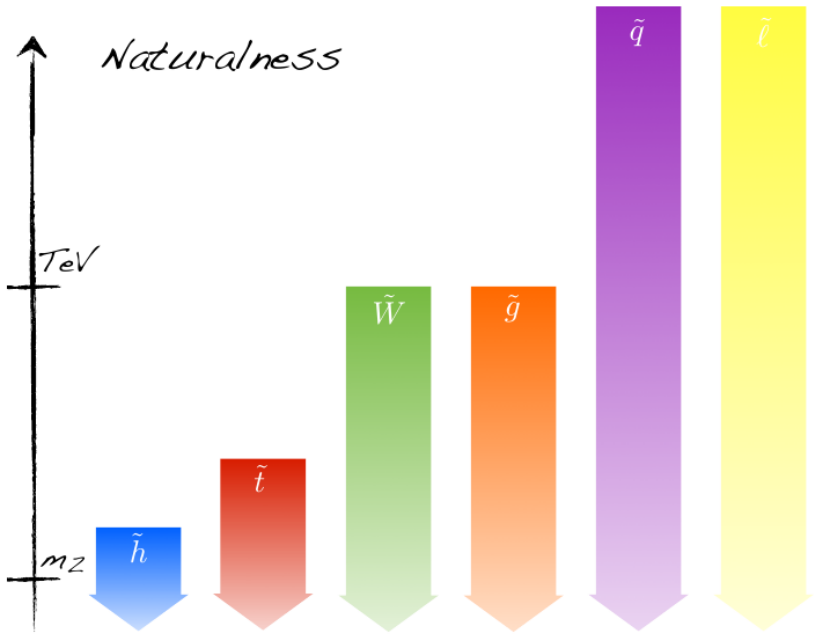

Figure 2.3: Cartoon illustration of the mass scales for various sparticles dictated solely by electroweak naturalness [16].

- **Gravity and forces unifications**: supersymmetric models , for example minimal supergravity (mSUGRA) [17],can take into account a gravity-mediated supersymmetry breaking [13], leading to unification of the gauge couplings at the GUT scale. Those assumptions further reduce the numbers of MSSM parameters.

2.2.4 Phenomenological Minimal Supersymmetric Standard Model

As mentioned before, several other models has been developed starting with the MSSM as an initial benchmark. The Phenomenological Minimal Supersymmetric Standard Model

(pMSSM), among other important ones, takes into account phenomenological constraints in order to significantly reduce the number of free parameters [18]. More than a physics motivated breaking scenarios the pMSSM is a useful parametrization of the possible breaking scenarios. This model reduced the parameter counts to 19 under the following constraints:

1. *No new source of CP violation*: Experimental limits on neutron and electron magnetic moments as well as in the K system are very tight. All phases of the soft SUSY-breaking potential are assumed to be zero so that all new sources of CP-violation are eliminated.

2. *No flavor-changing neutral currents*: Both the matrices for the sfermion masses and the trilinear couplings are assumed diagonal to prevent large violations of flavor-changing neutral current constraints.

3. *First and second generation universality:* Unless squarks are significantly heavier than 1 TeV, the mass splitting between the first- and second-generation squarks is limited by constraints from experimental data on $K^0 - \bar{K}^0$ mixing. The trilinear couplings A^u, A^d, and A^l are always proportional to the Standard Model fermion masses and therefore important only for the much heavier third generation; they can be assumed to be same and even set to zero for the first two generations of squarks without important phenomenological consequences.

This leads to the following 19 parameters for the so-called pMSSM [18]:

- $\tan\beta$: the ratio of the VEVs of the two-Higgs doublet fields;
- M_A: the mass of the pseudoscalar Higgs boson;
- μ: the Higgs-higgsino mass parameter;
- M_1, M_2, M_3: the bino, wino and gluino mass parameters;
- $m_{\widetilde{q}}$, $m_{\widetilde{u}_\mathrm{R}}$, $m_{\widetilde{d}_\mathrm{R}}$, $m_{\widetilde{l}}$, $m_{\widetilde{e}_\mathrm{R}}$: first/second generation sfermion masses;
- $m_{\widetilde{Q}}$, $m_{\widetilde{t}_\mathrm{R}}$, $m_{\widetilde{b}_\mathrm{R}}$, m_L, $m_{\widetilde{\tau}_\mathrm{R}}$: third generation sfermion masses
- A_t, A_b, A_τ: third generation trilinear (scalar^3, proportional to the Yukawa $\propto \mathbf{y_i}$) couplings.

Table 2.4 summarizes the particle content of the pMSSM.

Names	Spin	P_R	Gauge Eigenstates	Mass Eigenstates
Higgs bosons	0	+1	$H_u^0\ H_d^0\ H_u^+\ H_d^-$	$h^0\ H^0\ A^0\ H^\pm$
squarks	0	−1	$\widetilde{u}_L\ \widetilde{u}_R\ \widetilde{d}_L\ \widetilde{d}_R$ $\widetilde{s}_L\ \widetilde{s}_R\ \widetilde{c}_L\ \widetilde{c}_R$ $\widetilde{t}_L\ \widetilde{t}_R\ \widetilde{b}_L\ \widetilde{b}_R$	(same) (same) $\widetilde{t}_1\ \widetilde{t}_2\ \widetilde{b}_1\ \widetilde{b}_2$
sleptons	0	−1	$\widetilde{e}_L\ \widetilde{e}_R\ \widetilde{\nu}_e$ $\widetilde{\mu}_L\ \widetilde{\mu}_R\ \widetilde{\nu}_\mu$ $\widetilde{\tau}_L\ \widetilde{\tau}_R\ \widetilde{\nu}_\tau$	(same) (same) $\widetilde{\tau}_1\ \widetilde{\tau}_2\ \widetilde{\nu}_\tau$
neutralinos	1/2	−1	$\widetilde{B}^0\ \widetilde{W}^0\ \widetilde{H}_u^0\ \widetilde{H}_d^0$	$\widetilde{N}_1\ \widetilde{N}_2\ \widetilde{N}_3\ \widetilde{N}_4$
charginos	1/2	−1	$\widetilde{W}^\pm\ \widetilde{H}_u^+\ \widetilde{H}_d^-$	$\widetilde{C}_1^\pm\ \widetilde{C}_2^\pm$
gluino	1/2	−1	$\widetilde{g}$	(same)
goldstino (gravitino)	1/2 (3/2)	−1	$\widetilde{G}$	(same)

Table 2.4: SUSY particles in pMSSM [13]

2.2.5 SUSY generic signatures at the LHC with charginos and neutralinos

The assumptions made by the most important SUSY models set the mass of the first generation charginos $\tilde{\chi}_1^\pm$ and next-to-lightest neutralino $\tilde{\chi}_2^0$ to values not far from the LSP mass $\tilde{\chi}_1^0$. The possibility of being the first SUSY particles to be discovered puts the spotlight on this topology of SUSY searches in past literature [19].

In case of a mass split between the LSP and next-to-lightest neutralino $\tilde{\chi}_2^0$ or the lightest chargino $\tilde{\chi}_1^\pm$ larger than M_Z or M_W, the particles will decay into massive gauge bosons and the LSP $\tilde{\chi}_1^0$. If not, the decays will occur through virtual gauge boson and scalar fermion exchanges, leading in the final state to the LSP neutralino and a fermion-antifermion pair. It has been realized [20–23] that for large values of the parameter $\tan\beta$, the ratio of the vacuum expectation values of the two doublet Higgs fields which are needed to break the electroweak symmetry in the MSSM, the Yukawa couplings of third generation down-type fermions (b quarks and τ leptons), which are strongly enhanced, lead to dramatic consequences for the decays of these particles. Indeed, the virtual exchanges of, on the one side, Higgs particles (because the Higgs boson couplings to b quarks and τ leptons are proportional to $\tan\beta$) and, on the other side, of third generation down-type sfermions (which tend to be lighter than the other sfermions in this case) become very important.

Many scenarios of those decays has been taken into account considering different SUSY breaking parameters configuration [24].

For example Figure 2.4 shows a couple of the possible Feynman diagrams of $\tilde{\chi}_2^0 \longrightarrow \tilde{\chi}_1^0\tau^+\tau^-$ and $\tilde{\chi}_2^0 \longrightarrow \tilde{\chi}_1^0 b\bar{b}$. Figure 2.5 and Figure 2.6 show, respectively, the branching ratios $\mathrm{BR}(\tilde{\chi}_2^0 \longrightarrow \tilde{\chi}_1^0\tau^+\tau^-)$ and $\mathrm{BR}(\tilde{\chi}_2^0 \longrightarrow \tilde{\chi}_1^0 b\bar{b})$, as functions of $m_{\tilde{\tau}1}$ or $m_{\tilde{b}1}$ for $\mu = 500$ GeV (a), as a function of μ (b) and as a function of $\tan\beta$ (c) for $m_0 = 300$ GeV. There is an evident competition between $b\bar{b}$ and $\tau^+\tau^-$ final states. In the case of a light A boson and for large $\tan\beta$ values, the A and h contributions are much more important in the decay $\tilde{\chi}_2^0 \longrightarrow \tilde{\chi}_1^0 b\bar{b}$ than in the channel $\tilde{\chi}_2^0 \longrightarrow \tilde{\chi}_1^0\tau^+\tau^-$ because of the larger b-

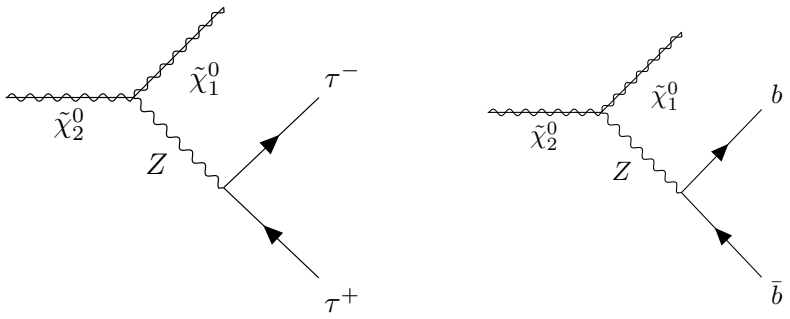

Figure 2.4: The Feynman diagrams contributing to the three-body decays of charginos and neutralinos into the LSP and two fermions

quark mass and the color factor; the Higgs contribution makes then BR($\tilde{\chi}_2^0 \longrightarrow \tilde{\chi}_1^0 b\bar{b}$) dominating, except when $\widetilde{\tau}_1$ is very light, and the two body decay $\tilde{\chi}_2^0 \longrightarrow \tilde{\tau}_1\tau$ is close to occur, making BR($\tilde{\chi}_2^0 \longrightarrow \tilde{\chi}_1^0\tau^+\tau^-$) close to unity. Even for heavy A, and H bosons, BR($\tilde{\chi}_2^0 \longrightarrow \tilde{\chi}_1^0 b\bar{b}$) can reach the level of 50%. However, for large enough values of $\tan\beta$ and μ, it is the decay channel $\tilde{\chi}_2^0 \longrightarrow \tilde{\chi}_1^0\tau^+\tau^-$ which dominates, since the stau is always lighter than the $\widetilde{b}_1$ state and its virtual contribution is larger, despite of the color factor. The sum of the two branching ratios is in general close to unity. According to this study searches for charginos and neutralinos in the di-τ channel are favored for low $\tilde{\tau}_1$ masses and large enough values of $\tan\beta$.

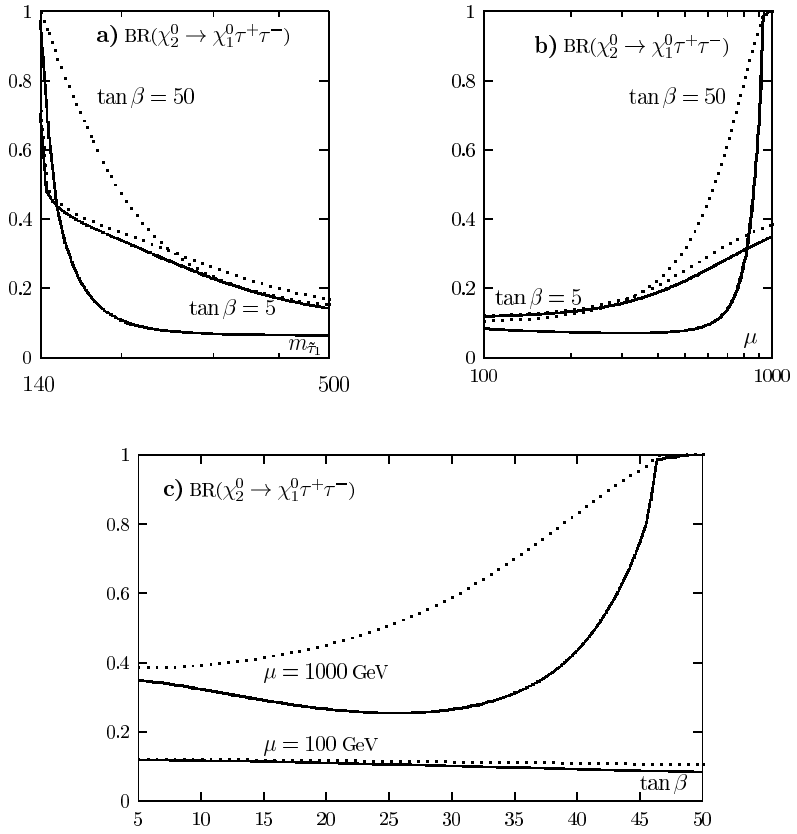

Figure 2.5: The branching ratio BR($\tilde{\chi}_2^0 \longrightarrow \tilde{\chi}_1^0\tau^+\tau^-$) for two values of $\tan\beta = 5$ and 50 and two values of $M_A = 100$ GeV (dashed lines) and 500 GeV (solid lines) as a function of $m_{\tilde{\tau}1}$ for $\mu = 500$ GeV (a) as a function of μ assuming $m_0 = 300$ GeV (b) and as a function of $\tan\beta$ for two values of $\mu = 100$ and 1000 GeV (c); M_2 is fixed to 150 GeV [24].

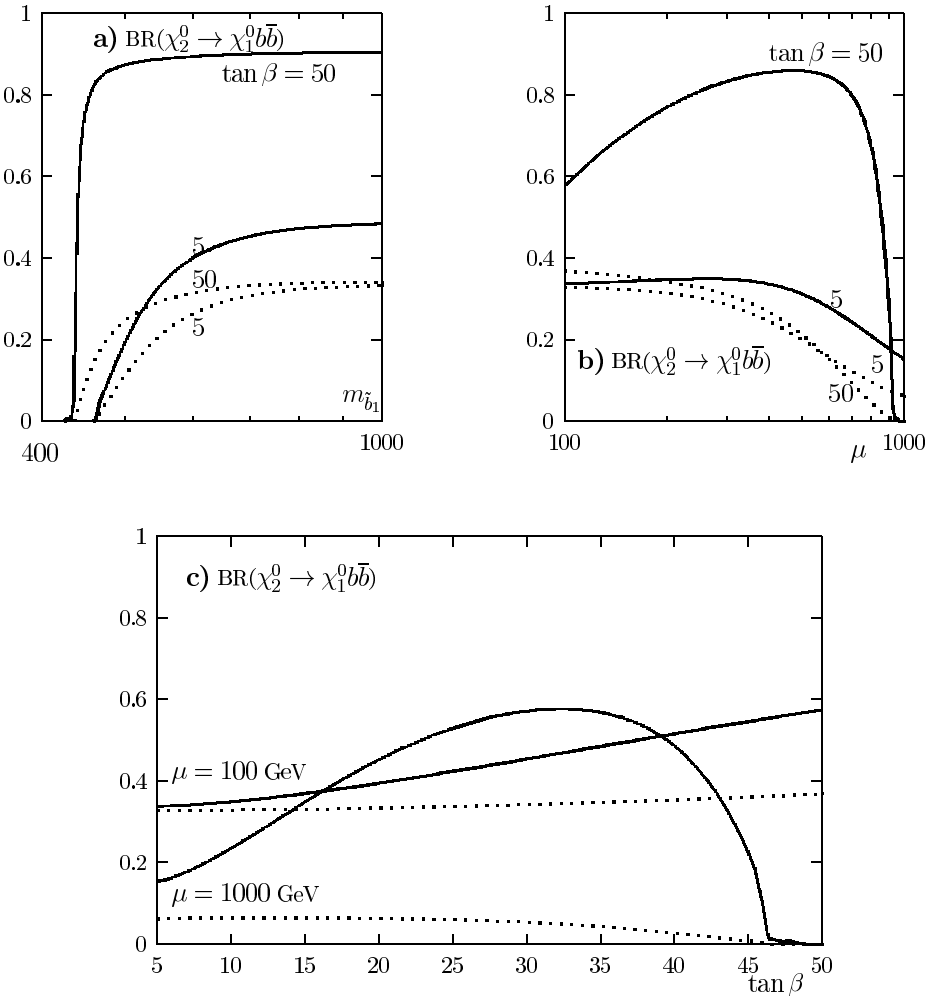

Figure 2.6: The branching ratio BR($\tilde{\chi}_2^0 \longrightarrow \tilde{\chi}_1^0 b\bar{b}$) for two values of $\tan\beta = 5$ and 50 and two values of $M_A = 100$ GeV (solid lines) and 500 GeV (dashed lines) as a function of $m_{\tilde{b}1}$ for $\mu = 500$ GeV (a) as a function of μ assuming $m_0 = 300$ GeV (b) and as a function of $\tan\beta$ for two values of $\mu = 100$ and 1000 GeV (c); M_2 is fixed to 150 GeV [24].

3 The Experimental Setup

3.1 The Large Hadron Collider

The Large Hadron Collider (LHC) is the world's largest and most powerful particle collider [25]. It was built by the European Organization for Nuclear Research (CERN) between 1998 and 2008 in collaboration with scientists and engineers from over 100 countries, as well as hundreds of universities and laboratories. It lies in a tunnel 27 km in circumference and as deep as 175 m beneath the France-Switzerland border near Geneva, Switzerland, which was originally digged for the Large Electron Positron Collider (LEP).

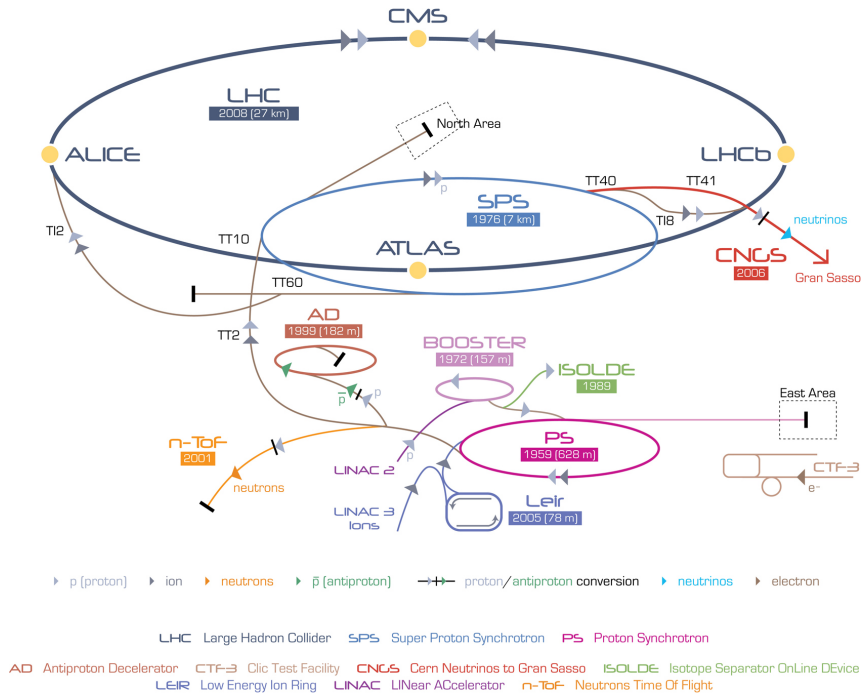

Figure 3.1: Schematic view of the LHC with its four big experiments. Also shown are the pre-accelerators, as well as several other experiments operated at CERN [26].

It is a proton-proton collider and consists of two rings with counter-rotating beams, that intersect each other at four interaction points. The proton beams are ramped up to the energy of 450 GeV by a chain of pre-accelerators, and are then injected into the LHC ring (Figure 3.1). LHC first data taking period, also called *Run1*, started on March 2010 with an initial energy per beam of 3.5 TeV (7 TeV in total), rising to 4 TeV per beam (8 TeV in total) in 2012. The shutdown in 2013 was followed by two years of technical upgrades after which the LHC restarted "*Run2*" with a total center of mass energy of 13 TeV. The design luminosity L is 10^{34} cm^{-2}s^{-1} and has been reached in June 2016, with a bunch crossing taking place every 25ns. Figure 3.2 shows the total cross section prospects for

LHC in comparison with several Standard Model processes. In 2012 LHC delivered a total luminosity of 23.30 fb^{-1} as shown on Figure 3.3. The delivered luminosity accounts for the luminosity delivered from the start of stable beams until the LHC requests CMS to turn off the sensitive detectors to allow a beam dump or beam studies. Given is the luminosity as determined from counting rates measured by the luminosity detectors. These detectors have been calibrated with the use of the van-der-Meer beam-separation method, where the two beams are scanned against each other in the horizontal and vertical planes to measure their overlap function [27].

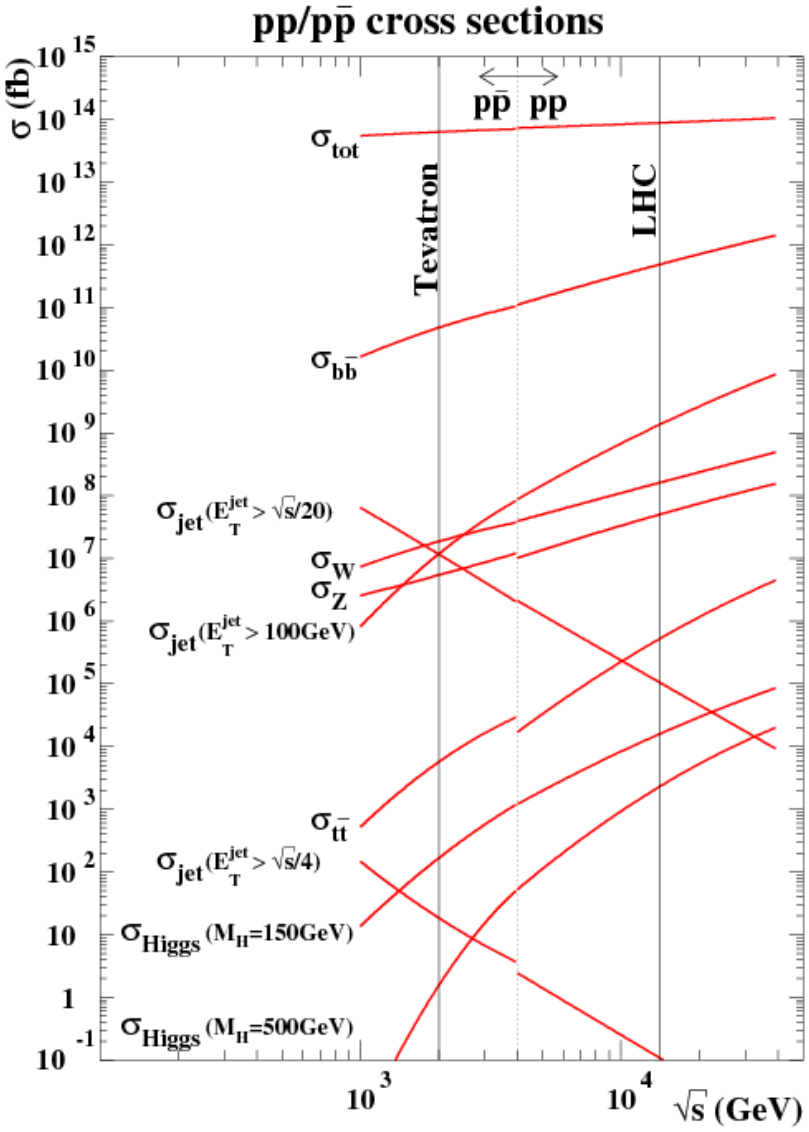

Figure 3.2: Production cross-sections for several representative processes at hadron colliders as a function of the machine's center-of-mass energy [28]

Several experiments are hosted at the LHC. ATLAS (A Toroidal LHC ApparatuS) [29] and CMS (Compact Muon Solenoid) [30] are multi-purpose detectors, aiming at Standard Model physics, Higgs searches, and physics beyond the Standard Model. LHCb [31] is ded-

icated to b-quark physics and the related problem of CP violation the matter-antimatter asymmetry in the universe. As the LHC can also be run in heavy ion (lead-lead) collision mode, one experiment, ALICE (A Large Ion Collider Experiment) [32], focuses on strongly interacting matter and quark-gluon plasma. Finally, another two experiments, LHCf [33] and TOTEM (TOTal Elastic and diffractive cross section Measurement) [34] are designed to study the total proton-proton interaction cross-section. The sites for each of the previously mentioned experiments are shown in Figure 3.1.

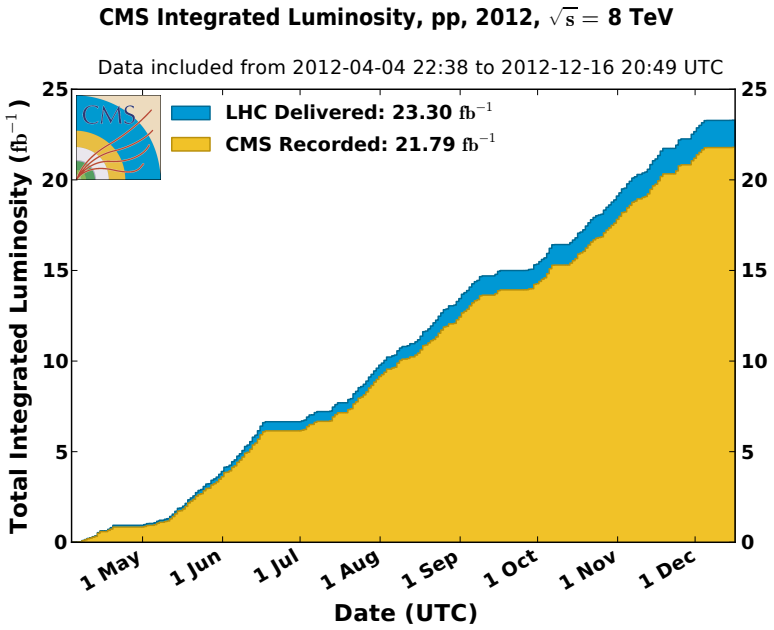

Figure 3.3: Cumulative luminosity as function of time delivered to (blue), and recorded by CMS (orange) during stable beams and for p-p collisions at 8 TeV centre-of-mass energy in 2012 [27].

3.2 The CMS experiment

The Compact Muon Solenoid is a "general purpose" experiment placed at Point 5 along the LHC ring. The experiment has a cylindrical geometry and is divided in two main sections: the lateral section, called Barrel and the remaining ones called Endcaps (Figure 3.4). CMS was designed to fulfill among others the following important research tasks:

1. Search for the Higgs Boson
2. Search for physics beyond the standard model

Those tasks combined with the LHC design specifications require a detector with the following characteristics:

- High granularity and response;
- High radiation damage resistance;
- Good performances in the reconstruction of the μ particle charge, momentum and invariant mass;
- Good τ particle reconstruction efficiency;
- Good jet and b-jet reconstruction efficiency;
- High resolution on the combined reconstruction of electrons and photons;
- Great phase-space coverage of pseudo-rapidity $|\eta| < 5$;
- Good resolution in the missing transverse energy reconstruction.

The CMS detector has a length of 24 m and a diameter of 14.6 m for a total weight of 14500t. The experiment is made of several sub-detectors placed concentrically around the interaction point, each one providing complementary measurements (Figure 3.5). Particles coming from the interaction point first go through the tracking system which measures the position of charged particles traveling through its layers. The calorimeters are placed right outside the tracking system and are capable of measuring the particles energy deposits. The Electromagnetic Calorimeter (ECAL) measures the energy of electrons and photons, the Hadronic Calorimeter (HCAL) measures the energy of hadrons, particles made of quarks and gluons.

High resolution measurements of momenta of charged particles requires strong magnetic fields, therefore the CMS collaboration made the important choice to adopt superconducting technology for the experiment magnet. All previously introduced sub-detectors are contained inside the solenoid magnet. All particles except for muons and neutrinos are absorbed by the calorimeters. Outside the magnet there are the muon chambers witch identify muon particles and measure their momentum.

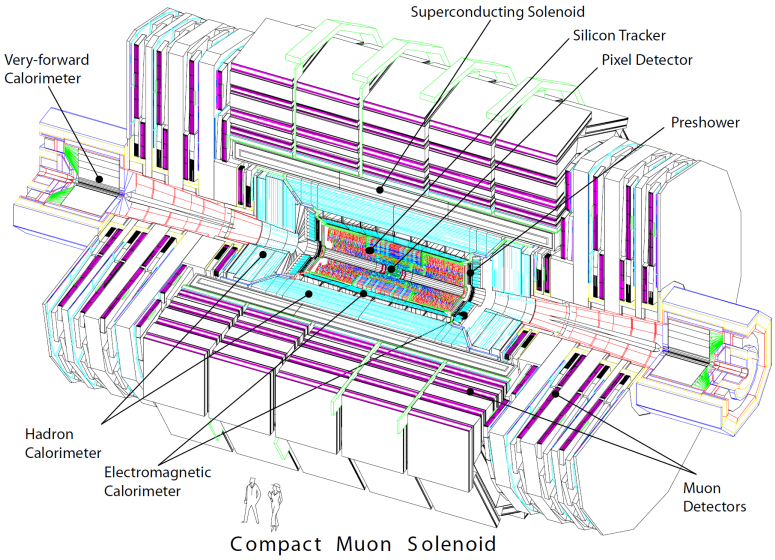

Figure 3.4: An exploited view of the CMS detector.

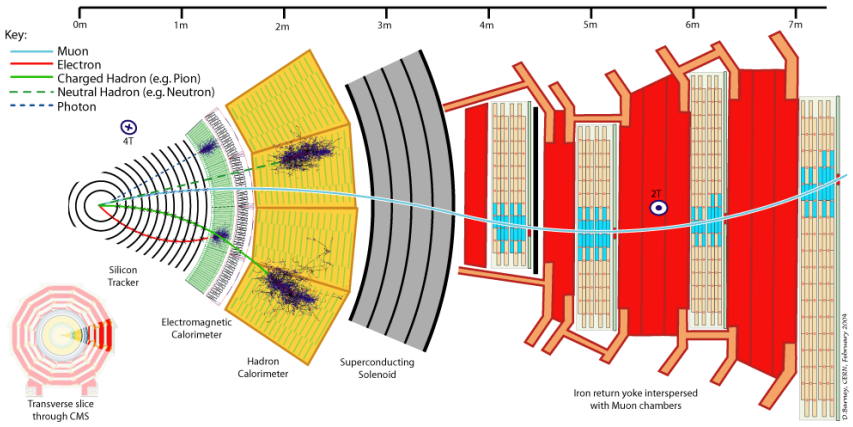

Figure 3.5: Longitudinal section of the CMS detector showing the different detectors components and position.

3.2.1 The magnet

The precision requirements of the muon chambers in order to distinguish unambiguously at 1 TeV/c the muon charge is $\Delta p/p \approx 10\%$ and therefore requires of a magnetic field with high bending power. The main features of the CMS solenoid are the use of a high-purity aluminium-stabilised conductor and indirect cooling (by a thermosyphon), together with full epoxy impregnation.

The CMS magnet is a large superconducting solenoid with an inner bore of 5.9 m and a length of 12.9 m. This good length-to-radius ratio is necessary to ensure good momentum resolution in the forward region as well. Its size is enough to contain the tracking system, the electromagnetic calorimeter and the hadronic calorimeter.

The high magnetic field of 3.8 T is generated by a current of 19.5 kA going through 2168 coil turns. An important parameter for this superconducting magnets design is the value of the hoop stress of 64 atm produced by the magnetic pressure due to the Lorentz force. The amount of total energy stored by the superconducting magnet is of 2.7 GJ.

3.2.2 Inner tracking system

The Inner Tracking systems reconstructs the track of charged particles and measures their momentum. In order to meet the design requirements of a compact design and high reconstruction efficiency (95% for high momentum μ particles) the main detector material is silicon. The detector can be divided in three parts:

- Close to the interaction point are the pixel detectors since the particle flux is very high. Each pixel is 100×150 μm^2 wide;
- In the intermediate region ($20 < r < 55$ cm) the particle flux is low enough to allow the usage of silicon micro-strips, each cell has the minimum size 10 cm $\times$ 80 μm;
- In the outermost region ($r > 55$ cm), the particle flux is low enough to allow bigger size micro-strips with size of 25 cm $\times$ 180 μm

A section of the whole inner tracking apparatus on the z-plane can be seen in Figure 3.6. Close to the interaction point three pixel-layers are placed at radial distances of 4.7, 7.3 and 10.2 cm. In the Barrel region the silicon micro-strips are placed at a radial distance between 20 and 110 cm. The forward region has instead two pixel and nine micro-strips layers. The barrel micro-strip section is divided in two different parts: the innermost and the outermost one. There are an additional three Inner Disks in the transition region between the Barrel and Endcap parts, on each side of the Inner Barrel. The total area of the pixel detector is ≈ 1 m^2, whilst that of the silicon strip detectors is 200 m^2, providing coverage up to $|\eta| < 2.4$. The inner tracker comprises 66 million pixels and 9.6 million silicon strips. The silicon pixels grants a precision of 10 μm on the (x, y) transverse plane and of 20 μm on the z axis. The resolution of the silicon micro-strips depends on each cell thickness, with a minimum value of 55 μm for the traverse plane. The overall layout apparatus is illustrated in Figure 3.7.

3.2.3 The Electromagnetic calorimeter

The Electromagnetic Calorimeter (ECAL) is an almost hermetic, homogeneous calorimeter comprising lead tungstate ($PbWO_4$) crystals mounted in the central barrel part, closed

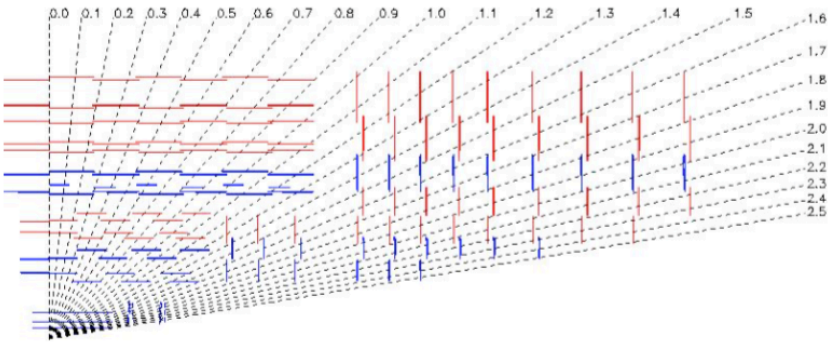

Figure 3.6: The tracker layout (1/4 of the z view).

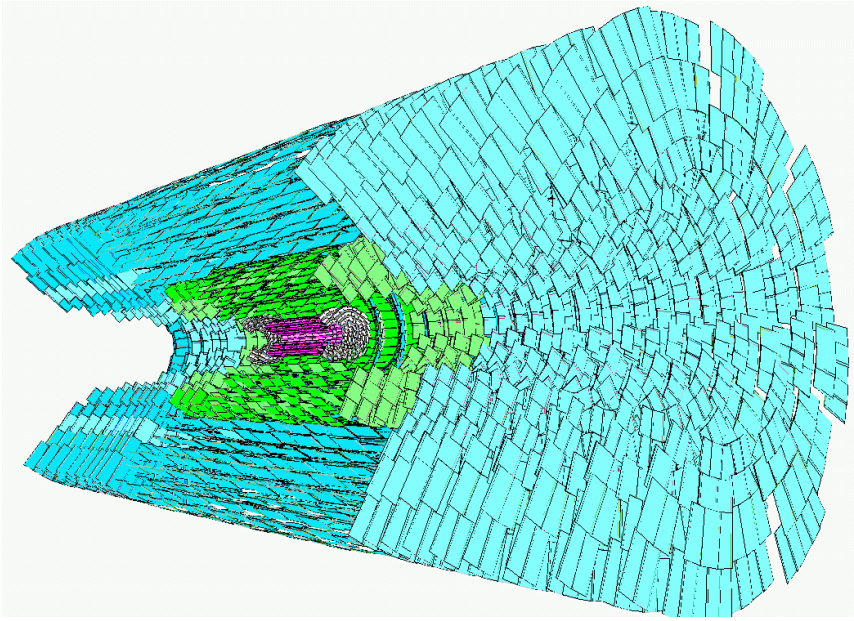

Figure 3.7: Visualization of the Si-Modules of the CMS Tracker [35].

by crystals in each of the two endcaps. The final design aim was to build a calorimeter as compact as possible. In order to have high hermeticity the space in between crystals has been reduced as much as possible especially in the transition region between barrel and endcaps. The crystal material choice was driven by the short radiation length and small Molière radius R_M, granting compactness and good granularity as listed on Table 3.1. Other important properties of $PbWO_4$ are radiation resistance and the short decaying time which allows to collect the 85% of light produced by the elecromagnetic showers during the 25 ns interval between a bunch crossing and the next one.

The barrel covers a pseudo-rapidity region of $|\eta| < 1.479$ with its cylinder radius of 129 cm. It contains 61200 crystals; 360 placed in ϕ and 2×85 in η. The crystals are quasi-projective (the axes are tilted at 3° with respect to the line from the nominal vertex position) and cover 0.0174 (i.e. $\approx 1°$) in $\Delta\phi$ and $\Delta\eta$. The crystals have a front face cross-section of $\approx 22 \times 22\text{mm}^2$ and a length of 230 mm, corresponding to $25.8X_0$. The

Density	8.28 g/ cm^3
X_0	0.89 cm
Molière Radius R_M 2.2	2.2 cm

Table 3.1: Parameters of the $PbWO_4$ crystals.

Endcaps cover the pseudo-rapidity of $1.48 < |\eta| < 2.6$ where the $2.6 \times 2.6 \times 22\text{cm}^3$ are gathered in 5×5 matrices called supercrystals.

In the pseudo-rapidity interval of $1.653 < |\eta| < 2.56$, as shown on Figure 3.8, a halo-ring shaped detector, called Preshower, is installed. It is a sampling calorimeter made by two distinct layers; the showering layer made of lead and the detector layer made of silicon strips capable of measuring the energy deposit of the initial part of particle showers as well as their lateral profile. The role of this detector is important whenever multiple particle showers overlap in the ECAL Endcap allowing a clear distinction of each of those showers.

The overall ECAL resolution can be parametrized as a function of the energy measured:

$$\frac{\sigma}{E}^2 = \frac{S}{\sqrt{E}}^2 + \frac{N}{E}^2 + C^2 \tag{3.1}$$

where S is the stochastic term, N the noise and C the constant term. The values of these parameters are listed on Figure 3.9.

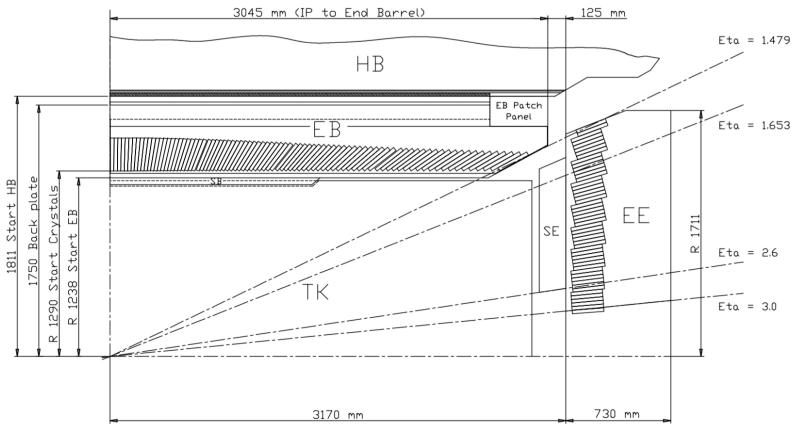

Figure 3.8: Longitudinal section of the electromagnetic calorimeter (one quadrant).

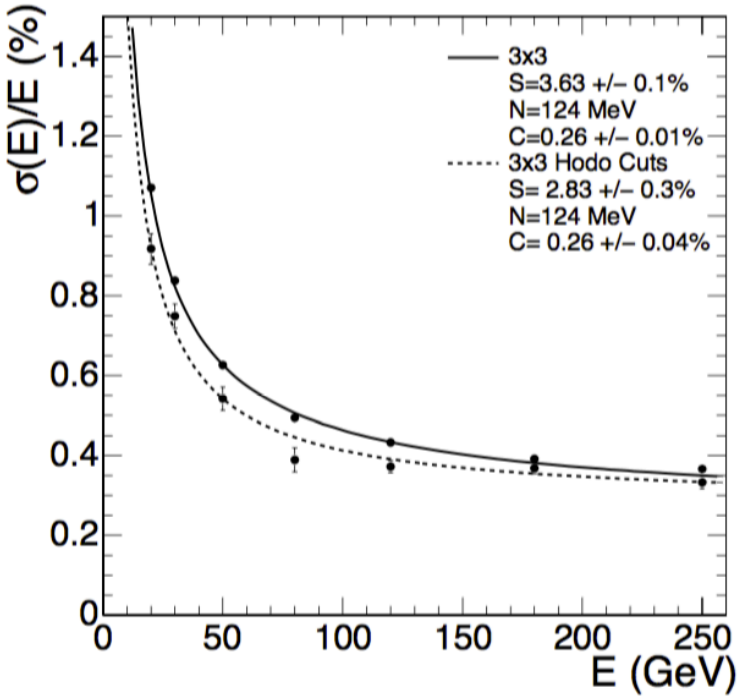

Figure 3.9: ECAL supermodule energy resolution, σ_E/E, as a function of electron energy as measured from a beam test. The upper series of points correspond to events taken with a 20×20 mm^2 trigger. The lower series of points correspond to events selected to fall within a 4×4 mm^2 region. The energy was measured in an array of 3 crystals with electrons impacting the central crystal.

3.2.4 The Hadron calorimeter

The Hadronic Calorimeter (HCAL) is used along side with the electromagnetic one in order to measure the energy deposit and position in the detector for hadronic jets and the missing transverse energy $\not{E}_{\mathrm{T}}$. The requirements for this detector are to minimize as much as possible the Gaussian tail of the resolution distribution and good containment of the hadronic showers in order to have good $\not{E}_{\mathrm{T}}$ reconstruction. Its design is influenced by the choice of the magnet parameters since is located inside the superconducting magnet along with the ECAL and the inner tracking system.

The barrel region of the HCAL (HB) consists of 32 towers covering the pseudo-rapidity region $-1.4 < \eta < 1.4$, resulting in 2304 towers with a segmentation $\Delta\eta \times \Delta\phi = 0.087 \times 0.087$, corresponding to a 5×5 ECAL crystal tower. The HB is constructed in two half barrels and has a single longitudinal sampling. There are 15 brass plates, each with a thickness of about 5 cm, plus two external stainless steel plates for mechanical strength. Particles leaving the ECAL volume first see a scintillator plate with a thickness of 9 mm rather than 3.7 mm for the other plates. The light collected by the first layer is optimized to be a factor about 1.5 higher than the other scintillator plates. The radiation length λ_0 for the HB is 8.9 cm.

The endcap regions of the HCAL (HE) consists of 14 η towers with 5° ϕ segmentation, covering the pseudo-rapidity region $1.3 < |\eta| < 3.0$. For the five innermost towers (at smaller η) the ϕ segmentation is 5° and the η segmentation is 0.087. For the eight outermost towers the ϕ segmentation is 10°, whilst the η segmentation varies from 0.09 to 0.35 at highest η. The total number of HE towers is 2304. The radiation length λ_0 for HE is 10.0 cm.

In order to improve the shower containment there's another calorimeter, called "Tail catcher" (HO) placed right outside the magnet. As further hermeticity improvement a "forward" calorimeter (HF) has been installed at around 11 meters from the interaction point, covering the η region of $3.0 < |\eta| < 5.0$. This calorimeter is made of steel/quartz fibres running parallel to the beam line.

Figure 3.10 shows the longitudinal section of the HCAL and the locations of its parts HB, HE, HF and HO.

The HCAL energy resolution is:

$$\frac{\sigma(E)}{E} \sim \frac{100\%}{\sqrt{E}} \oplus 4.5\% \tag{3.2}$$

Figure 3.11 shows of the jet energy resolution for different jet flavors as function of the simulate jet traverse energy [36].

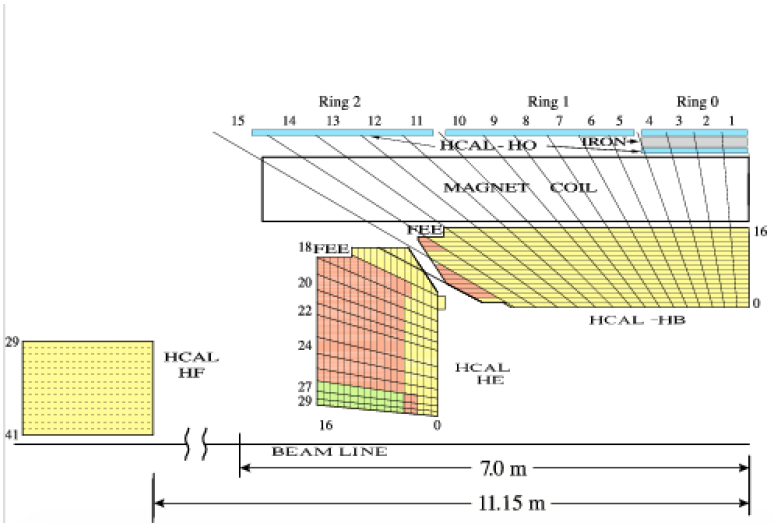

Figure 3.10: The CMS HCAL detector (quarter slice). "FEE" indicates the locations of the Front End Electronics for HB and HE. The signals of the tower segments with the same color are added optically, to provide the HCAL "longitudinal" segmentation. HB, HE and HF are built of 36 identical azimuthal wedges ($\Delta\phi = 20$ degrees).

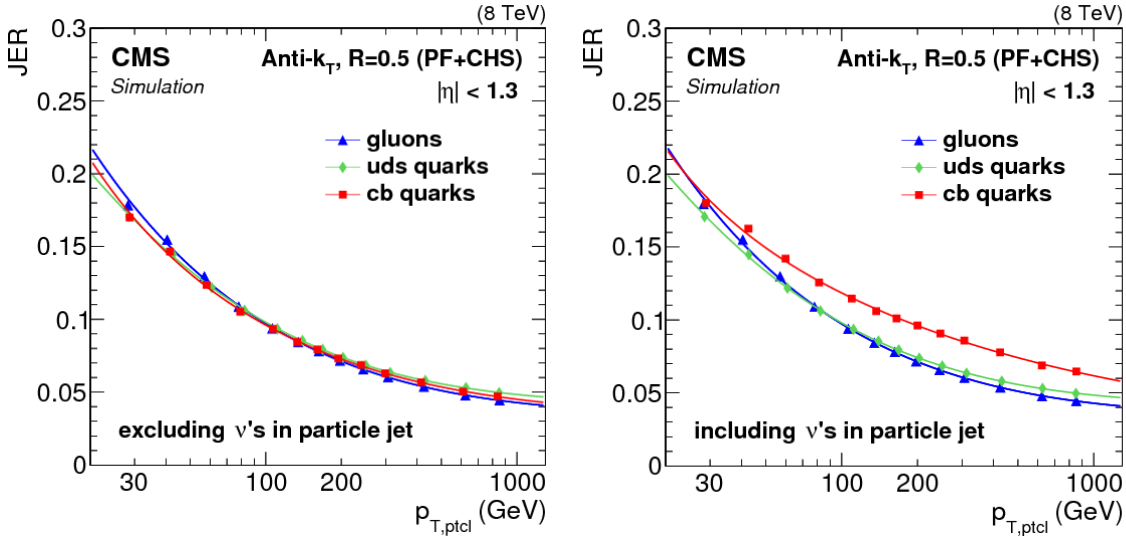

Figure 3.11: True jet energy resolution in simulation for different jet flavors in the γ + jet sample, for jets with $|\eta| < 0.5$. The distributions are shown for particle-level jets with no neutrinos (left), and with neutrinos exceptionally included (right) to demonstrate the large fluctuations this induces for c and b jets [36].

3.2.5 The Muon System

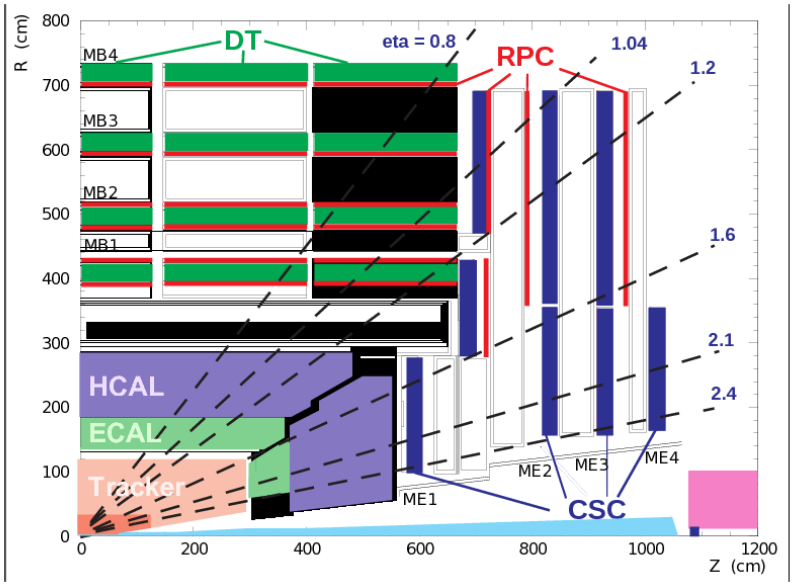

Figure 3.12: Layout of one quarter of the CMS muon system for initial low luminosity running. The RPC system is limited to $|\eta| < 1.6$ in the endcap, and for the CSC system only the inner ring of the ME4 chambers have been deployed.

Three types of gaseous detectors are used to identify and measure muons [37]. The choice of the detector technologies has been driven by the following reasons: the high radiation environment and the large surface area that has to be covered. Since in the barrel region ($|\eta| < 1.2$), both the muon rate and the residual magnetic field in the chambers is low, drift tube (DT) chambers are used. In the two endcaps instead, where the muon rate as well as the neutron induced background rate is high, and the magnetic field is also high, cathode strip chambers (CSC) are placed covering the pseudo-rapidity region up to $|\eta| < 2.4$. Additionally, resistive plate chambers (RPC) are used in both the barrel and the endcap regions covering a pseudo-rapidity region of $|\eta| < 2.1$. These RPCs operate in avalanche mode to ensure good performances at high rates and have double gap of 2 mm filled with gas. RPCs provide a fast response with good time resolution but with a coarser position resolution than the DTs or CSCs. RPCs can therefore identify unambiguously the correct bunch crossing [38].

The DTs or CSCs and the RPCs operate within the first level trigger system, providing independent and complementary sources of information. The layout of one quarter of the CMS muon system for the initial luminosity running is shown in Figure 3.12. In total, the muon system contains of order 25000 m^2 of active detection planes, and nearly 1 million electronic channels.

3.2.6 The Trigger System

With a bunch crossing rate of 40 MHz at design luminosity and the possibility to record the information for ∼100 Hz crossings per second, the CMS experiment needs a trigger system capable of a high rejection factor.

The CMS trigger and data acquisition system (DAQ) consist of four parts: the detector electronics, the hardware-based level 1 trigger, the readout network and the online event filter system that uses a software-based high level trigger (HLT) [39].

There's a minimum transit time required for the signal to reach the level 1 trigger hardware based on the service tunnels next to the CMS experiment site, wait for the trigger response to keep or discard the event and send it back to the detectors readout apparatus. The average time needed for a single cycle is 3.2 μs. During the following time the event information is stored in a buffer waiting for the Level-1 trigger response. The trigger decisional time is less than 1 μs with a rejection power of around 1 crossing kept for every 1000. An overview of the CMS L1 trigger system is shown on Figure 3.13.

The Level-1 decision is based on "trigger primitive" objects such as photons, electrons and muons and jets above thresholds as well as the transverse energy E_T and the missing transverse energy $\not{E}_{\mathrm{T}}$ involving the calorimetry and the muon system and a combination between these detectors. Since the Level-1 trigger is meant to take fast decisions at a high rate (the design value is 100kHz) the trigger objects are reconstructed with reduced resolution and granularity. A safe time margin of a factor of 3 is taken into account in order to cover for possible reconstruction uncertainties as well as beam and detector conditions leading to a rate of ∼100 Hz. The design value of 100 kHz is set by the average time to transfer full detector information through the readout system.

Once an event passes the Level-1 trigger selection the data from the pipelines to the front end readout buffers waiting for a further event reconstruction. After a successful reconstruction the compressed event is sent to one processors of the available farm that runs the High Level Trigger (HLT) software. The main aim of the HLT is to gather all the informations collected in the event in order to trigger over more complex objects such as τ particles, multiple jets and multiple particle object or event reconstructed quantities in order to further reduce the event rate from ∼100kHz to ∼100Hz for mass storage.

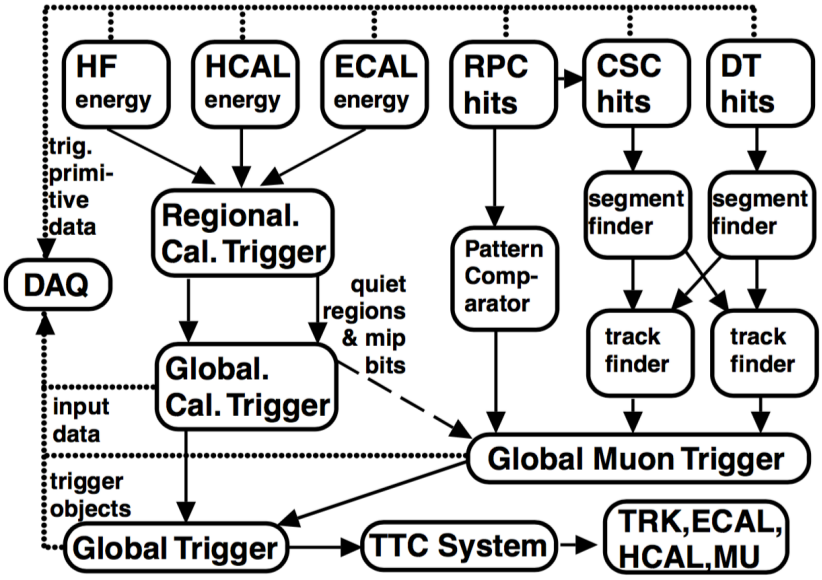

Figure 3.13: Overview of the CMS L1 trigger system [40]. Data from the forward (HF) and barrel (HCAL) hadronic calorimeters, and from the electromagnetic calorimeter (ECAL), are processed first regionally (RCT) and then globally (GCT). Energy deposits (hits) from the resistive-plate chambers (RPC), cathode strip chambers (CSC), and drift tubes (DT) are processed either via a pattern comparator or via a system of segment- and track-finders and sent onwards to a global muon trigger (GMT). The information from the GCT and GMT is combined in a global trigger (GT), which makes the final trigger decision. This decision is sent to the tracker (TRK), ECAL, HCAL or muon systems (MU) via the trigger, timing and control (TTC) system. The data acquisition system (DAQ) reads data from various subsystems for offline storage. MIP stands for minimum-ionizing particle.

3.2.7 Software and Computing

The CMS software and computing systems covers a broad range of tasks:

- online and offline calibration and status reports for each of the subdetectors;
- management, maintenance and access of the data storage;
- reconstruction and analysis of data;
- support of the distributed computing infrastructure and software framework.

The scale of the CMS collaboration in terms of storage capabilities and networking power is orders of magnitude higher that the CERN's infrastructure capabilities [41]. Therefore the CMS computing model is highly distributed, with a primary "Tier-0" centered at CERN with the additional support by "Tier-1" and "Tier-2" computing centers scattered worldwide in several universities and research centers.

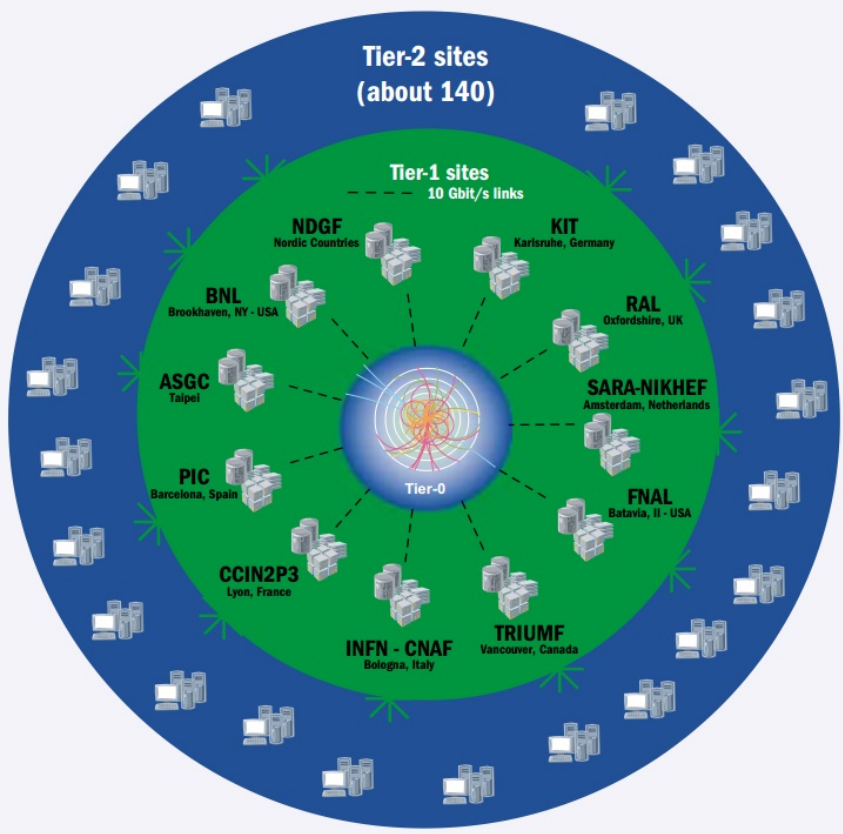

Figure 3.14: Overview of the structure of the CMS Computing Grid.

The scale of the CMS collaboration in terms of storage capabilities, networking power is orders of magnitude higher that the CERN's infrastructure capabilities. Therefore the CMS computing model is highly distributed consisting of four layers, or "tiers"; 0, 1, 2 and 3. Each tier provides a specific set of services.

All those facilities as shown on Figure 3.14 have hierarchical structure under the Tier-0 and go under the name of "CMS Computing Grid" [42].

3.2.7.1 Tier-0

This is the CERN Data Centre, which is located in Geneva, Switzerland and also at the Wigner Research Centre for Physics in Budapest, Hungary over 1200km away. The two sites are connected by two dedicated 100 Gbit/s data links. All data from the LHC passes through the central CERN hub, but CERN provides less than 20% of the total computing capacity.

Tier 0 is responsible for the safe-keeping of the raw data (first copy), first pass reconstruction, distribution of raw data and reconstruction output to the Tier 1s, and reprocessing of data during LHC down-times.

3.2.7.2 Tier 1

These are thirteen large computer centres with sufficient storage capacity and with round-the-clock support for the Grid. They are responsible for the safe-keeping of a proportional share of raw and reconstructed data, large-scale reprocessing and safe-keeping of corresponding output, distribution of data to Tier 2s and safe-keeping of a share of simulated data produced at these Tier 2s.

3.2.7.3 Tier 2

The Tier 2s are typically universities and other scientific institutes, which can store sufficient data and provide adequate computing power for specific analysis tasks. They handle analysis requirements and proportional share of simulated event production and reconstruction.

There are currently around 160 Tier 2 sites covering most of the globe.

3.2.7.4 Tier 3

Individual scientists will access these facilities through local (also sometimes referred to as Tier 3) computing resources, which can consist of local clusters in a University Department or even just an individual PC. There is no formal engagement between WLCG and Tier 3 resources.

4 Objects Reconstruction

The final aim of the CMS detector is the study of collision final states and several are the steps needed to transform the raw detector hits into useful information for an high energy physics analysis. The CMS collaboration converged its effort into a complex software algorithm, called Particle Flow, that combines all the information coming from all the experiments sub-detectors and reconstructs all the final state basic objects. Those reconstructed object ranges from simple particles such as electrons and muons to complex ones such as jets and hadronic taus. Particle Flow also reconstructs variables useful in the analysis selection such as jets imbalance and missing tranverse momentum. After a brief introduction on the Particle flow algorithm this chapter will give further information on the reconstruction on the most important objects used in the analysis described in this thesis.

4.1 The Particle Flow Algorithm

The raw data collected by the CMS experiment is the input of a detailed offline reconstructions of the collision final states. CMS developed over the years an algorithm, called the Particle Flow (PF) [43,44], that attempts to identify and to reconstruct the kinematic properties of each of the particles in the final states. For this purpose all the information coming from each of the CMS subdetectors is combined. This algorithm heavily relies on the precise measurement of the momenta of charged particles with the silicon tracker, and the precise measurement of photon and electron energies with the highly granular and hermetic ECAL, to overcome the coarser granularity of the HCAL. The reconstructed particles are then used to reconstruct jets, τ_{h} candidates, and the vector imbalance in transverse momentum in the event, referred to as $|\sum \vec{p}_{\mathrm{T}}^{\,\mathrm{PFcandidates}}|$, as well as to quantify the isolation of leptons.

4.1.1 Primary Vertices

The determination of collisions Primary Vertices (PV) for each of the bunch crossing is critical for reducing pile up effects and to detect long lived particles such as specific mesons. CMS reconstructs PVs starting from the vertices of all well reconstructed charged particle tracks in the event [45]. The first step consist on clustering the tracks according to the position on the z-axis of their closest track segment with respect to the beam line [46]. Then, a PV is reconstructed from each cluster with two or more constituents using a dedicated fit procedure. Which PV corresponds to the hardest interaction in the event is determined based on the tracks associated to the PV. The transverse momenta of all tracks associated to the PV are summed and the vertex with the highest sum is chosen. Every event used in this analysis requires at least a reconstructed PV. Table A.1 shows the detailed selection criteria for such requirement.

4.1.2 Electrons reconstruction

Electrons are reconstructed by matching tracks in the inner detector with energy depositions in the ECAL [43, 47]. The tracks of electron candidates are reconstructed using a Gaussian sum filter [48] algorithm, which accounts for the emission of bremsstrahlung photons along the electron trajectory. Energy loss in bremsstrahlung is reconstructed by searching for energy depositions in the ECAL located in directions tangential to the electron track. A multivariate approach based on boosted decision trees (BDT) [49] is employed for electron identification [50].

4.1.3 Muons reconstruction

The identification of muons is based on linking track segments reconstructed in the silicon tracking detector and in the muon system [51]. The matching between track segments is done outside-in, starting from a track in the muon system, and inside-out, starting from a track reconstructed in the inner detector. In case a link can be established, the track parameters are refitted using the combined hits in the inner and outer detectors, with the resulting track referred to as a global muon track. Quality criteria are applied on the multiplicity of hits, on the number of matched segments, and on the fit quality of the global muon track, quantified through a χ^2.

4.1.4 The Jet reconstruction

Jets within the range $|\eta| < 4.7$ are reconstructed using the anti-k_T algorithm [52] with a distance parameter of 0.5. As mentioned previously, the particles reconstructed by the PF algorithm are used as input to the jet reconstruction. Charged hadrons which are not coming from primary vertexes are discarded in the object reconstruction phase.

The energy of reconstructed jets is calibrated as a function of jet p_{T} and η [55].

Particle Flow jets (PFJets) are used in this analysis. The anti-k_{T} clustering algorithm with a reconstruction cone of $R = 0.5$ is used, defined in $\eta - \phi (R = \sqrt{\Delta\eta^2 + \Delta\phi^2})$ [58].

The PF jets used in this analysis are corrected using L1 FastJet, L2 Relative, and L3 Absolute corrections. The L1 FastJet corrections use the event-by-event UE/PU (Underlining Events / Pile Up) densities to remove the additional contributions to the measured jet energies due to underlying event and pile-up particles [56, 57]. The L2 and L3 corrections use jet balancing and γ + jets events to improve and provide a better energy response as a function of p_{T} and η. This analysis uses the "loose" working point Jet-Id selection criteria jets $p_{\mathrm{T}} = 30$ GeV and absolute pseudorapidity $|\eta| \leq 5.0$. Table A.4 shows the detailed selection criteria used for the recommended loose working point. The efficiency is > 98 for the entire η and p_{T} range. The "loose" working point has been validated in other studies.

Jets originating from the hadronization of b quarks are identified through the combined secondary vertex (CSV) algorithm [59], which exploits observables related to the long lifetime of b hadrons and the higher particle multiplicity and mass of b jets compared to light-quark and gluon jets. This analysis uses the loose working point of the combined secondary vertex algorithm [60]. The EPS13 prescription is used for the b-tagging and mis-tagging scale factors and efficiencies [61]. They are applied using the method called "Event reweighing using scale factors only" [62]. Table A.4 shows the detailed selection criteria.

4.1.5 $\not\!\!E_T$ reconstruction

Two algorithms are used to reconstruct $|\sum \vec{p}_T^{\,\mathrm{PFcandidates}}|$, the imbalance in transverse momentum in the event, whose magnitude is referred to as $\not\!\!E_T$. The standard algorithm computes the negative vectorial sum of all particle momenta reconstructed using the PF algorithm. In addition, a multivariate regression algorithm [63] has been developed to reduce the effect of pileup on the resolution in $\not\!\!E_T$. The algorithm utilizes the fact that pileup predominantly produces jets of low p_T, while leptons and high-p_T jets are produced almost exclusively in the hard-scatter.

Detection of weakly interacting particles is crucial both for SM measurements and searches for new physics. Although such particles leave no trace in any of CMSs sub-detectors, their transverse momenta can be estimated as the missing transverse energy in the event, making use of momentum conservation:

$$\not\!\!E_T = -\sum_j p_T^j \tag{4.1}$$

where p_T^j is the transverse momentum of PF particle j. Figure 4.1 shows the energy and ϕ resolution of the reconstructed $\not\!\!E_T$ in simulation versus the true $\not\!\!E_T$. Again, the PF approach is compared to the calorimetric-based approach and performs substantially better. Table A.6 shows the detailed selection criteria.

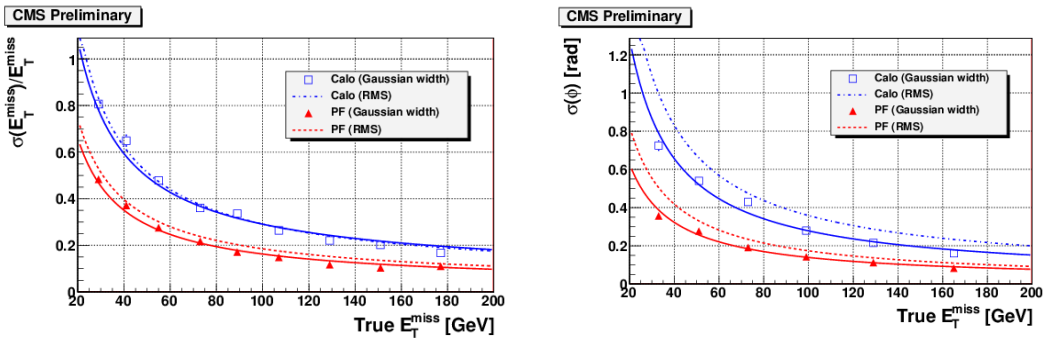

Figure 4.1: The energy and ϕ resolution of the $\not\!\!E_T$ in simulation. Red triangles show the resolution for the PF approach. Blue squares show the resolution for the calorimetric approach. The full lines show the results of fits of the data points and the dashed lines show the results of fits of an alternative resolution measure [43]

4.2 Tau lepton reconstruction

The τ lepton was discovered between 1974 and 1977 by the team under Martin Perl at SLAC/SPEAR while studying the $e^+ + e^- \longrightarrow e^\pm + \mu^\mp$ [64]. With a mean lifetime of 2.9×10^{-13} s and a mass of 1776.82 MeV [65] it is the heaviest of the leptons, enough to decay into hadrons, and it does so in about two thirds of the cases, typically into either one, three or five charged pions or kaons and up to four neutral pions π^0, and one neutrino ν_τ. The π^0 meson decays almost exclusively into $\gamma\gamma$. Among all the possible hadronic decays as shown on Table 4.2 the ones called "one-prong", where only one charged hadron is produced, are the most frequent. The τ decays also leptonically, with a branching ratio of 17% for each channel, via the following decay $\tau \longrightarrow \nu_\tau W^* \longrightarrow \nu_\tau l \nu_l$.

Decay Mode	Resonance	Mass [MeV]	BF (%)
$\tau^- \longrightarrow h^- \nu_\tau$	π	139.6	11.6
$\tau^- \longrightarrow h^- \pi^0 \nu_\tau$	ρ	770	26.0
$\tau^- \longrightarrow h^- h^+ h^- \nu_\tau$	a_1	1200	9.8
$\tau^- \longrightarrow h^- h^+ h^- \pi^0 \nu_\tau$			4.8
other hadronic channels			1.7
total			64.8

Figure 4.2: Hadronic tau decay modes into either one or three charged hadrons h and potential π_0, and the corresponding branching fractions BF. Also shown are the intermediate resonances and their masses, which are used in some of the tau reconstruction algorithms [65].

The τ_h decays are reconstructed and identified using the hadrons-plus-strips (HPS) algorithm [66], a cut-based algorithm focusing on the reconstruction of neutral pions. The HPS algorithm is seeded by jets of $p_\mathrm{T} > 14$ GeV and $|\eta| < 2.5$, reconstructed using the anti-k_T algorithm [52] with a distance parameter of 0.5. The algorithm is designed to reconstruct individual decay modes of the τ lepton, taking advantage of the excellent performance of the PF algorithm in reconstructing individual charged and neutral particles. The reconstruction and identification of τ_h decays in the HPS algorithm is performed in two steps:

- **Reconstruction:** combinations of charged and neutral particles reconstructed by the PF algorithm that are compatible with specific τ_h decays are constructed, and the four-momentum, expressed in terms of (p_T, η, ϕ , and mass) of τ_h candidates, is computed.
- **Identification:** discriminators that separate τ_h decays from quark and gluon jets, and from electrons and muons, are computed. This provides a reduction in the jet $\longrightarrow \tau_\mathrm{h}$, $e \longrightarrow \tau_\mathrm{h}$, and $\mu \longrightarrow \tau_\mathrm{h}$ misidentification rates.

4.2.1 Identification of decay modes

Reconstruction of specific τ_h decay modes requires reconstruction of neutral pions that are present in most of the hadronic τ decays. The high probability for photons originating

from $\pi^0 \longrightarrow \gamma\gamma$ decays to convert to e^+e^- pairs within the volume of the CMS tracking detector is taken into account by clustering the photon and electron constituents of the τ-seeding jet into strips in the $\eta - \phi$ plane. The clustering of electrons and photons of $p_T > 0.5$ GeV into strips proceeds via an iterative procedure. The electron or photon of highest p_T not yet included into any strip is used to seed a new strip. The initial position of the strip in the $\eta - \phi$ plane is set according to the η and ϕ of the seed e or γ. The e or γ of next-highest p_T that is within an $\eta \times \phi$ window centred on the strip location is merged into the strip. The strip position is then recomputed as an energy-weighted average of all electrons and photons contained in the strip [67].

τ_h candidates are formed by combining the strips with the charged-particle constituents of the jet. The charged particles are required to satisfy the condition $p_T > 0.5$ GeV. The distance of closest approach between their tracks and the hypothetical production vertex of the τ_h candidate, taken to be the vertex closest to the charged particle of highest p_T within the jet, is required to be less than 0.4 cm in the z direction and < 0.03 cm in the transverse plane. These requirements removes spurious reconstructed tracks and significantly reduces the effect of pileup.

A combinatorial approach is taken for constructing hadronic τ candidates. Multiple τ_h hypotheses, corresponding to combinations of either one or three charged particles and up to two strips, are constructed for each jet.

The four-momentum of each τ_h candidate hypothesis is given by the four- momentum sum of the charged particles and strips. In a few per cent of the cases, the charged particles included in the τ_h candidates are identified as electrons or muons, and are assigned their respective electron or muon masses by the PF algorithm. The HPS algorithm sets the mass of all charged particles included in τ_h candidates to that of the charged pion, except for electron constituents of strips, which are treated as massless. The charge of τ_h candidates is reconstructed by summing the charges of all particles included in the construction of the τ_h candidate, except for the electrons contained in strips. The probability for misreconstructing the τ_h charge is $\approx 1\%$, with a moderate dependence on p_T and η, for taus from Z decays.

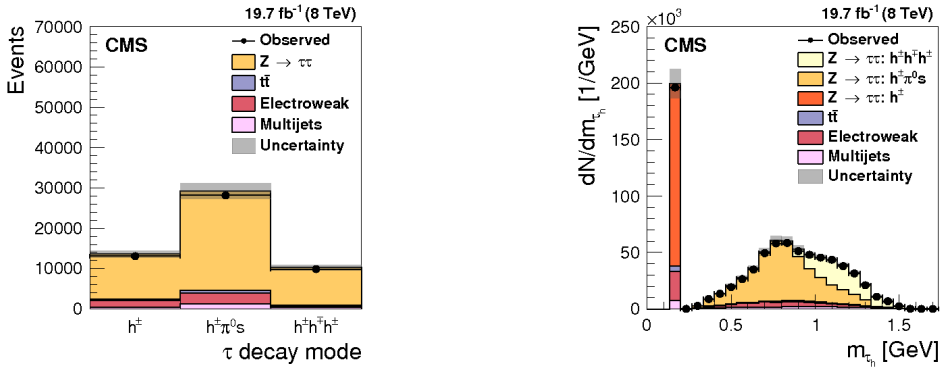

Figure 4.3: Contributions in reconstructed τ_h decay modes (left) and τ_h candidate masses in $Z/\gamma^* \longrightarrow \tau\tau$ events selected in data (right), compared to MC expectations. The $Z/\gamma^* \longrightarrow \tau\tau$ events are selected in the decay channel of muon and τ_h [67].

The following criteria are applied to assure the compatibility of each hypothesis with

the signatures expected for the different τ_h decays in Table 4.2:

1. $h^\pm h^\pm h^\pm$: Combination of three charged particles with mass $0.8 < m_{\tau_h} < 1.5$ GeV. The tracks are required to originate within $\Delta z < 0.4$ cm of the same event vertex, and to have a total charge of one.

2. $h^\pm \pi^0 \pi^0$: Combination of a single charged particle with two strips. The mass of the τ_h candidate is required to satisfy the condition $0.4 < m_{\tau_h} < 1.2\sqrt{p_T[\text{ GeV}]/100}$ GeV. The size of the mass window is enlarged for τ_h candidates of high p_T to account for resolution effects. The upper limit on the mass window is constrained to be at least 1.2 and at most 4.0 GeV.

3. $h^\pm \pi^0$: Combination of one charged particle and one strip with mass $0.3 < m_{\tau_h} < 1.3\sqrt{p_T[\text{ GeV}]/100}$ GeV. The upper limit on the mass window is constrained to be at least 1.3 and at most 4.2 GeV.

4. $h^\pm$: A single charged particle without any strips.

The combinations of charged particles and strips considered by the HPS algorithm represent all hadronic τ decay modes in Table 4.2, except $^- \longrightarrow h^- h^+ h^- \pi^0 \nu_\tau$. The latter corresponds to a branching fraction of 4.8% and is not considered in the present version of the algorithm, because of its contamination by jets. The $h^\pm\pi^0$ and $h^\pm\pi^0\pi^0$ decays are analyzed together, and referred to as $h^\pm\pi^0 s$.

Hypotheses that fail the mass window selection for the corresponding decay mode are discarded. When multiple combinations of charged hadrons and strips pass the mass window and the signal cone requirements, the hypothesis for the candidate with largest p_T is retained. All other combinations are discarded, resulting in a unique τ_h candidate to be associated to each jet.

The contributions in the decay modes and in the mass of τ_h candidates in $Z/\gamma^* \longrightarrow \tau\tau$ events are shown in Figure 4.3. The contribution of the $Z/\gamma^* \longrightarrow \tau\tau$ signal is split according to the reconstructed τ_h mode, as shown in the legend. For τ_h candidates reconstructed in the $h^\pm\pi^0 s$ and $h^\pm h^\pm h^\pm$ modes, the m_{τ_h} distribution peaks near the intermediate $\rho(770)$ and $a_1(1260)$ meson resonances (cf. Table 4.2), as expected. The narrow peak at the charged pion mass is due to τ_h candidates reconstructed in the $h^\pm$ mode.

4.2.2 Isolation

Requiring reconstructed τ_h candidates to pass strict isolation requirements constitutes the main handle for reducing the large multijet background [67]. Tau leptons are usually isolated relative to other particles in the event, and so are their decay products, in contrast to quark and gluon jets. Two types of τ_h isolation discriminants have been developed, using simple cutoff-based selections and an MVA approach. The expected efficiency of the τ_h isolation discriminants in $Z/\gamma^* \longrightarrow \tau\tau$ events ranges from 49.0% (Loose) to 38.1% (Tight) for the cutoff-based approach and 55.9% (Very Loose) to 27.3% (Tight) for the MVA one. The Jet $\rightarrow \tau$ misidentification rate of the τ_h isolation discriminants in Multi-jet events ranges from 3.86×10^{-3} (Loose) to 1.75×10^{-3}% (Tight) for the cutoff-based approach and 6.21×10^{-3} (Very Loose) to 4.43×10^{-3} (Tight) for the MVA one.

4.2.3 Electron and Muon veto

Electrons and muons have a sizable probability to get reconstructed in the $h^{\pm}$ decay mode. Electrons radiating a bremsstrahlung photon that subsequently converts may also get reconstructed in the $h^{\pm}\pi^0 s$ decay mode. In particular, electrons and muons originating from decays of W and Z bosons, which are produced with cross sections of ≈ 100 nb at the LHC at $\sqrt{s} = 8$ TeV have a high chance to pass isolation-based τ_{h} identification criteria. Dedicated discriminants have been developed to separate τ_{h} from electrons and muons [67]. The separation of τ_{h} from electrons is based on an MVA approach, with an efficiency and $e \to \tau$ misidentification rate going from 93.3% and 2.38×10^{-2} (Very loose) to 72.1% and 3.54×10^{-4} (Very tight) in $Z/\gamma^* \longrightarrow \tau\tau$ events. A cut based and an MVA based discriminant are used to separate τ_{h} from muons. The expected efficiency of the τ_{h} against muon discriminants in $Z/\gamma^* \longrightarrow \tau\tau$ events goes from 99.3% (Loose) to 99.1% (Tight) for the cutoff-based approach and 99.5% (Loose) to 98% (Tight) for the MVA one. The $\mu \to \tau$ misidentification rate efficiency of the τ_{h} isolation discriminants in $Z/\gamma^* \longrightarrow \mu\mu$ events ranges from 1.77×10^{-3} (Loose) to 7.74×10^{-4} (Tight) for the cutoff-based approach and 5.20×10^{-4} (Loose) to 3.18×10^{-4} (Tight) for the MVA one.

τ_{h} candidates are required to have a p_{T} of 45 GeV and a pseudo-rapidity of $|\eta| \leq 2.1$ in order to ensure that both tracks are reconstructed fully within the acceptance of the tracking system. In addition, a τ_{h} is required to have exactly one signal charged hadron with $p_{\mathrm{T}} = 5$ GeV and must not reside in the ECAL cracks.

One-prong τ_{h} candidates are selected using the `DecayModeFindingNewDMs` discriminator. In order to discriminate against muons, HPS taus are required to pass the `againstMuonLoose3` rejection discriminator which requires the leading track of the tau not be associated with a global muon signature. In order to discriminate against electrons, HPS taus are required to pass the `againstElectronMediumMVA5` discriminator which uses the amount of HCAL energy associated to the tau with respect to the measured momentum of the track. Additionally, the MVA discriminator considers the amount of electromagnetic energy in a narrow strip around the leading track with respect to the total electromagnetic energy of the tau.

The isolation discriminator is a BDT [49] discriminator based on isolation, p_{T} and τ_{h} lifetime information and defines the different TauID working points starting from the loose one with (`byLooseIsolationMVA3newDMwLT`) to the tighter one (`byTightIsolationMVA3newDMwLT`). Table A.4 shows the detailed selection criteria for an τ_{h} candidate.

5 Search for SUSY in Vector Boson Fusion Processes at the LHC

5.1 Introduction

Many of the searches for $\tilde{\chi}_1^{\pm}$ and $\tilde{\chi}_2^0$ in ATLAS [68, 69] and CMS [70] exploit events with three leptons and $\not{E}_{\mathrm{T}}$. Those searches dealt with some difficulties. Firstly, with the increasing luminosity at the LHC both experiments needed to raise the p_{T} thresholds on the triggered objects which degraded signal efficiency. Secondly Drell-Yan production cross-section of sleptons steeply declines with an increasing invariant mass [71].

As shown in early studies, however, an analysis of the $\tilde{\chi}_1^{\pm}/\ \tilde{\chi}_2^0$ system from a different angle in Vector Boson Fusion (VBF) events is also possible [72]. VBF production is characterized by the presence of two jets with a large di-jet invariant mass in the forward region in opposite hemispheres. Additionally the produced $\tilde{\chi}_1^{\pm}$ and $\tilde{\chi}_2^0$ decay into multiple τ leptons and two $\tilde{\chi}_1^0$ which travel through the detector undetected an can only be reconstructed as $\not{E}_{\mathrm{T}}$. A sample diagrams for $\tilde{\chi}_1^{\pm}/\ \tilde{\chi}_2^0$ pair production from VBF processes are shown in Figure 5.1.

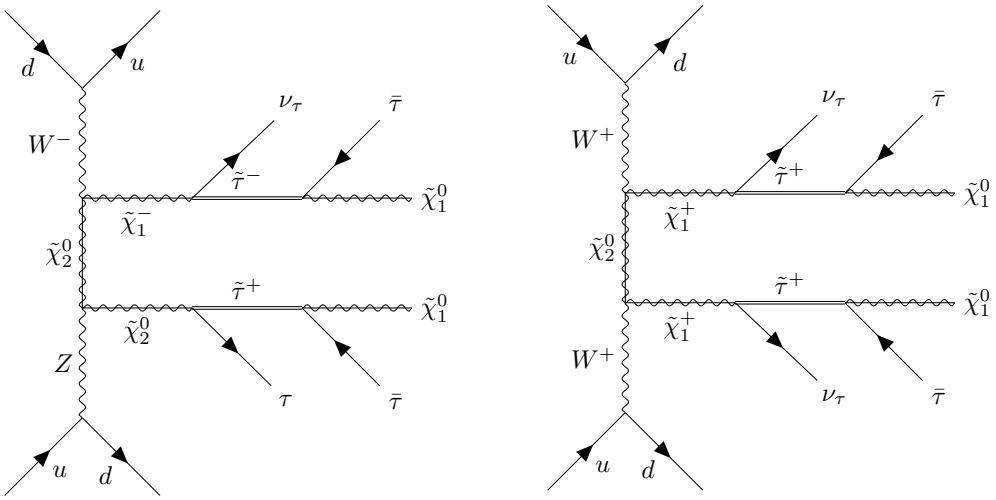

Figure 5.1: Diagrams of (left) $\tilde{\chi}_1^{\pm}\ \tilde{\chi}_2^0$ and (right) $\tilde{\chi}_1^{\pm}\ \tilde{\chi}_1^{\mp}$ pair production through vector-boson fusion including their decays to τ leptons and the LSP.

5.2 VBF with two leptons and two jets

This search for SUSY events with two leptons and two jets has some advantages with respect to the previous searches with no VBF signature [73]. Firstly, there is the possibility to probe signal for SUSY by triggering over the VBF properties of the event. This means that low kinematic constraints on the decay products of the $\tilde{\chi}_1^{\pm}$ $\tilde{\chi}_1^{\pm}$ pairs can be made.

Secondly VBF production allows the investigation of SUSY scenarios with high $\tan\beta$, in which case the $\tilde{\tau}_1$ is typically lighter than $\tilde{\mu}_1$ and $\tilde{e}_1$ [74]. A light $\tilde{\tau}_1$ with small mass splitting is favored in coannihilation processes [75] that set the relic density to correct values, in the case of Bino-like dark matter. A light $\tilde{\tau}_1$ is also motivated in the context of the MSSM by a possible enhancement of the $H \longrightarrow \gamma\gamma$ channel [76]. These facts stress the importance of searches in τ final states with low p_{T} and large backgrounds, for which production by VBF processes is more suited since the VBF signature allows for the reduction of the backgrounds to manageable levels.

Finally, the cross-section via Drell-Yan production declines faster than the VBF production cross-section with increasing mass allowing further control over background distributions [77].

The main feature of a VBF processes is the production of a jet pair aimed at the forward-backward region of the detector with high p_{T} and large $\Delta\eta$. By adding to the event selection the requirements on the di-jet $\Delta\eta$ as well as the invariant mass $m_{j_1 j_2}$ of the two jet candidates originated from the VBF processes the background contribution coming from V+jets and $\mathrm{t\bar{t}}$ events, shown in Figures 5.11 and 5.9, is kept under control. In order to generate supersymmetric particles, the incoming partons need to have an high momentum, so that the leading jet from the VBF-produced di-jet pair is expected to have higher p_{T} than WW production via VBF. The addition of a p_{T} cut on leading jets further reduces background contributions. Figure 5.3 shows a study on $m_{j_1 j_2}$ and leading jet p_{T} distributions for $\tilde{\chi}_1^{\pm}$ $\tilde{\chi}_1^{\pm}$ pair production by VBF processes, V+jets background, and VV background produced by VBF processes for $m_{\tilde{\chi}_1^{\pm}} = m_{\tilde{\chi}_2^0} = 300, 200$ and 100 GeV, $m_{\tilde{\chi}_1^{\pm}} - m_{\tilde{\tau}} = 5$ GeV and $m_{\tilde{\chi}_1^0} = 0$ GeV. This study shows the possibility of an increase in the signal-to-background ratio by imposing cuts such as m_{jj}, $p_{\mathrm{T}}(\tau)$, $p_{\mathrm{T}}(jet)$ and $\not{E}_{\mathrm{T}}$.

The remaining background contributions come from all the centrally produced particles. By considering an R-parity conserving model the decay of $\tilde{\chi}_1^{\pm}$ and $\tilde{\chi}_2^0$ are:

$$\tilde{\chi}_1^{\pm} \longrightarrow \tilde{\tau}_1^{\pm}\nu \longrightarrow \tau^{\pm}\tilde{\chi}_1^0\nu; \tag{5.1}$$

$$\tilde{\chi}_2^0 \longrightarrow \tilde{\tau}_1^{\pm}\tau^{\mp} \longrightarrow \tau^{\pm}\tau^{\mp}\tilde{\chi}_1^0. \tag{5.2}$$

Processes with same signature are all the VV (where V may be both W or Z) pairs produced via VBF where the bosons decays leptonically. Furthermore, in case of only τ_{h} decays Quantum Chromo Dynamics (QCD) multijet becomes an important background contribution. A cut on $\not{E}_{\mathrm{T}}$ is effective in reducing those backgrounds as shown on Figure 5.4. Requiring multiple τ leptons in the event further reduces Standard Model background contributions. The p_{T} of the τ coming from the $\tilde{\chi}_1^{\pm}$ and $\tilde{\chi}_2^0$ decays is strongly correlated to the mass difference between the $\tilde{\chi}_1^{\pm}$ and the $\tilde{\chi}_1^0$ LSP. In Figure 5.4, the normalized distribution of the p_{T} of the τs is displayed for $m_{\tilde{\chi}_1^{\pm}} = m_{\tilde{\chi}_2^0} = 300$ GeV, $m_{\tilde{\chi}_1^{\pm}} - m_{\tilde{\tau}} = 5$ GeV and $m_{\tilde{\chi}_1^0} = 0$ GeV. For smaller ΔM, the distribution peaks at lower p_{T} and the signal

acceptance is less efficient.

5.3 Search Strategy

For this type of search several benchmark points are defined with the following constraints. Firstly the $\tilde{\chi}_1^{\pm}$ and $\tilde{\chi}_2^0$ are mainly Wino-like, while the $\tilde{\chi}_1^0$ is mainly Bino-like. Furthermore, the $\tilde{\chi}_1^{\pm}$ mass is similar to the $\tilde{\chi}_2^0$ mass ($m_{\tilde{\chi}_1^{\pm}} \sim m_{\tilde{\chi}_2^0}$) and at values of 100, 200 and 300 GeV. Additionally the mass gap between the $\tilde{\tau}_1$ and $\tilde{\chi}_1^{\pm}$ is either 5 GeV or $(m_{\tilde{\tau}_1} - m_{\tilde{\chi}_1^{\pm}})/2$. Finally the LSP mass is either $\tilde{\chi}_1^0 = 0$, or 50 GeV.

The following processes are taken into account:

$$pp \longrightarrow \tilde{\chi}_1^{\pm}\tilde{\chi}_1^{\mp}jj, \quad pp \longrightarrow \tilde{\chi}_1^{\pm}\tilde{\chi}_2^0 jj, \quad pp \longrightarrow \tilde{\chi}_2^0\tilde{\chi}_2^0 jj \tag{5.3}$$

The cross-section prediction for each of those processes are shown in Figure 5.2 as function of the $\tilde{\chi}_1^{\mp}$- $\tilde{\chi}_2^0$ mass.

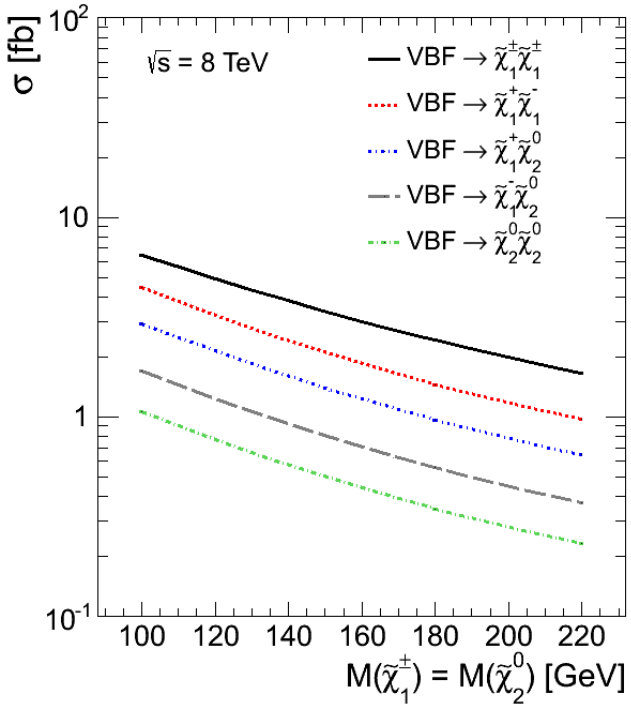

Figure 5.2: VBF production cross-section at $\sqrt{s}$= 8 TeV as a function of mass for various channels after imposing $\Delta\eta > 4.2$ using Madgraph 4 (NLO) [73].

The search strategy can be divided in two distinct parts: the first one considers the kinematic of the jets produced via VBF in order to reduce the contribution coming from V + jets events (where V is either the W or Z boson); the second one focuses on the decay products of the supersymmetric particles falling into the inner region of the detector (centrally produced) in order to reduce the overall background contributions.

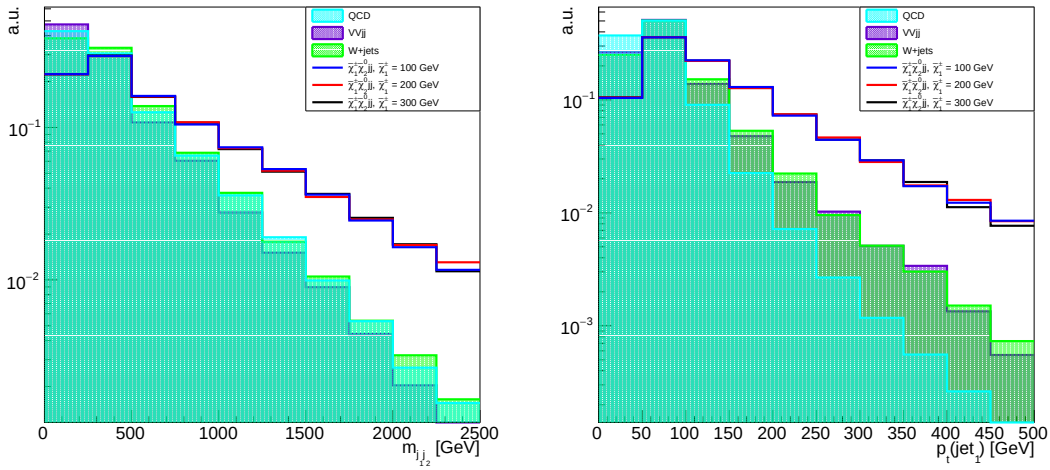

Figure 5.3: $m_{j_1 j_2}$ (left) and p_{T} of the leading jet (right) distributions normalized to arbitrary units for $\tilde{\chi}_1^{\pm}$ $\tilde{\chi}_1^{\pm}$ pair production by VBF processes, V+jets background, and VV background produced by VBF processes and QCD processes. The chosen signal benchmark point features $m_{\tilde{\chi}_1^{\pm}} = m_{\tilde{\chi}_2^0} = 300, 200$ and 100 GeV, $m_{\tilde{\chi}_1^{\pm}} - m_{\tilde{\tau}} = 5$ GeV and $m_{\tilde{\chi}_1^0} = 0$ GeV.

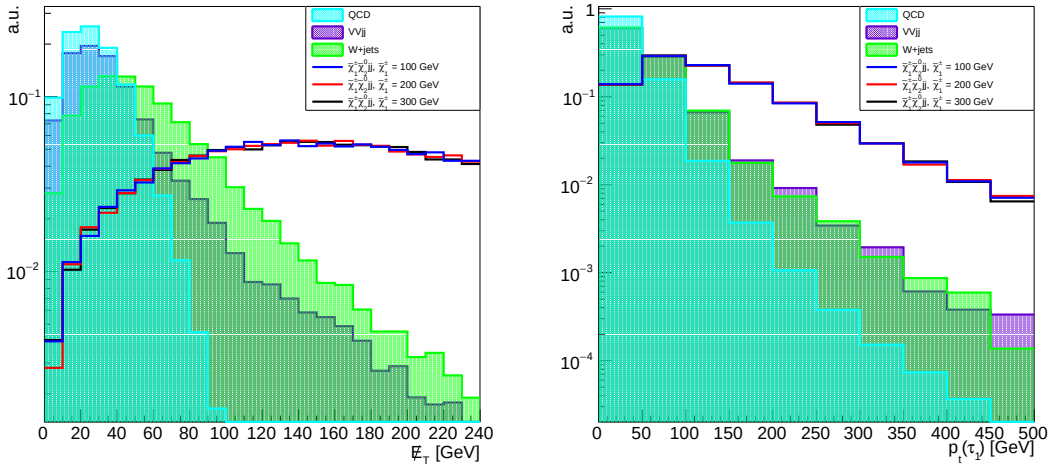

Figure 5.4: (left) $\not{E}_{\mathrm{T}}$ and (right) leading τ p_{T} distributions normalized to arbitrary units in $\geq 2j + 2\tau$ final state for $\tilde{\chi}_1^{\pm}$ $\tilde{\chi}_1^{\pm}$ pair production by VBF processes, V+jets background, and VV background produced by VBF processes and QCD processes. The chosen signal benchmark point features $m_{\tilde{\chi}_1^{\pm}} = m_{\tilde{\chi}_2^0} = 300, 200$ and 100 GeV, $m_{\tilde{\chi}_1^{\pm}} - m_{\tilde{\tau}} = 5$ GeV and $m_{\tilde{\chi}_1^0} = 0$ GeV.

5.4 VBF with two same sign hadronic τ and two jets

Besides the two oppositely directed forward jets that define the VBF configuration, the search requires the presence of at least two leptons coming from the different decay modes of the τ and large $\not{E}_{\mathrm{T}}$. The chosen search channels are $e\mu jj$, $\mu\mu jj$, $\mu\tau_{\mathrm{h}}jj$, and $\tau_{\mathrm{h}}\tau_{\mathrm{h}}jj$. The final states are further differentiated into like-sign (LS) and opposite-sign (OS) di-lepton pairs for a total of eight different search channels [78]. This thesis focuses its attention on the di-τ_{h} LS channel search and its background estimation strategy.

5.4.1 Background Contributions

The most important aspect of any search for new physics is the methodology used to estimate the background contribution in the signal region. The first step consists in the determination of all irreducible background processes and the definition of a technique to estimate each of the contributions. Five types of background contributions have been considered in this analysis.

The first irreducible background contribution is coming from the Standard Model VBF processes resulting in two τ_{h} and two jets as shown in Figure 5.5. This background is purely electroweak, well modeled and its cross section is very small. Therefore this background is considered minor and its contribution is directly estimated using Monte Carlo simulation.

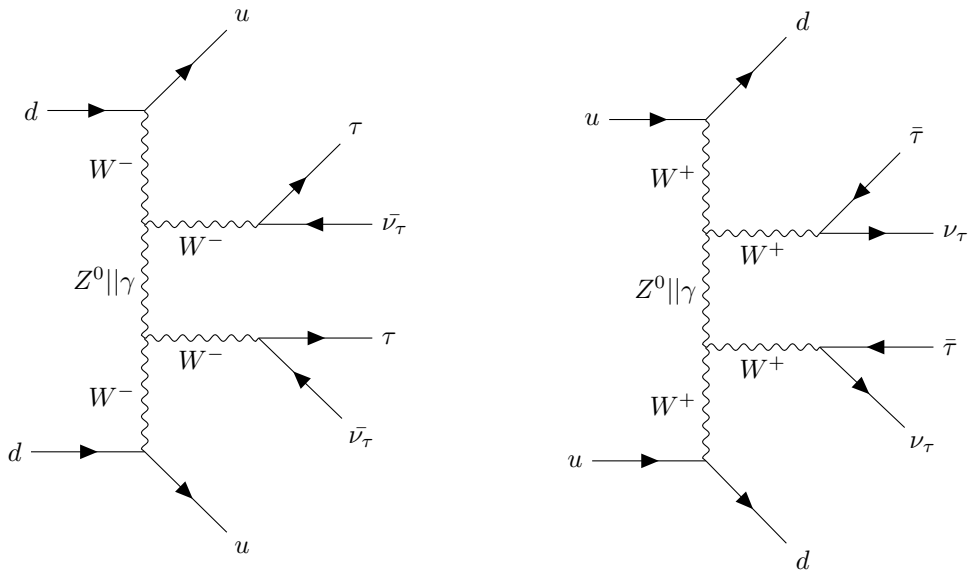

Figure 5.5: Feynman diagrams of irreducible backgrounds from Standard Model Vector Boson Fusion processes. Two hadronically-decaying τ leptons and two jets are observed.

Secondly, all the Standard Model VBF processes resulting in three leptons (Figure 5.6), with the opposite charged lepton failing to pass the tauID.

Those processes are again purely electroweak, therefore the rate and relative theoretical uncertainty on the rate are small compared to QCD. Additionally, the probability for events coming from this background contribution to pass the event selection is very low.

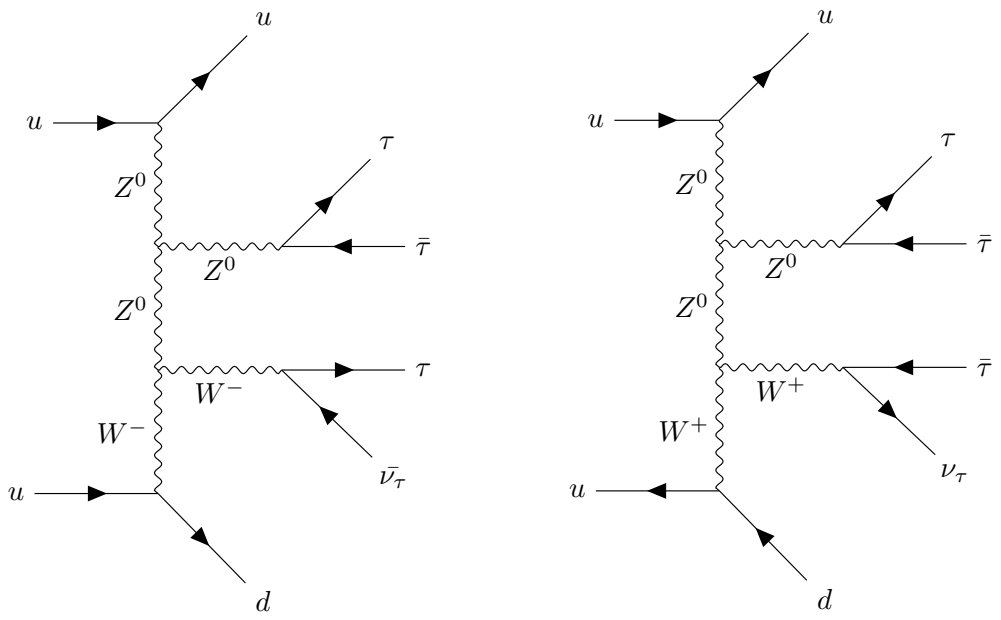

Figure 5.6: Feynman diagrams of irreducible backgrounds from Standard Model Vector Boson processes. Three τ are produced and the opposite charged lepton fails to pass the tauID selection criteria.

In conclusion, this topology of events is considered to be a minor contribution to the total background.

Thirdly, there are the Standard Model backgrounds where one of the τ_{h} has a mis-reconstructed charge as shown in Figures 5.7, 5.8 and 5.9. All of these processes have a very low cross section compared to the one coming from the main background contribution, therefore those processes are all considered a minor background and their event contribution is taken directly from simulation.

The fourth background contribution comes from all the QCD events resulting in four jets with two of those jets reconstructed as a fake τ_{h}. Even though the probability of a jet to fake a τ_{h} is low, the production cross sections of QCD events in a hadron collider are large. Therefore, even small $\tau_{\mathrm{h}}^{\mathrm{fake}}$ rates from QCD processes, matter. Also, in QCD events, additional jet activity from initial or final jet radiation processes is expected, which gives these type of events a high probability to pass the VBF selection criteria. Those motivations lead to the determination of QCD as main background source for this analysis. Examples of some QCD processes are shown in Figure 5.10.

The last background contribution comes from the $\tilde{\chi}_1^{\pm}$-$\tilde{\chi}_2^0$ pair events produced via QCD production. In case for low squark masses, in the order of 1 - 2 TeV, this topology of processes has an important contribution in the composition of irreducible background for this analysis. An example of a $\tilde{\chi}_2^0$ pair production is shown on Figure 5.12.

Furthermore, there are QCD processes resulting in one τ_{h} and three jets with one of the jets mis-reconstructed as the second τ_{h}. Examples of those processes are shown on Figure 5.11

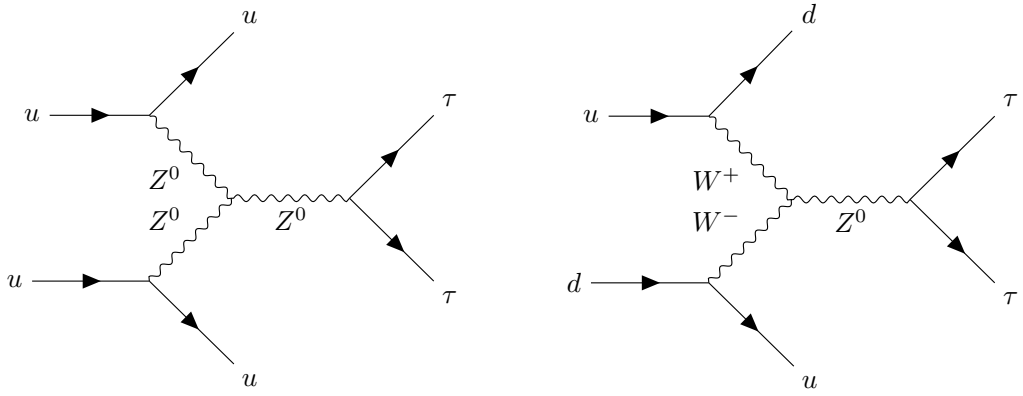

Figure 5.7: Feynman diagrams of irreducible backgrounds from Standard Model Vector Boson Fusion Z^0 production.

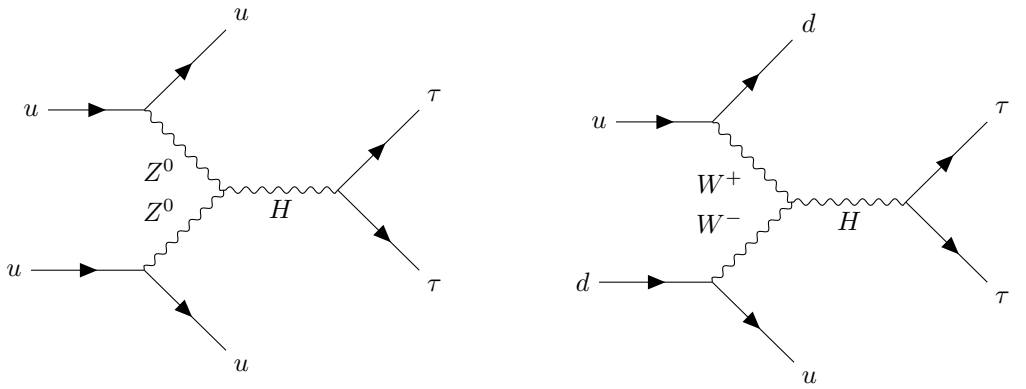

Figure 5.8: Feynman diagrams of irreducible backgrounds from Standard Model Vector Boson Fusion Higgs production.

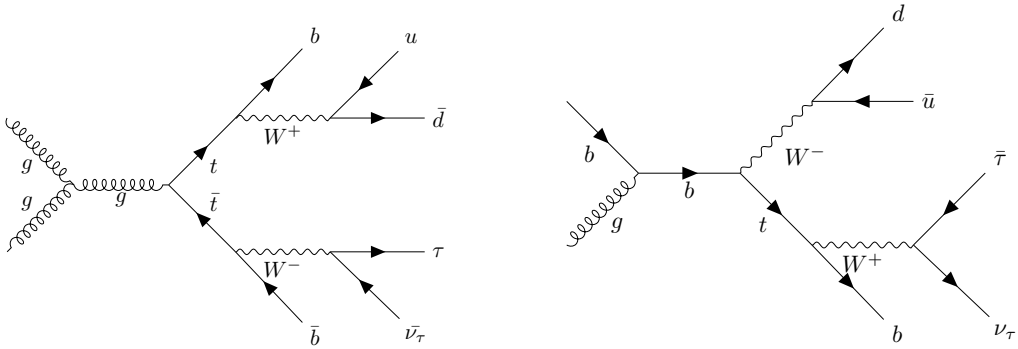

Figure 5.9: Feynman diagrams of $t\bar{t}$ (left) and single top (right) production which can be a background process if one of the jets is reconstructed as a τ_h.

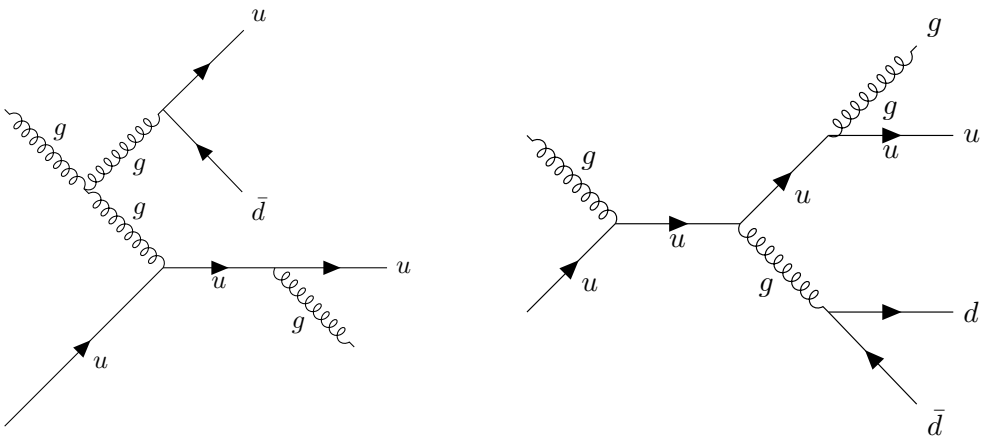

Figure 5.10: Feynman diagram of a four jet QCD prodution with initial state radiation (left) and final state radiation (right) where two jets are misreconstructed as τ_{h}.

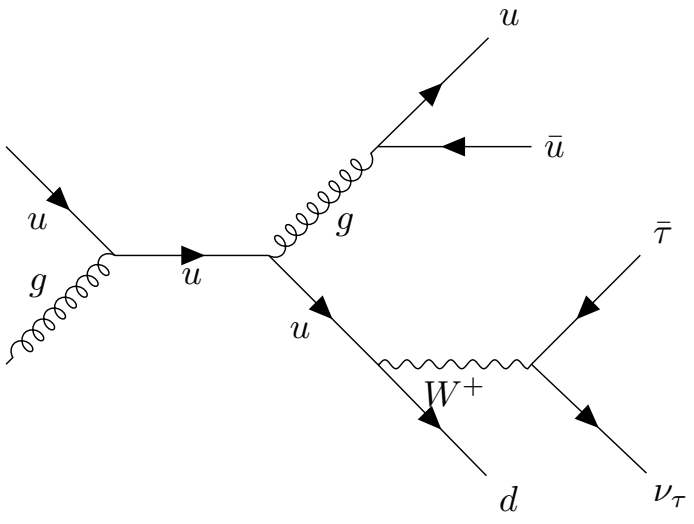

Figure 5.11: Feynman diagrams of W boson plus 3 jets production where one jet is misreconstructed as τ_{h}.

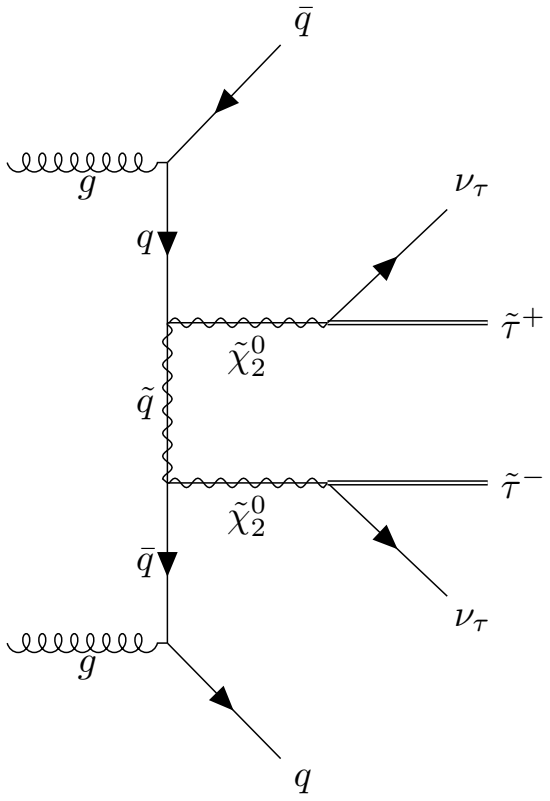

Figure 5.12: Feynman diagram of QCD production of $\tilde{\chi}_2^0$ pair.

6 Analysis of 8 TeV data

The following chapter describes the analysis with two same sign τ_h and two jets performed with 8 TeV data. After a brief description of the data and Monte Carlo samples, details follow on the selection used following the strategy suggested in Chapter 5. The next section motivates and describes the data-driven background estimation technique used for treating QCD background events where two jets get mis-reconstructed as τ_h and pass the event selection. Details on the validation method and systematic uncertainties are given in the last two sections.

6.1 Data sample and trigger paths

The analysis is performed using data collected with the CMS detector in proton-proton collisions at a centre of mass energy of $\sqrt{s}$= 8 TeV at the LHC. The data samples correspond to an integrated luminosity of 19.7 fb^{-1}. The original analysis design considered the usage of a VBF-based trigger. By doing the online selection over the properties of the hard jets coming from VBF processes, this trigger would a given a great freedom on the offline selection of the τ_h properties and on $\not\!\!E_T$. However the available HLT trigger was seeded by $\not\!\!E_T$ L1 trigger that was fully efficient at roughly $\not\!\!E_T > 250$ GeV. Implementing such value in the offline event selection would have had a drastic impact on signal events statistics as previously shown on Figure 5.4.

The other available trigger strategy was relying on the choice of a double-lepton trigger for each of the different search channel. In case of the τ_h τ_h channel the only unprescaled available alternative is the `HLT_DoubleMediumIsoPFTau35_Trk*_eta2p1_Prong1_v*` trigger. This trigger is the least competitive among all the lepton trigger but is the one with the highest signal acceptance for the τ_h channel. An efficiency study on the selected trigger is shown on Figure 6.1.

6.2 Signal and background samples

All the background yields, except for the dominant QCD, are taken from simulation. Simulated samples of signal and background events are generated using Monte Carlo event generators.

The signal event samples are generated with the `MadGraph v5.1.5` program [80], considering pair production of gauginos with two associated partons. The signal events are generated requiring a pseudorapidity gap $|\Delta\eta| > 4.2$ between the two partons, with $p_T > 25$ GeV for each parton. Signal cross sections are calculated at leading order using the MadGraph generator. The range of signal cross sections is 50^{-1} fb for $\tilde{\chi}_1^\pm = \tilde{\chi}_2^0$ masses is 100 to 400 GeV. Two different assumption has been taken into account to fix the $\tilde{\tau}_1$ mass: the fixed-mass assumption, where the mass is fixed to a value close to the $\tilde{\chi}_1^\pm$ mass ($m_{\tilde{\chi}_1^\pm} - m_{\tilde{\tau}_1} = 5$ GeV) and the average-mass assumption, where is fixed in between the $\tilde{\chi}_1^\pm$

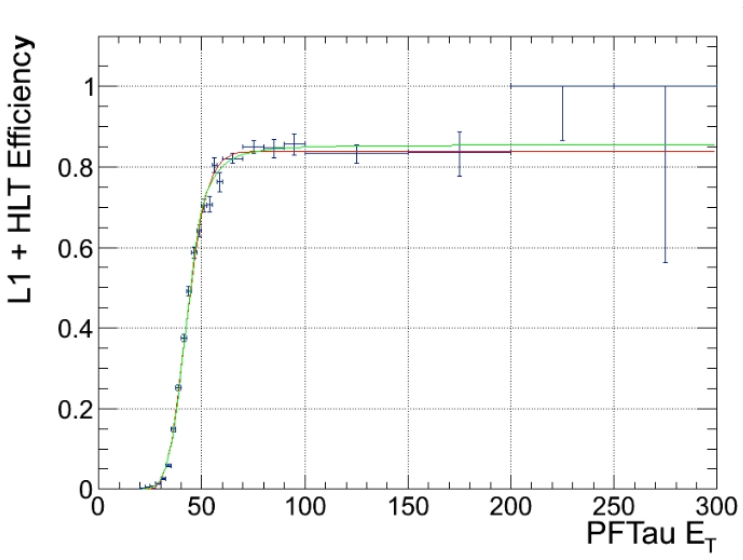

Figure 6.1: Efficiency study on the `HLT_DoubleMediumIsoPFTau35_Trk*_eta2p1_Prong1_-v*` trigger versus the τ_h transverse energy.The comparison of the fit curves given by the convolution of the step function with the Crystal Ball (in green) and the Gaussian (in red) is reported [79].

and $\tilde{\chi}_1^0$ masses ($m_{\tilde{\tau}_1} = 0.5m_{\tilde{\chi}_1^0} + 0.5m_{\tilde{\chi}_1^\pm}$). For each of those assumption two different scenarios has been taken into account: the uncompressed mass spectrum scenario, where the $\tilde{\chi}_1^0$ is considered massless ($m_{\tilde{\chi}_1^0} = 0$ GeV), and the compressed mass spectrum scenario, where the $\tilde{\chi}_1^0$ mass is fixed to a value close to the $\tilde{\chi}_1^\pm$ ($m_{\tilde{\chi}_1^\pm} - m_{\tilde{\chi}_1^0} = 50$ GeV). In order to minimize the contribution of all the QCD produced chargino/neutralino pair production as previosly shown on Figure 5.12 the masses of the squarks are set to high values.

Background event samples with a Higgs boson produced through VBF processes, and single top are generated with the `POWHEG v1.0r1380` program [81]. The `MadGraph v5.1.3` generator is used to describe Z+jets, W+jets, $t\bar{t}$, di-boson, and VBF Z boson production. The Monte Carlo background and signal yields are normalized to the integrated luminosity of the data. The $t\bar{t}$ background is normalized to the next-to-next-to-leading-logarithm level using the calculations presented in references [82, 83]. The Z+jets and W+jets processes are normalized to next-to-next-to-leading-order using the results from the `FEWZ v2.1` [84] generator. The di-boson background processes are normalized to next-to-leading-order using the `MCFM v5.8` [85] generator, while the VBF Z boson events are normalized to next-to-leading order using the `VBFNLO v2.6` [86, 87]program. The single-top and VBF Higgs boson background yields are taken from the `POWHEG` program, where the next-to-leading order effects are incorporated.

All Monte Carlo samples incorporate the `CTEQ6L1` [88] or `CTEQ6M` [89] parton distribution functions (PDF). The corresponding evaluation of uncertainties in the signal cross sections is discussed in Section 6.6. The `POWHEG` and `MadGraph` generators are interfaced with the `PYTHIA v6.4.22` [90] program, which is used in the matching between the matrix elements and the parton shower, and the hadronization processes.

The decays of τ leptons are simulated using the `tauola (27.1215)` [91] program. The background samples are processed with a detailed simulation of the CMS apparatus using the `Geant4` package [92], while the response for signal samples is modeled with the CMS fast simulation program [93]. For the signal acceptance and m_{jj} shapes based on the fast simulation, the differences with respect to the `Geant4`-based results are found to be small ($< 5\%$).

For all Monte Carlo samples, multiple proton-proton interactions are superimposed on the primary collision process, and events are reweighted such that the distribution of reconstructed collision vertices matches that in data. The distribution of the number of pileup interactions per event has a mean of 21 and a root-mean-square of 5.5.

For all datasets, a common `Physics Analysis Toolkit` (`PAT`) [94] sequence has been used to generate samples in PAT format, then further reduced them in size with the ntuple producer [95].

6.3 Event Selection

As mentioned in Section 5.3 the di-τ_h channel's main background contribution comes from QCD multijetevents, with a rate several orders of magnitude larger than the rate of other background contributions. Hence this search channel, more than any of the other lepton channels, relies on the efficient background rejection. Fortunately, the VBF and $\not\!\!E_T$ selections provide the required background suppression.

All the collision data events passing the requirements of the triggers shown in Table A.2 are considered for offline analysis.

As previously introduced in Section 5.3, the event selection criteria is divided in two distinct parts: the central part, which takes into account the LSP and the decay products of the multiple τ_h, and the VBF part, which cuts on the kinematic properties of the jets coming from a VBF process.

There are some differences this analysis has with the other existing VBF searches with final states to light leptons. The most important ones are the substantially tighter requirements on the τ_h isolation and p_T, which allows a good QCD background suppression while remaining efficient with the trigger online requirements. However those requirements leads also to a reduction in the signal acceptance, for that reason a looser $\not\!\!E_T$ cut is introduced.

The selected events are required to have at least two τ_h candidates as defined in Section 4.2. The reconstruction of more than two τ_h is constrained by the trigger. The like sign τ_h candidates with the highest p_T and separated from each other by a minimum $\Delta R = 0.3$ are then chosen to form a di-τ_h candidate. Further, to reduce top pair contamination the event is required not to have any jet identified as a b–quark jet by the b–tagging algorithms using the *c*ombined secondary vertex loose (CSVL) working point.

Reconstructed jets are required not to overlap with identified electrons, muons, or τ_h within $\Delta R < 0.5$, and to pass two levels of jet identification criteria: (i) misidentified jets, mainly generating from calorimeter noise, are rejected by requiring reconstructed jets to pass a set of loose jet identification criteria [53] and (ii) jets originating from pileup interactions are rejected through an MVA-based jet identification discriminant, based on information about the vertex and energy distribution within the jet [54]. Only jets with $p_T \geq 30$ GeV and separated from the taus in the di–τ_h pairs by $\Delta R \geq 0.3$ are searched for b–tags. The p_T cut of 30 GeV on b-jets (a looser veto requirement than other analyses

with light leptons) allows to be more efficient with respect to the signal since the higher p_{T} threshold on taus reduces the contamination of $t\bar{t}$ to a large extent. Further, the event is required to have at least 30 GeV of $\not{E}_{\mathrm{T}}$ in order to further reduce QCD contamination. All the selections described above is what will be referred to as *central selections*.

Subsequently, the following event-wide requirements are imposed. The *VBF selections* are imposed by requiring at least two jets as defined in Section 4.1.4. Only jets separated from the leptons in the τ_{h} τ_{h} pair by $\Delta\mathrm{R} \geq 0.3$ are considered. All jet candidates passing the above requirements and having $|\Delta\eta| \geq 4.2$ and $\eta_1 \cdot \eta_2 < 0$ are combined to form di-jet candidates. The final and the most important of the requirement is an invariant mass of the di-jet candidate, denoted m_{jj}, above the threshold of 250 GeV. In order to increase the event acceptance the analysis code algorithm takes into account every possible di-jet candidate combination and chooses the one that passes the VBF requirements and has the highest m_{jj}.

For better visualization and understanding all the selection criteria are summarized the following way:

- **VBF selection**
  - at least two jets with $p_T^{jet} \geq 30$ GeV, $|\eta_{jet}| \leq 5$ and loose jetID
  - $|\Delta\eta(jet, jet)| > 4.2$
  - $sign(\eta^{jet1} \cdot \eta^{jet2}) = -1$
  - $m_{jj} > 250$ GeV
- **Central selection**
  - Trigger: `HLT_DoubleMediumIsoPFTau35_Trk*_eta2p1_Prong1_v*`
  - two one-prong hadronically decaying τ with $p_{\mathrm{T}} \geq 45$ GeV
  - $\not{E}_{\mathrm{T}} > 30$ GeV
  - $\Delta R(jet, \tau) \geq 0.3$
  - b-tag veto

6.4 Data-Driven QCD background determination

The QCD background contribution for the like-sign di-τ_{h} channel is done using a ABCD data-driven approach. This method consist in dividing the analyzed data in different exclusive regions, defined by two variables. The first variable is the τ_{h} isolation discriminator used in the object reconstruction, namely:

1. Tight (T) isolated τ_{h} for `byTightIsolationMVA3newDMwLT`;
2. Medium (M) isolated τ_{h} for `byMediumIsolationMVA3newDMwLT` but failed `byTightIsolationMVA3newDMwLT`;
3. Loose (L) isolated τ_{h} for `byLooseIsolationMVA3newDMwLT` but failed `byTightIsolationMVA3newDMwLT` and `byMediumIsolationMVA3newDMwLT`.

Each event with a successfully reconstructed LS di-τ_{h} pair falls into a exclusive isolation region as shows on Figure 6.2:

- 2T or signal region (SR) consisting of two tight isolated τ_h;
- One Tight (1T) isolated τ_h region consisting of one tight isolated τ_h and an additional medium or loose isolated τ_h;
- Anti Tight (AT) isolation region consisting of at least one medium isolated τ_h and an additional medium or loose isolated τ_h;
- Anti Medium (AM) isolation region consisting of two loose isolated τ_h.

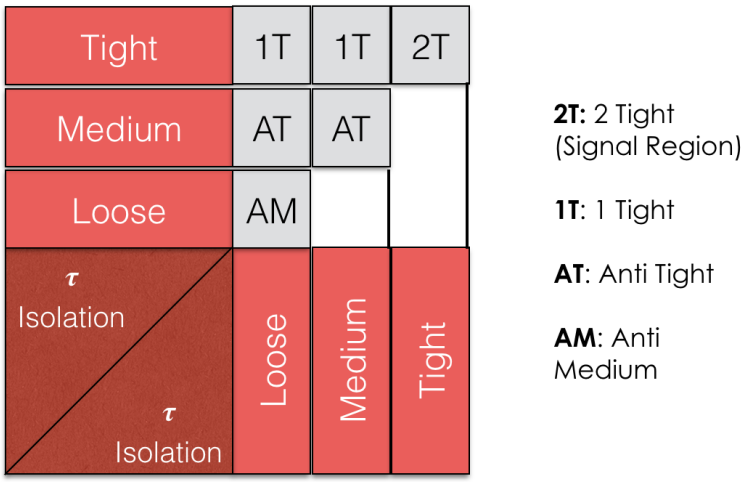

Figure 6.2: Definitions of the exclusive isolation region depending on the isolation of each of the τ_h where 2T is Two Tight consists two tight isolated τ_h (used in the definition of Signal Region), 1T is One Tight isolated Tau region consisting of one tight isolated τ_h and an additional medium or loose isolated τ_h, AT is Anti Tight isolation region consisting of at least one medium isolated τ_h and an additional medium or loose isolated τ_h, AM is Anti Medium isolation region consisting of two loose isolated τ_h

The second dimension of exclusivity is based on the VBF cuts described in 6.3. The regions are defined the following way:

- VBF region: consisting of all the events that passed all VBF cuts previously mentioned in section 6.3;
- VBF inverted region: consisting of all the events that at least fails one of the VBF cuts previously mentioned.

Using these definitions one signal region (SR) and seven control regions (CR) are defined as shown in Figure 6.3. The SR falls into the region defined by two tight isolated τ_h and all the VBF cuts applied, close to it the control region two (CR2) features the same

τ_h isolation requirements but inverted VBF selection requirement. The remaining control regions are defined as CR3 (One Tight isolation region), CR5 (Anti Tight isolation region) and CR7 (Anti Medium isolation region) followed by their corresponding VBF-inverted control regions CR4, CR6, CR8.

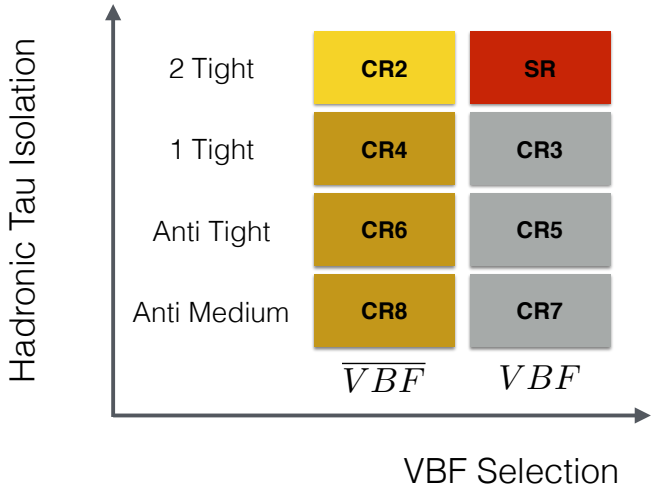

Figure 6.3: Definition of Signal and Control Regions using different τ_h isolation criteria and VBF selection.

The estimation of the events in the signal region is equivalent to the classic ABCD method consisting in counting the number of events in CR2 and multiplying it with a proper conversion factor. This estimation method has been developed under the following assumptions:

- The VBF selection efficiency is independent from any trigger efficiency concerning τ_h isolation such that each contribution to the numerator and denominator cancels out;
- The VBF selection efficiency is also independent from any $\not{E}_T$ cut applied in order to reduce QCD background contributions.

The predicted number of QCD events in the signal region N_{SR}^{QCD} is defined as:

$$N_{SR}^{QCD} = \left(N_{CR2}^{DATA} - N_{CR2}^{\overline{QCD}BG}\right) * \left[\frac{\epsilon_{VBF}^{QCD}}{1 - \epsilon_{VBF}^{QCD}}\right] \tag{6.1}$$

where N_{CR2}^{DATA} is the number of data events in CR2, $N_{CR2}^{\overline{QCD}BG}$ is the number of all non-QCD Monte Carlo samples events in CR2 and ϵ_{VBF}^{QCD} is the efficiency of VBF cuts in a lower τ_h isolation region.

The ϵ_{VBF}^{QCD} for each of the different τ_h isolation region is with the following equation.

$$\epsilon_{VBF}^{QCD} = \frac{N_{VBFCR}^{DATA} - N_{VBFCR}^{\overline{QCD}BG}}{\left(N_{VBFCR}^{DATA} - N_{VBFCR}^{\overline{QCD}BG}\right) + \left(N_{\overline{VBF}CR}^{DATA} - N_{\overline{VBF}CR}^{\overline{QCD}BG}\right)} \tag{6.2}$$

where N_{VBFCR}^{DATA} is the number of the events in data for a given τ isolation region and VBF region, $N_{VBFCR}^{\overline{QCD}BG}$ is the number of all non-QCD Monte Carlo events for a given τ isolation region and VBF region, $N_{\overline{VBF}CR}^{DATA}$ is the number of events in data in the same isolation Control Region but inverted VBF region and$N_{\overline{VBF}CR}^{\overline{QCD}BG}$ is the number of all non-QCD Monte Carlo events for a given τ isolation region but inverted VBF region. In order to increase statistics the $\not{E}_{\mathrm{T}}$ cut has been removed for CR3 to CR7.

Using the events in the defined control regions coming from Table 6.1 as input for Equation 6.1 and Equation 6.2 is possible to determine three independent predictions for the QCD background contribution, one for each pair of tau isolation control regions below the two-tight isolation region. Table 6.1 shows the event counting for all the control regions previously defined for data and all Monte Carlo samples. All the numbers except the ones coming from the QCD sample are used as input for the QCD background estimation method. All the statistical uncertainties are propagated accordingly. For each of the three different τ isolation regions out of the signal region (1T, AT, AM) an independent measurements of ϵ_{VBF}^{QCD} and prediction for N_{SR}^{QCD} is made. A validation of the data-driven background prediction is performed using a simulation-driven approach. Details and results on this methods are given in section 6.5.

Three sources of systematic uncertainty have been considered in the estimation of the QCD contamination in the signal region shown in Equation 6.1. The first source comes from the uncertainty over the generated Monte Carlo samples used in the analysis. The two remaining ones come from the assumptions about the stability of the ϵ_{VBF}^{QCD}, made when defining the data-driven method, one in regard to the relaxation of the tau-identification and the other in regard to a loosening of the $\not{E}_{\mathrm{T}}$ cut, since the ϵ_{VBF}^{QCD} is calculated in CRs where no $\not{E}_{\mathrm{T}}$ cut is applied.

The uncertainty given by a systematic error in the Monte Carlo simulation is estimated by checking the maximal variation over ϵ_{VBF}^{QCD} and N_{SR}^{QCD} after scaling non-QCD contributions by ± 50 %.

The remaining systematics uncertainties on the ϵ_{VBF}^{QCD} are estimated using a simulation-based approach as described in subsection 6.5.2.

6.5 Validation of the Data Driven method

The data-driven background estimation method, as previously shown, offered a possibility to circumvent the scarce statistics of the simulated QCD samples. The results given in section 6.7 can be backed by a simulation based approach which come with two main advantages. First, this it can confirm the assumption made for the data-driven method which states that all control regions and the signal region are indeed dominated by QCD events. Second, this approach can show that VBF efficiency ϵ_{VBF}^{QCD} defined in Equation 6.2 is independent, within the systematic uncertainty, with respect to a selection over $\not{E}_{\mathrm{T}}$ or τ_{h} transverse momentum. This section will give a brief description and results of this simulation based approach as presented in the PhD thesis of Denis Rathjens [96].

Sample	Events (CR2)	Events (CR3)	Events (CR4)	Events (CR5)	Events (CR6)
Data	109	39	737	22	312
Drell-Yan	1.3 ± 1	0.042 ± 0.0077	0.65 ± 0.045	0.002 ± 0.00076	0.029 ± 0.0037
VV	0.7 ± 0.09	0.035 ± 0.017	0.6 ± 0.1	0.0031 ± 0.001	0.045 ± 0.015
W+Jets	6.6 ± 0.17	0.83 ± 0.055	10 ± 0.2	0.081 ± 0.0096	0.89 ± 0.034
Single t	0.25 ± 0.017	0.057 ± 0.008	0.47 ± 0.02	0.011 ± 0.00076	0.1 ± 0.0028
$t\bar{t}$	1.4 ± 0.051	0.19 ± 0.013	2.5 ± 0.059	0.04 ± 0.0024	0.52 ± 0.0095
Higgs	0.012 ± 0.0048	0.0029 ± 0.0023	0.012 ± 0.0044	$2.7 \cdot 10^{-05} \pm 1.1 \cdot 10^{-05}$	$0.00018 \pm 2.2 \cdot 10^{-05}$
QCD	54 ± 1.2	47 ± 1.9	$3.4 \cdot 10^{+02} \pm 4$	19 ± 0.68	$1.4 \cdot 10^{+02} \pm 1.6$
Total $\overline{QCD}$ Monte Carlo	10 ± 1	1.2 ± 0.06	15 ± 0.24	0.14 ± 0.01	1.6 ± 0.038

Table 6.1: Number on events in all the defined control regions for data and all Monte Carlo samples used for the estimation of N_{SR}^{QCD}

Sample	Events (CR7)	Events (CR8)
Data	17	184
Drell-Yan	0.0012 ± 0.00057	0.013 ± 0.0021
VV	0.0011 ± 0.00014	0.033 ± 0.016
W+Jets	0.036 ± 0.0051	0.35 ± 0.015
Single t	0.0061 ± 0.00045	0.058 ± 0.00087
$t\bar{t}$	0.022 ± 0.00079	0.32 ± 0.0054
Higgs	$4.9 \cdot 10^{-06} \pm 2.3 \cdot 10^{-06}$	$5.7 \cdot 10^{-05} \pm 1 \cdot 10^{-05}$
QCD	15 ± 0.81	$1.1 \cdot 10^{+02} \pm 1.7$
Total nonQCD Monte Carlo	0.067 ± 0.0053	0.77 ± 0.023

Variable	One Tight region	Anti-Tight region	Anti-Medium
ϵ_{VBF}^{QCD}	0.05 ± 0.008	0.066 ± 0.014	0.085 ± 0.02
N_{SR}^{QCD}	5.2 ± 1	6.9 ± 1.7	9.1 ± 2.5

Table 6.2: Values for ϵ_{VBF}^{QCD} and N_{SR}^{QCD} for different τ isolation regions.

6.5.1 The simulation-based method

A solution to the scarce statistics of the QCD sample in the signal region can be solved by taking all the events with at least four reconstructed jets and assigning to each one of them an event weight . This weight is a function of the probabilities that two of those four reconstructed jets will fake an τ_{h}:

$$w_{\mathrm{event}}^{TT} = \sum_{i=0}^{N} P(\mathrm{iso} \mid \mathrm{jet}_i) \left(\sum_{j=0;j\neq i}^{N} P(\mathrm{iso} \mid \mathrm{jet}_j) \left[\prod_{k=0;k\neq i,j}^{N} (1 - P(\mathrm{iso} \mid \mathrm{jet}_k)) \right] \right) \tag{6.3}$$

where $P(\mathrm{iso} \mid \mathrm{jet})$ is the probability for a given jet to fake an τ_{h} with a given isolation:

$$P(\mathrm{iso} \mid \mathrm{jet}_i) = P(\mathrm{iso\ ID} \mid \mathrm{jet}_i) \cdot P(p_{\mathrm{T}}^{\tau_{\mathrm{h}}(\mathrm{fake})} > 45\ \mathrm{GeV} \mid \mathrm{jet}_i) \cdot \epsilon^{\mathrm{trigger}}(\mathrm{ID}) \tag{6.4}$$

where $P(\mathrm{iso\ ID} \mid \mathrm{jet}_i)$ is the probability for a given jet to fake a τ_{h} with a given TauID selection besides the p_{T} requirement, $P(p_{\mathrm{T}}^{\tau_{\mathrm{h}}(\mathrm{fake})} > 45\ \mathrm{GeV} \mid \mathrm{jet}_i)$ is the probability for a given jet reconstructed as fake-τ_{h} to pass the requirement of $p_{\mathrm{T}}(\tau_{\mathrm{h}}) > 45$ GeV and $\epsilon^{\mathrm{trigger}}(\mathrm{ID})$ is the efficiency of the trigger ,the one used in the analysis, in selecting events with at least four jets.

The most optimal way to represent $P(\mathrm{iso\ ID} \mid \mathrm{jet}_i)$ is through a parametrization of the most significant jet variables. Closure studies done over different types of parametrization shows that the best parameters choice is the jet candidate p_{T} and the its charged hadron fraction F_q, defined as the momentum of all charged jet components relative to the overall jet momentum.

It is not granted that a jet ,with $p_{\mathrm{T}}(\tau_{\mathrm{h}}) > 45$ GeV, which gets mis-reconstructed offline as τ_{h} passes also the TauID p_{T} selection. Several are the reasons behind this effect. The most important one is that jets have energy corrections while $\tau_{\mathrm{h}}^{\mathrm{fake}}$ do not, which directly translates into slight deviations of the reconstructed object directions. It is possible to correct the τ_{h} transverse momentum by a factor to match the p_{T} from the original jet. It is also important to correct the mass of the $\tau_{\mathrm{h}}^{\mathrm{fake}}$ by a factor which takes into account the difference in size of the reconstruction cone used for the jet and τ_{h} objects.

The last of the corrections is the efficiency of the di-τ trigger in selecting events with two fake τ_{h}, $\epsilon^{\mathrm{trigger}}(\mathrm{ID})$. This efficiency is derived for a single $\tau_{\mathrm{h}}^{\mathrm{fake}}$ from a study over W+jets events where one of the jets fakes an τ_{h}.

This method, also called "dicing", is applied for QCD samples and W+jet samples, in the case where only one of the jets is reconstructed as $\tau_{\mathrm{h}}^{\mathrm{fake}}$. Figure 6.4 and Figure 6.5 show a very good agreement between data and Monte Carlo for di-τ_{h} and $\not{E}_{\mathrm{T}}$ distributions in control region 2 for OS channel. All shown QCD distributions are scaled in order to exactly match the difference between the amount of data measured to the amount of non-QCD background events expected in the control region with the exception of the signal region where the scaling is done to the prediction of the ABCD method performed on data [96].

6.5.2 ϵ^{VBF}-stability with regard to τ_h-isolation and E_T^{miss}-cuts

The efficiency of the VBF selection ϵ^{VBF} has been defined under the assumptions that is independent, within statistical uncertainty, from a selection over $\not{E}_{\mathrm{T}}$ and τ_{h} isolation.

A study on the efficiency stability as function of the second leading τ_{h} momentum is

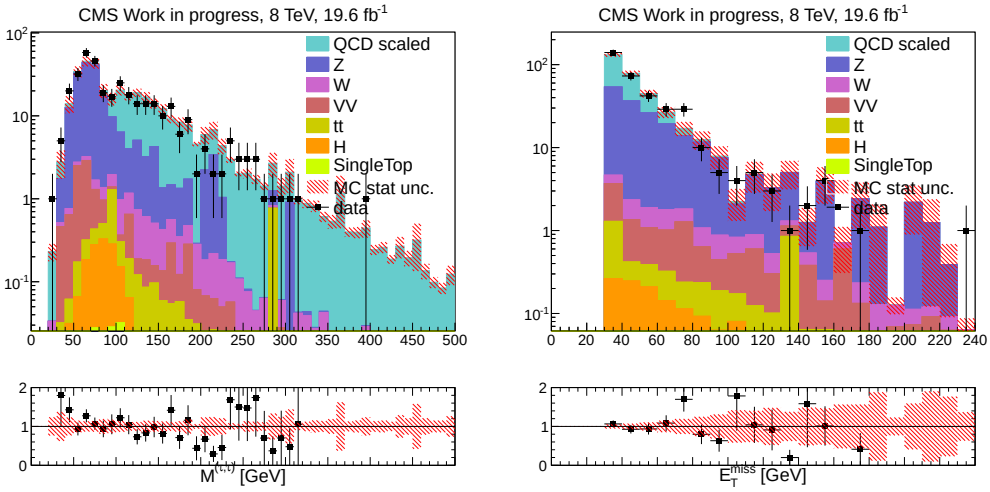

Figure 6.4: (Left) di-τ_h invariant mass and (Right) $\not{E}_T$ distribution for control region 2 (OS channel).

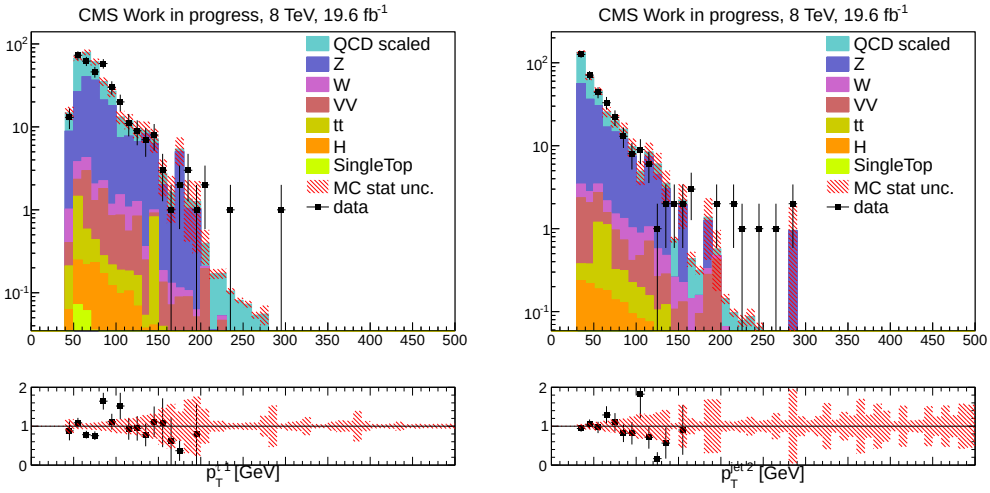

Figure 6.5: (Left) Leading τ_h traverse momentum and (Right) next to leading jet transverse momentum for control region 2 (OS channel).

done using the "diced" QCD sample over different tau isolation requirements as shown on Figure 6.6. The chosen τ_h isolation selection is requiring two tight isolated τ_h (TT) or one tight plus one medium isolated τ_h (TM_I). This study shows that in the case only two additional jets are required in the event selection a slight disagreement is observed for different isolation selections and is taken into account as systematic uncertainty.

An additional stability study is performed over the "diced" QCD sample by considering the deviation of the weighted arithmetic mean of ϵ^{VBF} with respect to $\not{E}_T$ as shown in Figure 6.7. A dependence on $\not{E}_T$, caused by the impact of higher jet energy resolution in the forward sections of the detector, is observed. An additional systematic uncertainty is derived in order to take this effect into account.

To summarize, two systematic uncertainties are taken into account in this study:

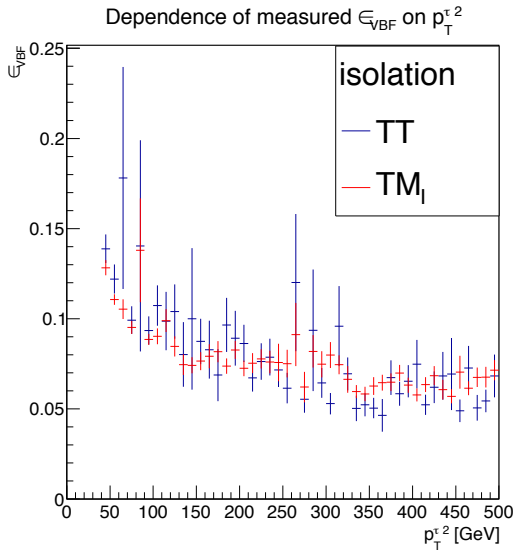

Figure 6.6: Distribution of ϵ^{VBF} against the second to leading τ_{h} momentum in case of two τ_{h} passing a tight (TT) or loose ($\mathrm{TM_I}$) isolation requirement. It can be observed ϵ^{VBF} decreases before stabilizing at high momenta [96].

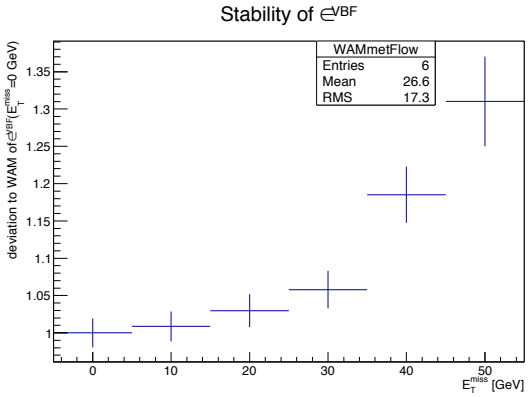

Figure 6.7: Deviation of the weighted arithmetic mean (WAM) of the VBF efficiency of all control region ratios with respect to $\not{E}_{\mathrm{T}}$. A slight quadratic divergence is observed for $\not{E}_{\mathrm{T}} > 30$ GeV [96].

1. Stability of ϵ^{VBF} with respect to τ_{h}-isolation: Maximum relative difference to weighted arithmetic mean at $\not{E}_{\mathrm{T}}$ 30 GeV. This amounts to +17.26% and −7.58% relative uncertainty.

2. Stability of ϵ^{VBF} with respect to $\not{E}_{\mathrm{T}}$-requirement: Relative difference to ϵ^{VBF} within uncertainties of weighted arithmetic mean at no selection on $\not{E}_{\mathrm{T}}$. This amounts to +8.30% relative uncertainty on the upper edge and +3.26% on the lower edge.

6.6 Signal samples systematic uncertanties

The following systematics have been considered while estimating the signal samples contribution in the signal region:

- **Parton Distribution Functions (PDF):** The systematic effect due to imprecise knowledge of the parton distribution functions is determined by comparing CTEQ6.6L [89], MSTW2008nnlo [97], and NNPDF20 PDF [98] with the default PDF and variations within the family of parametrization. The maximal deviation from the central value is used as the overall systematic uncertainty due to PDFs. We obtain a value of 16% on the cross section uncertainty and 23% on the signal acceptance [99].

- **Initial State Radiation (ISR) and Final State Radiation (FSR):** The systematic effect due to imprecise modeling of initial and final state radiation is determined by re-weighting events to account for effects such as missing a terms in the soft-collinear approach [100] and missing NLO terms in the parton shower approach [101]. We obtain uncertainties of 0.9% and 1.2% for ISR and FSR respectively.

- **Luminosity:** We consider a 2.6% uncertainty on the measured luminosity [102].

- **Trigger, Reconstruction, and Selection:** An overall uncertainty is applied for the trigger uncertainties determined on the correction factors described in [103] and which are measured using tag-and-probe methods. We consider 6.8% uncertainty per hadronic tau leg [104]. Scale factors for τ_h identification are taken from the tau POG and obtained using a fit of data in a Z$\rightarrow \tau\tau$ enhanced region and fixing the cross section to that measured using ee/$\mu\mu$. We consider a 100% correlation among the 2 tau legs, therefore we consider 13.6% uncertainty on the signal acceptance.

- ***b*-Tagging Efficiency:** We consider a 30% uncertainty on the mis-tag rate as measured by the b-tagging POG [60]. For the case of our signal, the systematic uncertainty on the requirement of 0 jets mis-tagged as b-jets is determined by propagating the 30% uncertainty on the mis-tag rate through the following equation (which represents the signal efficiency for requiring 0 jets mis-tagged as b-Jets):

$$\epsilon^{\text{NBtag<1}} = 1 - \sum_{n=1} P(n) \cdot \sum_{m=1}^{n} C(n,m) \cdot f^m \cdot (1-f)^{n-m} \tag{6.5}$$

  where $P(n)$ is the probability to obtain n additional jets (non-tau and non-lepton) in the event, $C(n,m)$ the combinatorial of n *choose* m, and f the mis-tag rate. The probability to obtain at least one additional jet in the event is much less than 1%. Therefore, based on the above equation, the mis-tag rate and uncertainty, and the probability to obtain at least one additional jet we calculate a negligible systematic effect on our signal due to the mis-tag rate.

- **Tau Energy Scale:** We consider the effect of the 3% tau energy scale uncertainty measured by the tau POG on the signal acceptance. The tau 4-momentum is scaled by a factor of $k = 1.03$ ($p_{scaled} = k \cdot p_{default}$) and variables are recalculated using p_{scaled}. We find that by using p_{scaled} calculated with a factor of $k = \pm 1.03$, the signal

acceptance fluctuates by 4%. Therefore, we assign a 4% systematic on the signal acceptance due to tau energy scale.

- **Jet Energy Scale:** The uncertainty on jet energy correction (JEC) is the result of a factorized approach on $Anti - k_t$ jets with $R = 0.5$ clustered from Particle Flow (PF) candidates. For MC samples JEC is divided in different steps that take into account several levels of correction. The fist step consist in a single level of corrections (L1) which estimates the p_t offset in bins of η and N_{PV} for AK5PF jets. The second step, known as MC-Truth Corrections, consists in two level of corrections (L2 and L3) converging into an η , p_t dependent scaling factor fully derived from MC after applying L1 corrections. The last step takes into account an L5 correction and uncertainties for individual flavors and predefined mixtures inside the reconstructed jets. We assign a 2% systematic on the signal acceptance due to jet energy scale.

- **Jet Energy Resolution:** The measured jet transverse momentum is never equal to the energy of the original particle due to e.g. a limited detector resolution. This effect is quantified by the jet transverse momentum response R which is defined as $R = p_T/p_T^{particle}$ where p_T denotes the transverse momentum of the jet measured at detector level and $p_T^{particle}$ is the transverse momentum of the original particle-level jet. The average response $\langle R \rangle$ is referred to as jet energy scale and calibrated such that $\langle R \rangle = 1$ for fixed $p_T^{particle}$. The response usually depends on the jet momenta as well as on the pseudorapidity. This is expected since the quality of the jet measurement is directly related to the detector sub-components and the energy of the particles originating e.g. from the track-reconstruction efficiency or the individual amount of detector material. The core of the response is caused by the intrinsic resolution of the various sub-detector components and the precision of the jet clustering algorithms. The response tails are mainly caused by severe jet-mismeasurements [36]. These can be e.g. detector effects like shower leakage or detector noise. Finally, the relative jet transverse momentum resolution is defined as the width of the response distribution corresponding to the gaussian part and hence is a function of p_T and η as well as the total response. One possibility to measure the resolution of the jet transverse momenta in data as well as in simulated events is to utilize the dijet asymmetry A. For events with at least two jets it is defined as:

$$A = \frac{p_{T,1} - p_{T,2}}{p_{T,1} + p_{T,2}} \tag{6.6}$$

For a sufficient number of events the asymmetry is approximately normally distributed and its standard deviation is σ_A. In an ideal dijet topology the two jets are exactly balanced at particle level which leads to an important relation between the width of the asymmetry σ_A and the jet-p_T resolution $\sigma(p_T)$:

$$\frac{\sigma(p_T)}{\langle p_T \rangle} = \sqrt{2}\sigma_A \tag{6.7}$$

Using the latest JER uncertainty collection from `Summer13_V5_DATA_Uncertainty-Sources_AK5PFchs.txt` assign a 4% systematic on the signal acceptance due to jet energy resolution.

- **MET:** The uncertainty on MET for our signal process is driven by the jet energy scale (non-tau jets) (JES), light lepton energy/momentum scale (LES), and unclustered energy (UCE). The systematic effect from MET due to TES, JES and LES is included in the JES, TES, LES systematic uncertainties described above. We find that a 10% uncertainty on the unclustered energy results in at most a 0.5% fluctuation on the signal acceptance.

Source	Initial uncertainty	Signal uncertainty
PDF	—	23%
ISR/FSR	—	1%
Luminosity	2.6%	2.6%
Trigger, ID, Selection	6.8%	16%
Tau Energy Scale	–	4%
b-Jet ID	30%	1%
JES	2% - 10 %	2%
JER	5% - 25 %	4%
MET	10%	0.5%

Table 6.3: Summary of systematic uncertainties

Table 6.3 summarizes all the relevant uncertainties that has been considered for the generated signal samples.

6.7 Results

Following the procedure described in section 6.4, ϵ_{VBF}^{QCD} is calculated for both the opposite-sign (OS) and like-sign (LS) channels. All the uncertainties described in section 6.4 and subsection 6.5.2 have been taken into account and have been properly propagated. The weighted average mean coming from the three different measurements gives the following final result for the like-sign channel:

$$\epsilon_{VBF}^{QCD} = 0.067 \pm 0.0046(stat.)^{-0.00038(MC)+0.0117(\tau iso)+0.0056(MET)}_{+0.00022(MC)-0.0051(\tau iso)+0.0022(MET)} \tag{6.8}$$

Using this result as input for Equation 6.1 gives the final QCD background prediction in signal region:

$$N_{SR}^{QCD} = 7.59 \pm 0.92(stat.)^{-0.42(MC)+1.34(\tau iso)+0.20(MET)}_{+0.35(MC)-0.58(\tau iso)-0.20(MET)} \tag{6.9}$$

The like-sign signal region consist of events satisfying the criteria shown in section 6.3 with the di-τ charge requirement. Table 6.4 shows the contributions in the signal region from all MC samples and data. As described in section 6.5.1, the statistical power of QCD and W+jet background contribution have been increased by "dicing".

QCD is the dominant background and its data-driven prediction shown in Equation 6.9 is fully compatible within statistical and systematic uncertainty with the simulation-driven results shown in Table 6.4. The m_{jj} invariant mass distribution in the like-sign (LS) τ_{h} τ_{h} signal regions is shown in Figure 6.8.

Sample	Events (SR)
Data	9
Drell-Yan	0.037 ± 0.015
VV	0.11 ± 0.065
W+Jets	0.53 ± 0.04
Single t	0.036 ± 0.0066
TTbar	0.11 ± 0.012
Higgs	$0.0005 \pm 7.2e-05$
QCD Prediction	$7.59 \pm 0.92(stat.)^{+1.38}_{-0.72}(syst.)$
Total nonQCD MC	$0.83 \pm 0.079(stat.) \pm 0.41(syst.)$

Table 6.4: Number of events for data and all Monte Carlo contribution in the signal region. The QCD prediction has been corrected for the unidirectional MET-bias described in section 6.5.2 for the combination of the systematic errors.

A combination of the opposite and like-sign signal yields coming from all the different search channels is shown on Table 6.5 and Table 6.6. The added contribution of all the different search channels to the m_{jj} distribution is shown in Figure 6.9 [78]. The observed numbers of events are seen to be consistent with the expected Standard Model background in all search regions. Therefore no excess above the Standard Model is observed.

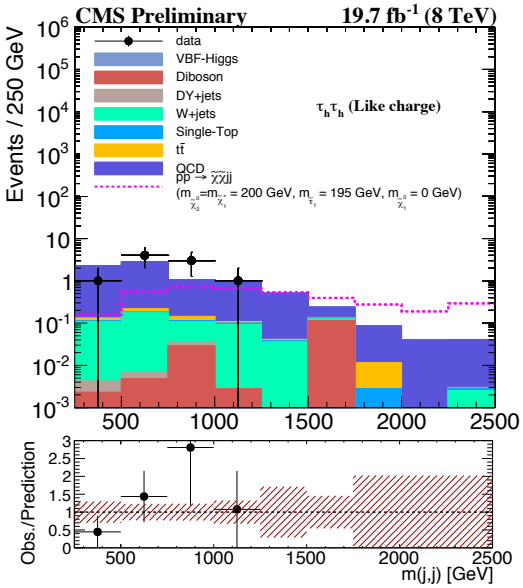

Figure 6.8: The final yields of the like sign di-τ_h channel. The signal scenario with $m(\tilde{\chi}_2^0) = m(\tilde{\chi}_1^\pm) = 200$ GeV , $m(\tilde{\tau}_1) = 195$ GeV , and $m(\tilde{\chi}_1^0) = 0$ GeV, is shown. The signal events are scaled up by a factor of 5 for purposes of visibility. The shaded band in the ratio plot includes the systematic and statistical uncertainties in the background prediction. [78].

Process	$\mu^\pm\mu^\mp jj$	$e^\pm\mu^\mp jj$	$\mu^\pm\tau_h^\mp jj$	$\tau_h^\pm\tau_h^\mp jj$
Z+jets	4.3 ± 1.7	$3.7^{+2.1}_{-1.9}$	19.9 ± 2.9	12.3 ± 4.4
W +jets	<0.1	$4.2^{+3.3}_{-2.5}$	17.3 ± 3.0	2.0 ± 1.7
VV	2.8 ± 0.5	3.1 ± 0.7	2.9 ± 0.5	0.5 ± 0.2
$t\bar{t}$	24.0 ± 1.7	$19.0^{+2.3}_{-2.4}$	11.7 ± 2.8	–
QCD	—	—	—	6.3 ± 1.8
Higgs boson	1.0 ± 0.1	1.1 ± 0.5	—	1.1 ± 0.1
VBF Z	—	—	—	0.7 ± 0.2
Total	32.2 ± 2.4	$31.1^{+4.6}_{-4.1}$	51.8 ± 5.1	22.9 ± 5.1
Observed	31	22	41	31

Table 6.5: Number of observed events and corresponding background predictions for the OS channels. The uncertainties are statistical, including the ones from the control regions and simulated event samples [78].

Process	$\mu^{\pm}\mu^{\pm}jj$	$e^{\pm}\mu^{\pm}jj$	$\mu^{\pm}\tau^{\pm}_{\tau_h}jj$	$\tau^{\pm}_{\tau_h}\tau^{\pm}_{\tau_h}jj$
Z+jets	<0.1	$0^{+1.7}_{-0}$	0.5 ± 0.2	<0.1
W +jets	<0.1	$0^{+3.0}_{-0}$	9.3 ± 2.3	0.5 ± 0.1
VV	2.1 ± 0.3	$1.9^{+0.4}_{-0.2}$	1.1 ± 0.2	$0.1 \pm 6.5 \times 10^{-2}$
$t\bar{t}$	3.1 ± 0.1	$3.5^{+0.7}_{-0.9}$	6.7 ± 2.8	$0.1 \pm 1.2 \times 10^{-2}$
Single top	—	—	—	<0.1
QCD	—	—	—	7.6 ± 0.9
Higgs boson	—	—	—	<0.1
Total	5.4 ± 0.3	$5.4 \pm^{3.5}_{0.9}$	17.6 ± 3.8	8.4 ± 0.9
Observed	4	5	14	9

Table 6.6: Number of observed events and corresponding background predictions for the LS channels. The uncertainties are statistical, including the ones from the control regions and simulated event samples [78].

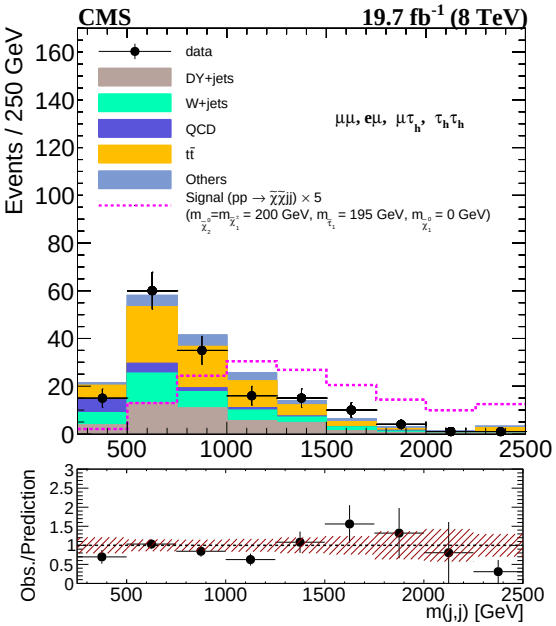

Figure 6.9: Dijet invariant mass distribution for the combination of all search channels. The signal scenario with $m(\tilde{\chi}^0_2) = m(\tilde{\chi}^{\pm}_1) = 200$ GeV , $m(\tilde{\tau}_1) = 195$ GeV , and $m(\tilde{\chi}^0_1) = 0$ GeV, is shown. The signal events are scaled up by a factor of 5 for purposes of visibility. The shaded band in the ratio plot includes the systematic and statistical uncertainties in the background prediction. [78].

6.8 Exclusion limits on chargino/neutralino masses

Upper limits at 95% CL on the cross sections as function of $m_{\tilde{\chi}_2^0} = m_{\tilde{\chi}_1^\pm}$ are set for the τ_h τ_h like-charge and opposite-charge channel. The results are presented using models with uncompressed mass spectrum scenario ($m_{\tilde{\chi}_1^0} = 0$ GeV), a fixed-$\tilde{\tau}_1$-mass assumption ($m_{\tilde{\tau}_1} = m_{\tilde{\chi}_1^\pm} - 5$ GeV) and a $\tilde{\chi}_1^\pm$ mass between $100 \leq m_{\tilde{\chi}_1^\pm} \leq 400$ GeV.

Figure 6.10 shows the upper limit at the 95% CL on the cross-section for opposite and like-sign channel. A combination of the two channels is shown on Figure 6.11. The upper expected limit on $m_{\tilde{\chi}}$ corresponds to the point where the expected limit crosses the theoretical line and is set for $\tilde{\chi}_1^\pm/\tilde{\chi}_2^0$ with masses of 180 GeV. The upper observed limit on $m_{\tilde{\chi}}$ corresponds to the point where the observed limit crosses the theoretical line. In the model considered, $\tilde{\chi}_1^\pm/\tilde{\chi}_2^0$ with masses below 140 GeV are excluded.

The contributions from all the search channels converge in Figure 6.12, showing the expected and observed limits as well as the theoretical cross section as functions of $m_{\tilde{\chi}_1^\pm}$ for, respectively, the fixed- and average-mass $m(\tilde{\tau}_1)$ assumptions. For the compressed-mass spectrum assumption ($m\tilde{\chi}_1^\pm - m_{\tilde{\chi}_1^0} = 50$ GeV), $\tilde{\chi}_2^0$ and $\tilde{\chi}_1^\pm$ gauginos with masses below 170 GeV are excluded. For the average-mass assumption with an uncompressed mass spectrum ($m_{\tilde{\chi}_1^0} = 0$ GeV), the corresponding limit is 300 GeV. These mass limits are conservatively determined using the theoretical cross section minus its one standard deviation uncertainty [78].

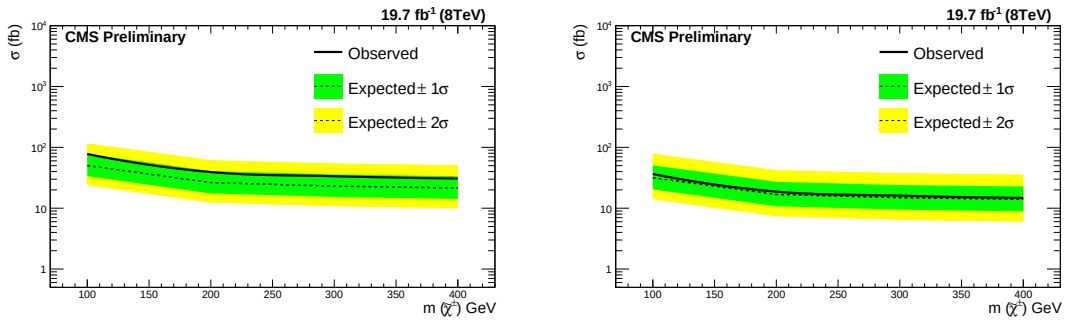

Figure 6.10: Upper limit at the 95% CL on the cross-section as a function of $m_{\tilde{\chi}_2^0} = m_{\tilde{\chi}_1^\pm}$ for the (a) OS $\tau_h\tau_h j_f j_f$, (b) LS $\tau_h\tau_h j_f j_f$ final states. The bands represent the one and two standard deviations obtained from the background-only hypothesis.

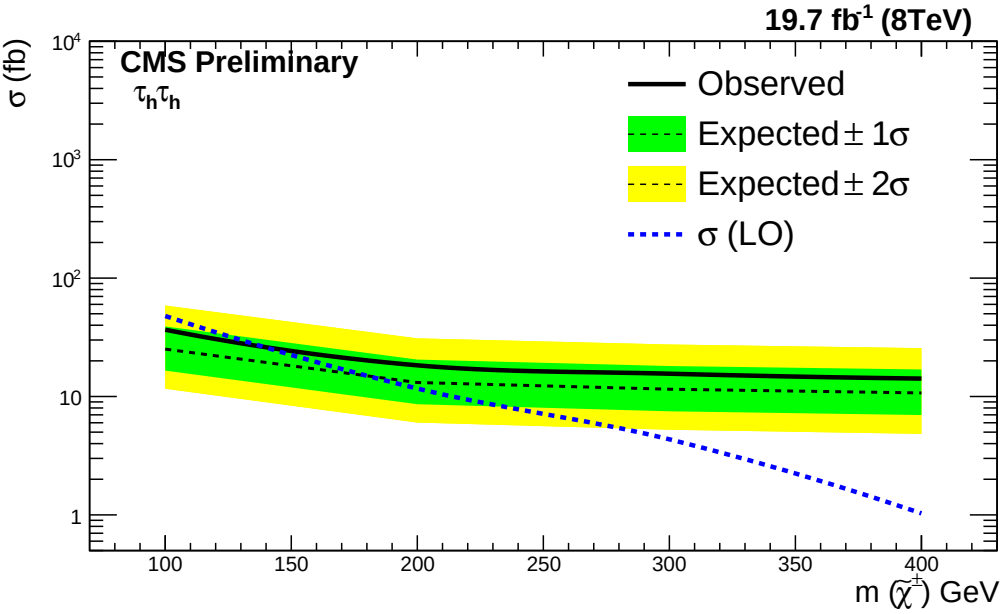

Figure 6.11: Upper limit at the 95% CL on the cross-section as a function of $m_{\tilde{\chi}_2^0} = m_{\tilde{\chi}_1^\pm}$ for the combination of OS and LS $\tau_h\tau_h j_f j_f$ final states. The bands represent the one and two standard deviations obtained from the background-only hypothesis.

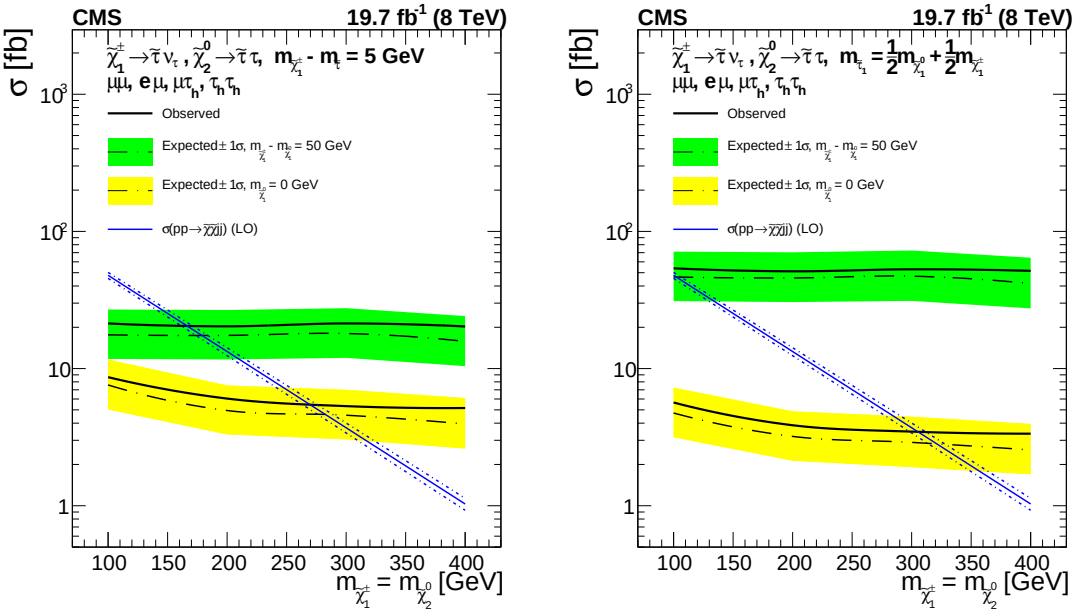

Figure 6.12: Combined 95% CL upper limits on the cross section as a function of $m(\tilde{\chi}_1^{\pm}) = m(\tilde{\chi}_2^0)$. The results for the fixed-mass difference assumption, in which $m(\tilde{\chi}_1^{\pm}) - m(\tilde{\tau}_1) = 5$ GeV, for $m(\tilde{\chi}_1^{\pm}) - m(\tilde{\chi}_1^0) = 50$ GeV (compressed-mass spectrum) and $m(\tilde{\chi}_1^0) = 0$ GeV (uncompressed mass spectrum). (right) The corresponding results for the average-mass assumption, in which $m(\tilde{\tau}_1) = 0.5m(\tilde{\chi}_1^{\pm}) + 0.5m(\tilde{\chi}_1^0)$ [78].

7 Analysis of 13 TeV data

In 2015, After two years of maintenance and upgrades, LHC started the second run phase, also known as *Run2*, featuring an increase of the center of mass energy up to 13 TeV. The goal of this run is to increase the delivery of particle collisions for physics research, and thereby speed the route to potential new physics. A considerable upgrade program has been planned also for the CMS ad ATLAS detectors, featuring the upgrades of many sub-detectors and software tools. It is possible to study the capabilities that searches for SUSY events in vector boson fusion events have using the new hardware and software setup. This chapter describes a sensitivity study of a SUSY VBF search performed using 13 TeV simulated data.

7.1 Signal and background samples

The signal event samples are generated with the `MadGraph v5.2.1` program [80], considering pair production of gauginos with two associated partons. The signal events are generated requiring a pseudorapidity gap $|\Delta\eta| > 4.2$ between the two partons, with $p_{\mathrm{T}} > 30$ GeV for each parton. The signal samples have been generated following all the considerations made for 8 TeV analysis for $\tilde{\chi}_1^{\pm} = \tilde{\chi}_2^0$ masses of 100, 200, 300 and 500 GeV. Two are the assumptions made to fix the $\tilde{\tau}_1$ mass: the fixed-mass and average-mass assumptions. For each of those assumption two different scenarios has been taken into account: the uncompressed mass spectrum and the compressed mass spectrum scenarios.

The Monte Carlo background events used in this study refer to the production run labeled as `RunIISpring15MiniAODv2` and incorporate the `CTEQ10` [105] parton distribution functions (PDF).The `POWHEG` and `MadGraph` generators are interfaced with the `PYTHIA v8.5.12` [90] program, which is used in the matching between the matrix elements, the parton shower, and the hadronization processes.

All Monte Carlo samples are stored in a new format called `miniAOD` [106]. This format is an updated version of the previously used one and includes the new CMS reconstruction features developed between the time of the original analysis and the starting of Run2. A comprehensive list of all the samples used in this study is listed in section A.4.

7.2 Object reconstruction

The upgrade plan commissioned for the CMS detector translates also into an updated version of the physical object definition used for this study with respect to the one used in the 8 TeV analysis.

The τ_{h} object reconstruction went through a major update with the introduction of new isolation and decay mode discriminators and electron veto [107]. Its reconstruction has been commissioned for $p_{\mathrm{T}} > 20$ GeV in all η ranges. Using the specifications suggested by the Tau POG, an increase of the overall TauID efficiency of about 10% for loose isolated τ_{h} with respect to the 8 TeV specifications is achieved, with the reconstruction efficiency

going up to 71% for $Z \longrightarrow \tau\tau$ events [107]. A detailed list of the τ_h object selection can be found in Table A.7.

The Jet object definition remained unchanged with respect to the one used in the 8 TeV analysis.

With Run 2 the experiment gains access to a new trigger list. The aim is to use a trigger that is exclusively making an online selection on the dijet object kinematic properties. Differently with respect to the 8 TeV trigger version, this trigger cannot be seeded by a level one trigger based on $\not{E}_T$. The drop of all online selections over the τ_h properties leads to some important advantages. First, it is possible to have a lower τ_h p_T selection. Second, it is possible to go from a 1-prong to a 3-prong decay selection since this stringent requirement is not a part of any level 1 trigger seed.

The b-tag object reconstruction has an updated discriminator as suggested by the POG [108].

7.3 Cross section limit studies

The aim of this study is to optimize the event cuts is order to exclude signal at the lowest cross section measurable. A cross section limit is made by requiring the so called significance α to:

$$\alpha = 2 \tag{7.1}$$

There are several definitions of significance α available in literature, however the one picked for this 13 TeV study is a frequentist definition based on completely standard concepts [109] which is generally applicable, and has a very clear interpretation. It is particularly suitable for optimization, being independent of a-priori expectations about the presence of a signal, thus allowing the determination of a single set of cuts that is optimal both for setting limits and for making a discovery. The definition of sensitivity is:

$$\alpha = \frac{S}{\frac{a}{2} + \sqrt{B + \left(\frac{B}{2}\right)^2}} \tag{7.2}$$

with a the confidence level expressed in terms of σ, and S and B the number of signal and background events for a given selection. One of the most important features of Equation 7.2 that it is non-diverging in case of $B = 0$.

The number of signal events can be defined as:

$$S = \epsilon \cdot \sigma_{sec} \cdot L \tag{7.3}$$

where ϵ is the efficiency for a given selection criteria, σ_{sec} the cross section of the signal process considered and L the luminosity given by the experiment. Is it possible now to define the efficiency ϵ as function of variables used in the analysis event selection. Three of the most important variables in the 8 TeV analysis has been chosen for this study: $p_T(\tau_h)$, $\not{E}_T$ and m_{jj}. The definition of ϵ in Equation 7.3 now becomes:

$$\epsilon^{signal}(p_T(\tau_h), m_{jj}, \not{E}_T) = \frac{N^{signal}_{passed}(p_T(\tau_h), m_{jj}, \not{E}_T)}{N^{signal}_{total}} \tag{7.4}$$

where N_{passed}^{signal} is the number of signal events passing the selection criteria as a function of the chosen variables and N_{total}^{signal} is the total number of signal events. It is easy to notice that by fixing the significance value as shown on Equation 7.1 the cross section σ_{sec} in Equation 7.3 becomes indeed the cross-section limit σ_{sec}^{lim}. After merging both Equation 7.3 and Equation 7.4 the cross section limit σ_{sec}^{lim} is defined as:

$$\sigma_{sec}^{lim}(p_{\mathrm{T}}(\tau_{\mathrm{h}}), m_{jj}, \not{E}_{\mathrm{T}}) = \frac{\alpha \cdot \left(\frac{a}{2} + \sqrt{B(p_{\mathrm{T}}(\tau_{\mathrm{h}}), m_{jj}, \not{E}_{\mathrm{T}}) + (0.5 \cdot B(p_{\mathrm{T}}(\tau_{\mathrm{h}}), m_{jj}, \not{E}_{\mathrm{T}}))^2}\right)}{\epsilon^{signal}(p_{\mathrm{T}}(\tau_{\mathrm{h}}), m_{jj}, \not{E}_{\mathrm{T}}) \cdot L} \tag{7.5}$$

7.3.1 Event selection

The values for ϵ^{signal} and B are directly taken from the signal and background samples listed in section A.4, on which the event selection has been applied. The idea of this 13 TeV study is to be as close as possible to the one done in 8 TeV, therefore the event selection is very similar to the one described in section 6.3.

As previously mentioned the event selection for this study is a function of the reconstructed tau $p_{\mathrm{T}}, \not{E}_{\mathrm{T}}$ and the di-jet candidate invariant mass m_{jj}, therefore those cuts are considered as free variables in the event selection.

The uncertainties on the official 13 TeV trigger list and on how good are those triggers simulated in Monte Carlo lead to the decision of removing the trigger requirement in the event selection. In case this study will use 13 TeV data it is useful to notice that a choice of a VBF-selection-seeded trigger will lead to an online selection over the di-jet canditates invariant mass m_{jj}.

The di-jet $\Delta\eta$ cut has been removed due to its strong correlation to the di-jet canditates invariant mass m_{jj} as shown in the 8 TeV study [78].

For better visualization and understanding, all the selection criteria are summarized below:

- **VBF selection**
  - at least two jets with $p_T^{jet} \geq 30$ GeV, $|\eta_{jet}| \leq 5$ and loose jetID
  - $\mathrm{sign}(\eta^{jet1} \cdot \eta^{jet2}) = -1$
- **Central selection**
  - two one-prong or three-prong hadronically decaying τ with $p_{\mathrm{T}} = 20, 25, 30, 35, 40, 45$ GeV
  - $\Delta R(jet, \tau) \geq 0.3$
  - b-tag veto

7.3.2 Background estimation

Similar to the analysis at 8 TeV, the largest challenge for this study is to determine the number of background events in the signal region. As described in subsection 5.4.1, the main background contribution is coming from QCD events. The remaining background contributions are considered negligible. Even though this study is characterized by a loosening of the selection cuts with respect to the previous analysis, the limited statistics

of the Monte Carlo samples used gives a very scarce number of selected events. The problem of a limited statistics is solved by estimating the number of background events in the signal region through a two-fold ABCD method. It involves the usage of two distinct correction factors in order to gradually convert the number of background events, taken from a starting control region with looser cuts, into the signal region ones. This method is defined under the same assumptions made for the 8 TeV analysis, listed in section 6.4.

Bearing in mind the idea of developing a method similar to the one used for 8 TeV, the regions are defined by two distinct variables: the isolation of the di-tau candidates and the inversion of the VBF cuts. There are three regions defined for this method. The signal region, also called SR, is defined as the region fulfilling all the cuts listed in subsection 7.3.1. Control region two, also called CR2, has the same selection as the one for the signal region but requires the inversion of the VBF-related cuts. Finally control region three, also called CR3, has the same selection as CR2 but requires the di-tau candidates to have a Loose isolated and a non-isolated τ_h.

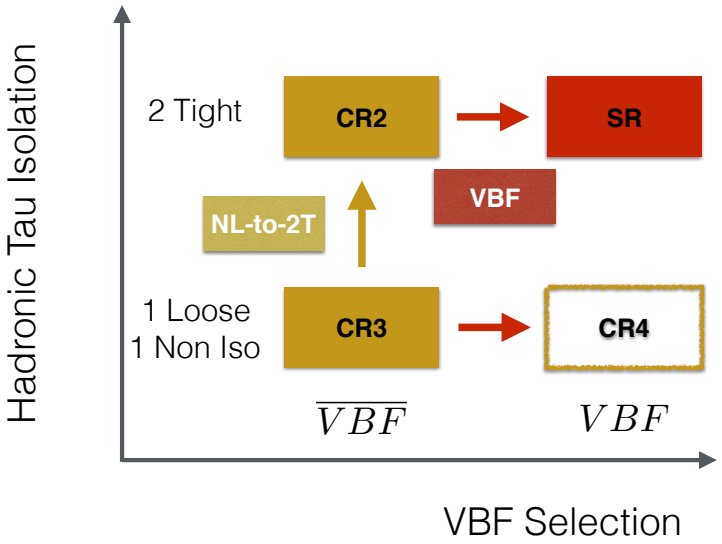

Figure 7.1: Definition of Signal and Control Regions using different τ_h isolation criteria and VBF selection.

As previously mentioned, two conversion factors are used in this method. The first factor, named "*NL-to-2T*" or "*None-Loose to two Tight*", allows to convert the number of selected events from CR3 to CR2. This factor is derived from a study over the same QCD sample where the event population is high by only requiring at least four reconstructed jets in the event, and is defined as:

$$\text{NLto2T} = A \cdot B \tag{7.6}$$

where A and B are ratios. Further, A has as denominator the number of events with at least four jets where at least one of these jets is matched with a loose isolated τ_h. In case this matched τ_h is also tight isolated the events are counted in the numerator:

$$A = \frac{N_{events}(\text{the matched } \tau_{\text{h}} \text{ is also tight isolated })}{N_{events}(= 1\text{jet matched to loose } \tau_{\text{h}})} \tag{7.7}$$

The definition of B is equal to A with the only difference that the τ_{h} matched to a jet in the denominator is non-isolated:

$$B = \frac{N_{events}(\text{the matched } \tau_{\text{h}} \text{ is also tight isolated })}{N_{events}(= 1\text{jet matched to non-isolated } \tau_{\text{h}})} \tag{7.8}$$

The second conversion factor is identical to the VBF conversion factor defined in section 6.4 with the only difference of the updated version of the VBF cuts for the 13 TeV study. This factor is derived from the control regions with a lower τ_{h} isolation requirements such as CR3 and CR4:

$$\text{VBF} = \frac{\epsilon_{VBF}^{QCD}}{1 - \epsilon_{VBF}^{QCD}} \tag{7.9}$$

where ϵ_{VBF}^{QCD} is previously defined in Equation 6.2.

Finally the number of predicted events in the signal region is:

$$B = N_{SR}^{QCD} = N_{CR3}^{MC} \cdot \text{NLto2T} \cdot \text{VBF} \tag{7.10}$$

A representation of the regions and the conversion factor used in this two-fold ABCD method is shown in Figure 7.1.

7.3.3 Systematic and statistical uncertainties

The uncertainty consider for this study originates from the simulated samples. Following the strategy used in the previous analysis this systematic uncertainty is estimated from the variation on the cross-section limit result after considering a $\pm 50\%$ variation of the Monte Carlo statistics.

7.4 Results

The definition of the cross-section limit σ_{sec}^{lim}, as given in Equation 7.5, allows a scan in a three-dimensional space defined by the variables $p_{\text{T}}(\tau_{\text{h}})$, m_{jj} and $\not{E}_{\text{T}}$. The minimum cross-section limit found by the scan gives the optimal event selection cuts for each of the available signal benchmark points. The distribution of the most important analysis variables are shown in Figure 7.2, Figure 7.3, Figure 7.4 and Figure 7.5; for this purpose the cuts over the study variables $p_{\text{T}}(\tau_{\text{h}})$, m_{jj} and $\not{E}_{\text{T}}$ have been removed.

For an easier reading over the results of the cross-section limit study, it is possible to simplify the three-dimensional problem in a "*two plus one*" dimensional one. Following this approach, the cross-section limits are calculated and shown in a two-dimensional plot defined in bins of m_{jj} and $\not{E}_{\text{T}}$. This process is then repeated for each of the chosen $p_{\text{T}}(\tau_{\text{h}})$ cuts.

Each of the two-dimensional bins stores a σ_{sec}^{lim} for the given $p_{\text{T}}(\tau_{\text{h}})$, m_{jj} and $\not{E}_{\text{T}}$ cuts setup. The most important input values to Equation 7.5 are the signal efficiency ϵ^{signal}, as defined in Equation 7.4, and the number of predicted background events B, as defined in

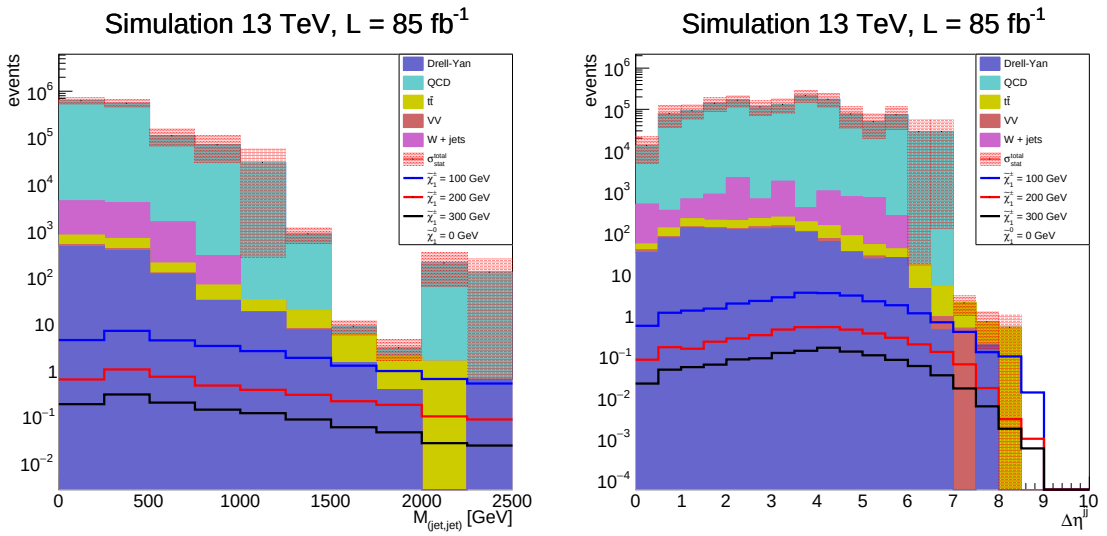

Figure 7.2: (Left) Di-jet invariant mass distribution and (Right) and Di-jet $\Delta\eta$ distribution of selected signal and all MC background samples in signal region.

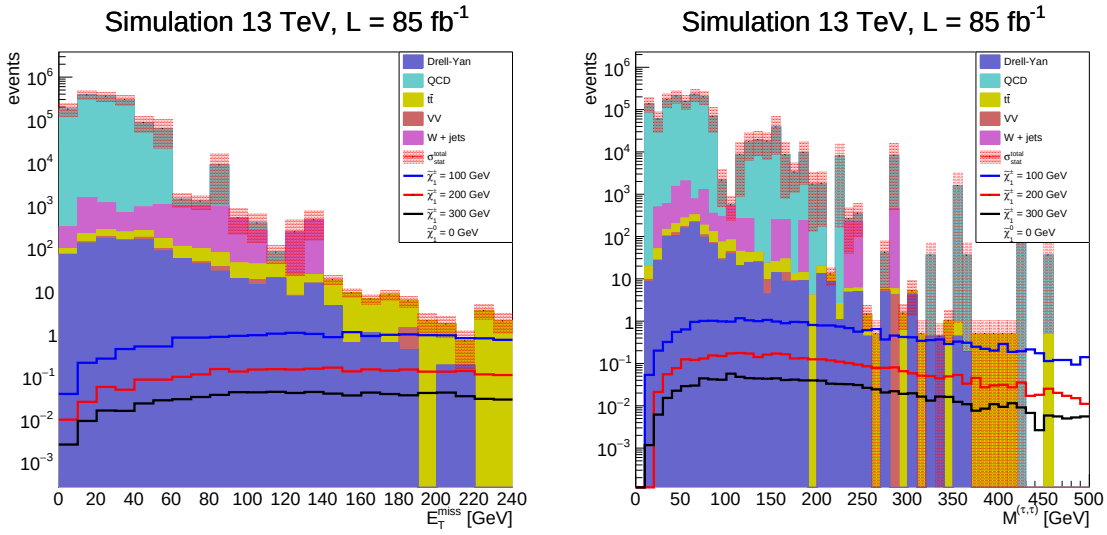

Figure 7.3: (Left) $\not{E}_{\mathrm{T}}$ distribution and (Right) and Di-τ_{h} invariant mass distribution of selected signal and all MC background samples in signal region.

Equation 7.10. The remaining input values are the luminosity L and the confidence level a. The predicted luminosity for the 13 TeV Run [110] is estimated between 75 and 100 fb^{-1}; for the purpose of this study its value has been set to $L = 85$ fb^{-1}. The corresponding value as units of σ with respect to a confidence level of 95% is 2.

A full list of the study results is given as appendix in section A.6. Similarly to what shown in the 8 TeV analysis the cut over the $p_{\mathrm{T}}(\tau_{\mathrm{h}})$ has an high impact on the signal efficiency ϵ^{signal}; for an easier understanding of the final results this cut has been set to its allowed minimum of 20 GeV.

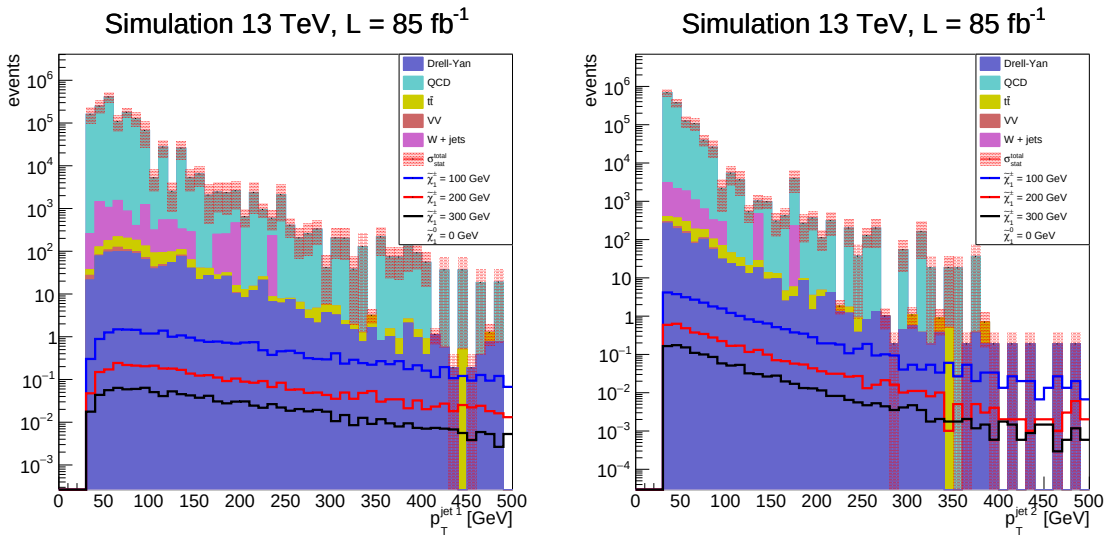

Figure 7.4: (Left) Leading jet p_{T} distribution and (Right) and second leading jet p_{T} distribution of selected signal and all MC background samples in signal region.

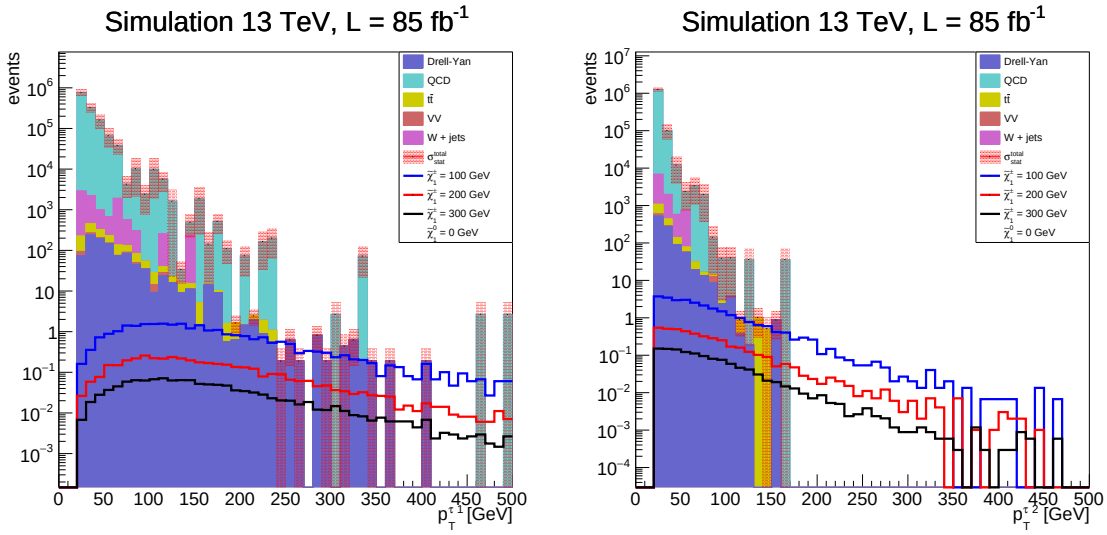

Figure 7.5: (Left) Leading τ_{h} p_{T} distribution and (Right) and second leading τ_{h} p_{T} distribution of selected signal and all MC background samples in signal region.

The best cross-section limit scenario is given for a $\tilde{\chi}_1^{\pm}$ and $\tilde{\chi}_2^0$ mass of 500 GeV for the benchmark point assuming an uncompressed sparticles scenario and an average-$\tilde{\tau}_1$-mass assumption, as shown on Figure 7.6. The cross-section limit minimum value is:

$$\sigma_{lim}^{min} \pm (stat.) \pm (MCsyst.) \pm (VBFsyst.) = 0.017 \pm 0.001^{+0.002+0.001}_{-0.002-0.000}[\mathrm{pb}] \qquad (7.11)$$

for the optimal cuts of $p_{\mathrm{T}}(\tau_{\mathrm{h}}) > 20$ GeV, $m_{jj} > 500$ GeV and $\not{E}_{\mathrm{T}} > 120$ GeV.

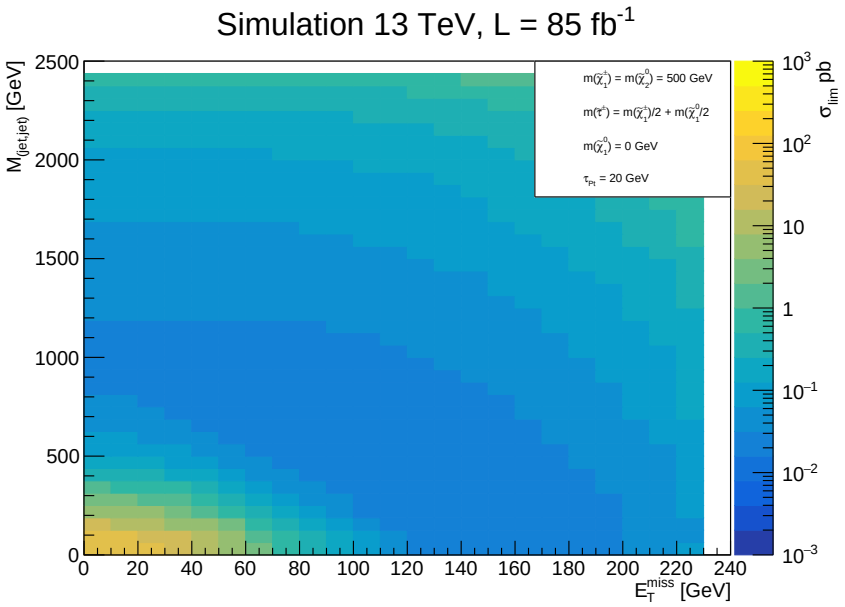

Figure 7.6: Cross section limit as function of m_{jj} and $\not{E}_{\mathrm{T}}$ for $\mathrm{m}(\tilde{\chi}_1^{\pm}) = \mathrm{m}(\tilde{\chi}_2^0) = 500$ GeV, $\mathrm{m}(\tilde{\tau}_1) = 250$ GeV, and $\mathrm{m}(\tilde{\chi}_1^0) = 0$ GeV and an offline selection on $p_{\mathrm{T}}(\tau_{\mathrm{h}}) < 20$ GeV.

For $p_{\mathrm{T}}(\tau_{\mathrm{h}}) > 45$ GeV $\not{E}_{\mathrm{T}} > 30$, $m_{jj} > 250$ GeV, $\mathrm{m}(\tilde{\chi}_1^0) = 50$ GeV		
$\mathrm{m}(\tilde{\chi}_1^{\pm}) = \mathrm{m}(\tilde{\chi}_2^0)$	$\sigma_{lim}^{min} \pm (stat.) \pm (syst.)$ [pb] (**8 TeV**)	$\sigma_{lim}^{min} \pm (stat.) \pm (syst.)$ [pb] (**13 TeV**)
100 GeV	$0.084 \pm 0.016^{+0.18}_{-0.01}$	$0.60 \pm 0.69^{+1.62}_{-0.87}$
200 GeV	$0.14 \pm 0.02^{+0.03}_{-0.04}$	$0.65 \pm 0.74^{+1.74}_{-0.94}$
300 GeV	$1.43 \pm 0.52^{+0.49}_{-0.38}$	$1.19 \pm 1.39^{+3.2}_{-1.71}$

Table 7.1: Cross-section limit comparison between the 8 TeV analysis and the 13 TeV sensitivity study. The chosen values corresponds to an identical selection and signal benchmark points. Cross section limit minimum reached at the given cuts for $p_{\mathrm{T}}(\tau_{\mathrm{h}}) < 45$ GeV $\not{E}_{\mathrm{T}} > 30$, $m_{jj} > 250$ GeV, $\mathrm{m}(\tilde{\chi}_1^0) = 50$ GeV.

By comparing the 8 TeV cross-section limit values with the ones at 13 TeV it is possible to see that the previous analysis performs better in terms of limit setting as shown in Table 7.1. The high statistical and systematic uncertainties shown for 13 TeV are caused by the cut over the $p_{\mathrm{T}}(\tau_{\mathrm{h}})$, which dramatically reduces the QCD statistics. It is worth to mention, however, that the 8 TeV analysis has a selection which in general prevents the comparison in areas of the previously defined three-dimensional phase-space where the 13 TeV analysis is meant to perform better thanks to the more gentle τ_{h} candidate selection.

Another important result from this cross section limit study features the most important signal benchmark point among the ones available that originally gave reason to this analysis design, the one considering a compressed sparticles scenario and the average-$\tilde{\tau}_1$-

mass assumption. A comparison between the cross-section limit values coming from this study and the cross-section limit granted by the CMS collaboration [111] as function of the chargino $\tilde{\chi}_1^{\pm}$ masses shown in Figure 7.7. Given the previously described setup, this analysis is capable of excluding models with chargino masses below $m(\tilde{\chi}_1^{\pm}) = 380$ GeV improving by 80 GeV the limit set by the analysis with 8 TeV data.

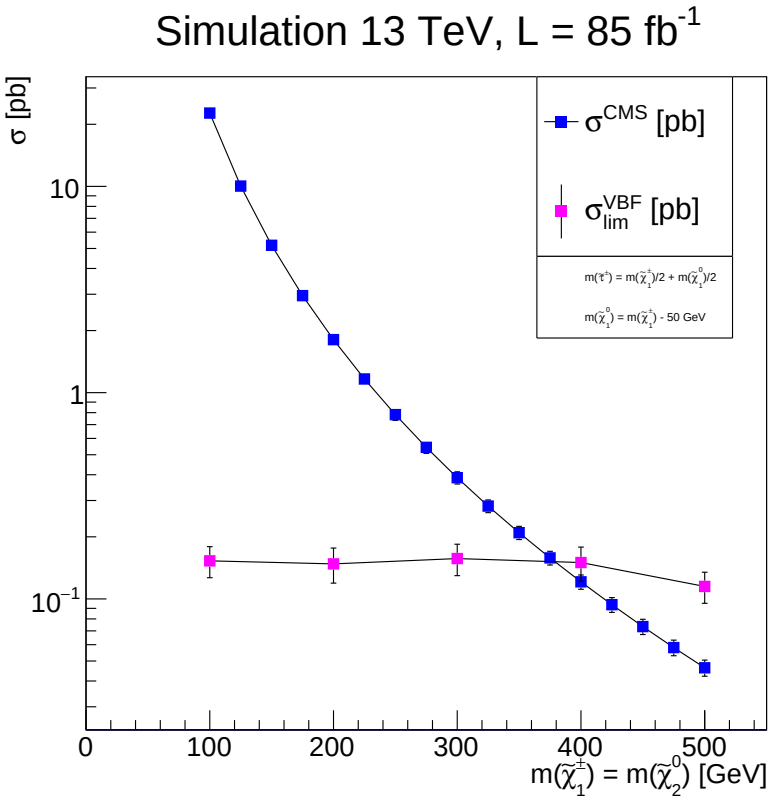

Figure 7.7: Comparison between the cross section limit given by this 13 TeV study and official CMS cross sections calculated using the `resummino` code from B. Fuks et al with CTEQ6.6 and MSTW2008nlo90cl PDFs [112].

To conclude the list of results shown in this chapter an additional study over this last signal benchmark point has been performed. The aim of this final study is to apply a more realistic event selection to see how strong the impact is on the cross section limit. In order to achieve that four different event selection scenarios has been considered, which are meant to resemble the different trigger scenario that can be used in analysis. The first scenario simply adds a cut on the p_{T} of the τ_{h} of 50 GeV, resembling a τ trigger selection as the 8 TeV analysis. The second scenario instead resembles a generic version of a $\not{E}_{\mathrm{T}}$ trigger that is fully efficient at 200 GeV. The third scenario combines a MET trigger with a VBF one by adding the requirement of $\not{E}_{\mathrm{T}} > 150$ GeV with $m_{jj} > 700$ GeV, the angular distance between the two VBF jets candidates $|\Delta\eta(jet, jet)| > 3.6$ and their p_{T} set to 90 GeV. The fourth and final scenario simulates a VBF only trigger by requiring the same selection of the third but dropping the requirement over $\not{E}_{\mathrm{T}}$ and increasing the cut on m_{jj} up to 1000 GeV.

For a better visualization those different scenarios are summarized the following way:

- **Central selection (All scenarios)**
  - two one-prong hadronically decaying τ with $p_{\mathrm{T}} = 20$ GeV
  - at least two jets with $p_T^{jet} \geq 30$ GeV, $|\eta_{jet}| \leq 5$ and loose jetID
  - $\Delta R(jet, \tau) \geq 0.3$
  - b-tag veto
- **VBF selection (All scenarios)**
  - $\mathrm{sign}(\eta^{jet1} \cdot \eta^{jet2}) = -1$

1. **Cut scenario 1**:
   - $p_{\mathrm{T}}(\tau_{\mathrm{h}}) > 50$ GeV;
2. **Cut scenario 2**:
   - $\not{E}_{\mathrm{T}} > 200$ GeV;
3. **Cut scenario 3**:
   - $\not{E}_{\mathrm{T}} > 150$ GeV,
   - $m_{jj} > 700$ GeV,
   - $|\Delta\eta(jet, jet)| > 3.6$,
   - $p_{\mathrm{T}}(jet_1, jet_2) = 90$ GeV;
4. **Cut scenario 4**:
   - $m_{jj} > 1000$ GeV,
   - $|\Delta\eta(jet, jet)| > 3.6$,
   - $pt(jet_1, jet_2) = 90$ GeV.

Comparison between multiple cross section limits coming from the different cut scenarios and the official CMS cross section is shown in Figure 7.8.

The correlation between signal efficiency and the selection over p_{T} (τ_{h}) is once again confirmed by the drop on the cross section limit down to a chargino mass of 230 GeV for cut scenario 1. The introduction of strong cut over m_{jj} combined with a requirement over $\not{E}_{\mathrm{T}}$ (cut scenario 3) greatly impacts the limit setting by scaling down the original one down to a chargino mass of 270 GeV. Similar performance in shown instead in the case where the cuts over those important variables get dissociated as shown for cut set number 2 and 4 with a cross section limit between a chargino mass of 280 and 300 GeV. A summary of the cross section limits for each of the considered scenario is shown on Table 7.2.

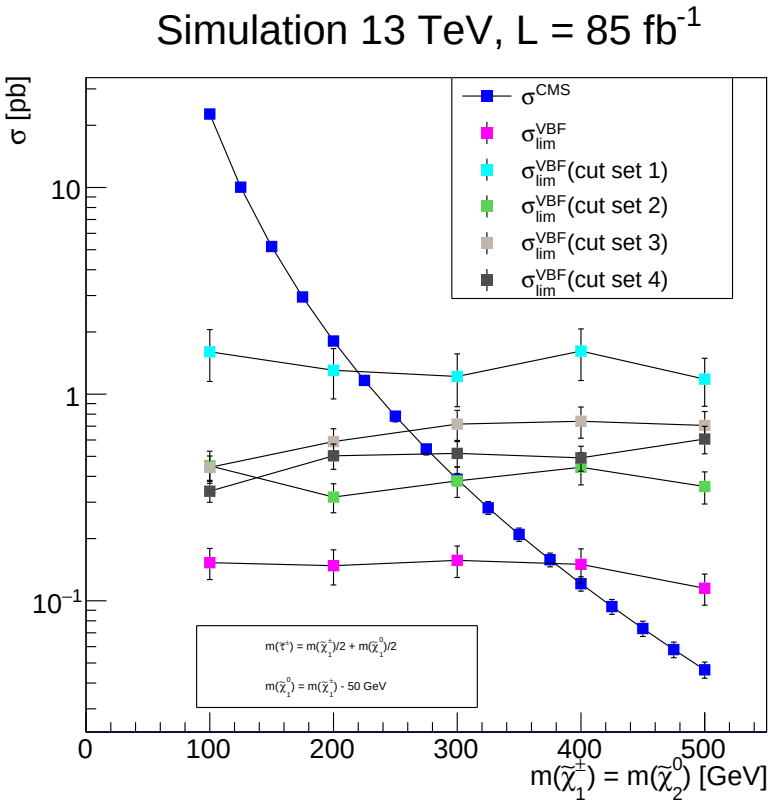

Figure 7.8: Comparison between multiple cross section limits given by different cut scenarios and the official CMS cross sections calculated using the `resummino` code from B. Fuks et al with CTEQ6.6 and MSTW2008nlo90cl PDFs [112].

For $m(\tilde{\tau}^{\pm}) = m(\tilde{\chi}_1^{\pm})/2 + m(\tilde{\chi}_1^0)/2$ and $m(\tilde{\chi}_1^0) = 0$ GeV		
Scenario	Cut	Limit
Original Scenario	Central + VBF selection	380 GeV
Cut Scenario 1	$p_{\mathrm{T}}(\tau_{\mathrm{h}}) > 50$ GeV	230 GeV
Cut Scenario 2	$\not{E}_{\mathrm{T}} > 200$ GeV	300 GeV
Cut Scenario 3	$\not{E}_{\mathrm{T}} > 150$ GeV $m_{jj} > 700$ GeV $\lvert\Delta\eta(jet, jet)\rvert > 3.6$ $p_{\mathrm{T}}(jet_1, jet_2) = 90$ GeV	270 GeV
Cut Scenario 4	$m_{jj} > 1000$ GeV $\lvert\Delta\eta(jet, jet)\rvert > 3.6$ $pt(jet_1, jet_2) = 90$ GeV	300 GeV

Table 7.2: Cross-section limit comparison between the 8 TeV analysis and the 13 TeV sensitivity study. The chosen values corresponds to an identical selection and signal benchmark points. Cross section limit minimum reached at the given cuts for $p_{\mathrm{T}}(\tau_{\mathrm{h}}) > 45$ GeV $\not{E}_{\mathrm{T}} > 30$, $m_{jj} > 250$ GeV, $\mathrm{m}(\tilde{\chi}_1^0) = 50$ GeV.

8 Conclusion

This thesis presented a search for non-colored supersymmetric particles in the vector-boson fusion (VBF) topology using data corresponding to an integrated luminosity of 19.7 fb^{-1} collected with the CMS detector in proton-proton collisions at $\sqrt{s} = 8$ TeV. This is the first search for SUSY in the VBF topology and makes use of events in eight different final states covering both same and opposite sign dilepton pairs. The leptons considered are electrons, muons, and hadronically decaying τ leptons. The VBF topology requires two well-separated jets that appear in opposite hemispheres, with large invariant mass m_{jj}.

The work covered in this thesis predominantly features the background estimation technique for one of the most challenging channels of this search, the same sign di-τ_{h} channel. The QCD background is considered the most relevant contribution and is estimated via a so-called ABCD method utilizing the inversion of VBF jet selection and τ_{h} isolation requirements. This technique was used to predict the QCD background contribution in the signal region to be:

$$N_{SR}^{QCD} = 7.59 \pm 0.92(stat.)^{-0.42(MC)+1.34(\tau iso)+0.20(MET)}_{+0.35(MC)-0.58(\tau iso)-0.20(MET)} \tag{8.1}$$

This number is in full agreement with the measured number of data events. The combined observed m_{jj} distributions do not reveal any evidence for new physics. The results are used to exclude a range of $\tilde{\chi}_1^{\pm}$ and $\tilde{\chi}_2^0$ gaugino masses. For models in which the $\tilde{\chi}_1^0$ lightest supersymmetric particle mass is zero, and in which the $\tilde{\chi}_1^{\pm}$ and $\tilde{\chi}_2^0$ branching fractions to τ leptons are large, $\tilde{\chi}_1^{\pm}$ and $\tilde{\chi}_2^0$ masses up to 300 GeV are excluded at the 95% confidence level. For a compressed-mass-spectrum scenario, in which $m(\tilde{\chi}_1^{\pm}) - m(\tilde{\chi}_1^0) = 50$ GeV, the corresponding limit is 170 GeV. While many previous studies at the LHC have focused on strongly coupled supersymmetric particles, including searches for charginos and neutralinos produced in gluino or squark decay chains, and a number of studies have presented limits on the Drell-Yan production of charginos and neutralinos, this analysis obtains stringent limits on the production of charginos and neutralinos decaying to τ leptons in compressed mass spectrum scenarios defined by the mass separation $\Delta m = m(\tilde{\chi}_1^{\pm}) - m(\tilde{\chi}_1^0) < 50$ GeV.

The sensitivity of the di-τ_{h} channel is predominantly limited by the di-τ_{h} trigger efficiency. Even though the hadronic channel has the best branching ratio fraction from the τ lepton decay, the overall contribution to the combined exclusion limit is small compared to the one of the other lepton channels. With the aim to search for a better trigger strategy for the next run of the analysis, a sensitivity study is performed for the same topology of events using 13 TeV simulated data and an integrated luminosity of 85 fb^{-1}. The first part of this sensitivity study made use of a looser event selection compared to the one used with 8 TeV data, making no requirements on the momentum of the reconstructed tau leptons $p_{\mathrm{T}}(\tau_{\mathrm{h}})$, the missing transverse momentum$\not{E}_{\mathrm{T}}$ or the invariant mass of the di-jet candidatem_{jj}. This study demonstrates the potential for excluding models with $\tilde{\chi}_1^{\pm}$ masses below $m\left(\tilde{\chi}_1^{\pm}\right) = 380$ GeV, particularly for compressed spectra SUSY scenarios. The last part of the sensitivity study has the aim of applying an event selection that falls in line with the available trigger choices the CMS detector for the second part of the data

taking period. The most promising and realistic trigger choice is the one that applies an online selection over the VBF properties of the event. By incorporating this trigger into the analysis, the potential to exclude models with $\tilde{\chi}_1^{\pm}$ masses below $m\left(\tilde{\chi}_1^{\pm}\right) = 280$ GeV for compressed spectra SUSY scenarios is greatly increased.

A Appendix

A.1 Physic Object Recostruction

This section features the detailed list of cuts for all the physical objects used in the 8 TeV analysis following the CMS POG work group recommendations.

A.1.1 Primary Vertices object definition

Table A.1: definition of Vertex.

collection label: recoVertex type: offlinePrimaryVertices	
vertex.size()	> 0

A.1.2 Trigger Paths definition

Table A.2: Trigger paths list.

collection label: TriggerResults_HLT type: edm::TriggerResults	
HLT_DoubleMediumIsoPFTau35_Trk5_eta2p1_Prong1_v2	OR
HLT_DoubleMediumIsoPFTau35_Trk5_eta2p1_Prong1_v3	OR
HLT_DoubleMediumIsoPFTau35_Trk5_eta2p1_Prong1_v4	OR
HLT_DoubleMediumIsoPFTau35_Trk5_eta2p1_Prong1_v6	OR
HLT_DoubleMediumIsoPFTau35_Trk1_eta2p1_Prong1_v1	OR
HLT_DoubleMediumIsoPFTau35_Trk1_eta2p1_Prong1_v3	OR
HLT_DoubleMediumIsoPFTau35_Trk1_eta2p1_Prong1_v4	

A.1.3 Jet object definition

Table A.3: definition of jets.

collection label: selectedPatJets type: pat::Jet		
jet.pt()	>=	30.
fabs(jet.eta())	<=	5.0
jet.neutralHadronEnergyFraction()	<	0.99
jet.neutralEmEnergyFraction()	<	0.99
jet.numberOfDaughters()	>	1
if(fabs(jet.eta()) < 2.4)		
jet.chargedHadronEnergyFraction()	>	0
jet.chargedEmEnergyFraction()	<	0.99
jet.chargedMultiplicity()	>	0
DeltaR(jet,tau)	>=	0.3

A.1.4 b-Jet object definition

Table A.4: definition of b-jets.

collection label: selectedPatJets type: pat::Jet		
jet.pt()	>=	30.
fabs(jet.eta())	<=	2.4
DeltaR(jet,tau)	>=	0.3
jet.bDiscriminator(?)	>	0.244

A.1.5 Tau object definition

Table A.5: definition of τ leptons.

collection label: patTaus type: pat::Tau		
fabs(tau.eta())	<=	2.1
tau.pt()	>=	45.0
tau.leadPFChargedHadrCand()->pt()	>=	5.0
tau.tauID(''byTightIsolationMVA3newDMwLT'')	>	0.5 ||
tau.tauID(''byMediumIsolationMVA3newDMwLT'')	>	0.5 ||
tau.tauID(''byLooseIsolationMVA3newDMwLT'')	>	0.5
(decayModeFindingNewDMs	>	0.5 &&
signalPFChargedHadrCands().size()	==	1)
tau.tauID(''againstElectronMediumMVA5'')	>	0.5
tau.tauID(''againstMuonLoose3'')	>	0.5

A.1.6 MET object definition

Table A.6: definition of $\not{E}_{\mathrm{T}}$

collection label: patMET type: patPfMetT0pcT1Txy		

A.2 Physic Object Recostruction at 13 TeV

This section features the detailed list of cuts for all the physical objects used in the 13 TeV analysis following the CMS POG work group recommendations.

A.2.1 Tau object definition

Table A.7: definition of τ leptons.

collection label: patTaus type: pat::Tau		
fabs(tau.eta())	<=	2.1
tau.pt()	>=	20
tau.leadPFChargedHadrCand()->pt()	>=	5.0
tau.tauID(‘‘byTightIsolationMVArun2v1DBdR03oldDMwLT’’)	>	0.5 ||
tau.tauID(‘‘byMediumIsolationMVArun2v1DBdR03oldDMwLT’’)	>	0.5 ||
tau.tauID(‘‘byLooseIsolationMVArun2v1DBdR03oldDMwLT’’)	>	0.5
(byLooseIsolationMVArun2v1DBnewDMwLT	>	0.5 &&
signalPFChargedHadrCands().size()	<	4)
tau.tauID(‘‘againstElectronMediumMVA6’’)	>	0.5
tau.tauID(‘‘againstMuonLoose3’’)	>	0.5

A.2.2 Jet object definition

Table A.8: definition of jets.

collection label: selectedPatJets type: pat::Jet		
jet.pt()	>=	30.
fabs(jet.eta())	<=	5.0
jet.neutralHadronEnergyFraction()	<	0.99
jet.neutralEmEnergyFraction()	<	0.99
jet.numberOfDaughters()	>	1
if(fabs(jet.eta()) < 2.4)		
jet.chargedHadronEnergyFraction()	>	0
jet.chargedEmEnergyFraction()	<	0.99
jet.chargedMultiplicity()	>	0
DeltaR(jet,tau)	>=	0.3

A.3 Monte Carlo Samples at 8 TeV

Process	Official CMS Datasets /DY*/AODSIM
$Z \longrightarrow \tau\tau$	ToTauTau_M-20_CT10_TuneZ2star_v2_8TeV-powheg-tauola-pythia6/Summer12 DR53X-PU_S10_START53_V7A-v2
$Z \longrightarrow \mu\mu$	ToMuMu_M-20_CT10_TuneZ2star_v2_8TeV-powheg-pythia6/Summer12_DR53X-PU_S10_START53_V7A-v1
$Z \longrightarrow ee$	ToEE_M-20_CT10_TuneZ2star_v2 8TeV-powheg-pythia6/Summer12_DR53X-PU_S10_START53 V7A-v1
$Z \longrightarrow ll$ $(10 < m_{ll} < 50)$	JetsToLL_M-10To50_TuneZ2Star_8TeV-madgraph/Summer12_DR53X-PU_S10_START53_V7A-v1
$Z \longrightarrow ll$ $(m_{ll} > 50)$	JetsToLL_M-50_TuneZ2Star_8TeV-madgraph-tarball/Summer12_DR53X-PU_S10 START53_V7A-v1
$Z \longrightarrow ll + 1jets$	1JetsToLL_M-50_TuneZ2Star_8TeV-madgraph/Summer12_DR53X-PU_S10 START53_V7A-v1
$Z \longrightarrow ll + 2jets$	2JetsToLL_M-50_TuneZ2Star_8TeV-madgraph/Summer12_DR53X-PU_S10_START53_V7A-v1
$Z \longrightarrow ll + 3jets$	3JetsToLL_M-50_TuneZ2Star_8TeV-madgraph/Summer12 DR53X-PU_S10_START53_V7A-v1
$Z \longrightarrow ll + 4jets$	4JetsToLL_M-50_TuneZ2Star_8TeV-madgraph/Summer12 DR53X-PU_S10_START53_V7A-v1
$Z \longrightarrow ll$ EWK	JJ01JetsToLL_M-50_MJJ-200_TuneZ2Star 8TeV-madgraph_tauola/Summer12_DR53X-PU_S10 START53_V7A-v1

Table A.9: Drell Yang simulated samples.

Process	Official CMS Datasets /W*/AODSIM
W + 0 jets	JetsToLNu_TuneZ2Star_8TeV-madgraph-tarball/Summer12_DR53X-PU_S10 START53_V7A-v2
W + 1 jet	1JetsToLNu_TuneZ2Star_8TeV-madgraph/Summer12_DR53X-PU_S10_START53_V7A-v1
W + 2 jets	2JetsToLNu_TuneZ2Star_8TeV-madgraph/Summer12_DR53X-PU_S10_START53_V7A-v1
W + 3 jets	3JetsToLNu_TuneZ2Star_8TeV-madgraph/Summer12_DR53X-PU_S10 START53_V7A-v1
W + 4 jets	4JetsToLNu_TuneZ2Star_8TeV-madgraph/Summer12_DR53X-PU_S10_START53_V7A-v1

Table A.10: W boson plus additional jets simulated samples.

Process	Official CMS Datasets /TTJets*/AODSIM
$t\bar{t}$	MassiveBinDECAY_TuneZ2star_8TeV-madgraph-tauola/Summer12_DR53X-PU_S10_START53_V7C-v1

Table A.11: Standard model top production simulated sample.

Process	Official CMS Datasets */AODSIM
$WW(\longrightarrow 2l2\nu)$	WJetTo2L2Nu_8TeV-powheg-pythia6/Summer12_DR53X-PU_S10_START53_V7C-v1
W^+W^+	/WpWpqq_8TeV-madgraph/Summer12_DR53X-PU_S10_START53_V7A-v1
WW	/WmWmqq_TeV-madgraph/Summer12_R53X-PU_10_START53_V7A-v1
WW double scattering	/WW_DoubleScattering_8TeV-pythia8/Summer12_DR53X-PU_S10_START53_V7A-v1
WW EWK	/WWjjTo2L2Nu_8TeV_madgraph_qed6_qcd0/Summer12_DR53X-PU_S10__V19-v1
WZ $(\longrightarrow 2q2\nu)$	/WZJetsTo2Q2Nu_TuneZ2star_8TeV-madgraph-tauloa/Summer12_DR53X-PU_S10_START53_V7A-v1
WZ $(\longrightarrow 2l2\nu)$	/WZJetsTo2L2Nu_TuneZ2star_8TeV-madgraph-tauloa/_DR53X-PU_S10_START53_V7A-v1
WZ $(\longrightarrow 3l)$	/WZJetsTo3L_TuneZ2star_8TeV-madgraph-tauloa/Summer12_DR53X-PU_S10 START53_V7A-v1
ZZ $(\longrightarrow 2q2\nu)$	/ZZJetsTo2Q2Nu_TuneZ2star_8TeV-madgraph-tauloa/Summer12_DR53X-PU_S10_START53_V7A-v1
ZZ $(\longrightarrow 2l2\nu)$	/ZZJetsTo2L2Nu_TuneZ2star_8TeV-madgraph-tauloa/Summer12_DR53X-PU_S10_START53_V7A-v1
ZZ $(\longrightarrow 2l2q)$	/ZZJetsTo2L2Q_TuneZ2star_8TeV-madgraph-tauloa/Summer12_DR53X-PU_S10_START53_V7A-v1
ZZ $(\longrightarrow 4l)$	/ZZJetsTo4L_TuneZ2star_8TeV-madgraph-tauloa/Summer12_DR53X-PU_S10_START53_V7A-v1

Table A.12: Standard model production of two vector bosons simulated samples.

Process	Official CMS Datasets /VBF */AODSIM
$H \longrightarrow WW(\longrightarrow 2l)$	HToWWTo2LAndTau2Nu_M-125_8TeV-powheg-pythia6/Summer12_DR53X-_S10_START53_V7A-v1
$H \longrightarrow ZZ(\longrightarrow 2l2\nu)$	HToZZTo2L2Nu_M-120_8TeV-powheg-pythia6/Summer12_DR53X-PU_S10_START53_V7A-v1
$H \longrightarrow ZZ$ $(\longrightarrow 2l2q)$	HToZZTo2L2Q_M-125_8TeV-powheg-pythia6/Summer12_DR53X-PU_S10_START53_V7A-v1
$H \longrightarrow ZZ$ $(4l)$	HToZZTo4L_M-125_8TeV-powheg-pythia6/Summer12_DR53X-PU_S10_START53_V7A-v1
$H \longrightarrow ZZ$ $(\longrightarrow 4\nu)$	HToZZTo4Nu_M-120_8TeV-pythia6/Summer12_DR53X-PU_S10_START53_V7A-v1
$H \longrightarrow \tau\tau$	HToTauTau_M-125_8TeV-powheg-pythia6/Summer12_DR53X-PU_S

Table A.13: Standard model Higgs production by vector boson fusion simulated samples

Process	Official CMS Datasets /VBF */AODSIM
$bg \longrightarrow tW^-$	/T_tW-channel-DR_TuneZ2star_8TeV-powheg-tauola/Summer12_DR53X-PU_S10 START53_V7A-v1
$bg \longrightarrow tW^+$	/Tbar tW-channel-DR_TuneZ2star_8TeV-powheg-tauola/Summer12_DR53X-PU_S10_START53_V7A-v1
q'b $\longrightarrow$ qt	/T_t-channel_TuneZ2star_8TeV-powheg-tauola/Summer12_DR53X-PU_S10_START53_V7A-v1
$qb \longrightarrow qt$	/Tbar_t-channel_TuneZ2star_8TeV-powheg-tauola/Summer12_DR53X-PU_S10_START53_V7A-v1
qq'$\longrightarrow$ tb	/T_s-channel_TuneZ2star_8TeV-powheg-tauola/Summer12_DR53X-PU_S10_START53_V7A-v1
qq'$\longrightarrow$ tb	/Tbar_s-channel_TuneZ2star_8TeV-powheg-tauola/Summer12_DR53X-PU_S10_START53_V7A-v1

Table A.14: Single top simulated samples.

A.4 Monte Carlo Samples at 13 TeV

Process	Official CMS Datasets QCD*/RunIISpring15MiniAODv2
QCD $100 < H_T < 200$ GeV	HT100to200_TuneCUETP8M1_13TeVmadgraphMLMpythia8/
QCD $200 < H_T < 300$ GeV	HT200to300_TuneCUETP8M1_13TeVmadgraphMLMpythia8/
QCD $300 < H_T < 500$ GeV	HT300to500_TuneCUETP8M1_13TeVmadgraphMLMpythia8/
QCD $500 < H_T < 700$ GeV	HT500to700_TuneCUETP8M1_13TeVmadgraphMLMpythia8/
QCD $700 < H_T < 1000$ GeV	HT700to1000_TuneCUETP8M1_13TeVmadgraphMLMpythia8/
QCD $1000 < H_T < 1500$ GeV	HT1000to1500_TuneCUETP8M1_13TeVmadgraphMLMpythia8/
QCD $1500 < H_T < 2000$ GeV	HT1500to2000_TuneCUETP8M1_13TeVmadgraphMLMpythia8/
QCD $2000 < H_T < \infty$ GeV	HT2000toInf_TuneCUETP8M1_13TeVmadgraphMLMpythia8/

Table A.15: QCD simulated samples.

Process	Official CMS Datasets DYJetsToLL_M50*/RunIISpring15MiniAODv2
DYJetsToLL $100 < H_T < 200$ GeV	HT100to200_Tune4C_13TeVmadgraphtauola/
DYJetsToLL $200 < H_T < 400$ GeV	HT200to400_Tune4C_13TeVmadgraphtauola/
DYJetsToLL $400 < H_T < 600$ GeV	HT400to600_Tune4C_13TeVmadgraphtauola/
DYJetsToLL $600 < H_T < \infty$ GeV	HT600toInf_Tune4C_13TeVmadgraphtauola/

Table A.16: Drell-Yan simulated samples.

Process	Official CMS Datasets WJetsToLNu*/RunIISpring15MiniAODv2
$W + jets \to l + \nu$ $100 < H_T < 200$ GeV	HT100to200_Tune4C_13TeVmadgraphtauola/
$W +$ jets $\to l + \nu$ $200 < H_T < 400$ GeV	HT200to400_Tune4C_13TeVmadgraphtauola/
$W +$ jets $\to l + \nu$ $400 < H_T < 600$ GeV	HT400to600_Tune4C_13TeVmadgraphtauola/
$W +$ jets $\to l + \nu$ $600 < H_T < \infty$ GeV	HT600toInf_Tune4C_13TeVmadgraphtauola/

Table A.17: $W +$ jets $\to l + \nu$ simulated samples.

Process	Simulated Datasets VBFC1pmN2_C1ToTau_N2ToTauTau*/
$pp \longrightarrow \tilde{\chi}_1^{\pm} + \tilde{\chi}_2^0 + 2$ jets $\longrightarrow 3\tau + 2$ jets $m\left(\tilde{\chi}_1^0\right) = 0$ GeV, $m\left(\tilde{\tau}_1\right) = 50$ GeV, $m\left(\tilde{\chi}_1^{\pm}\right) = m\left(\tilde{\chi}_2^0\right) = 100$ GeV	LSP000_Stau050_Chargino100_1M/
$pp \longrightarrow \tilde{\chi}_1^{\pm} + \tilde{\chi}_2^0 + 2$ jets $\longrightarrow 3\tau + 2$ jets $m\left(\tilde{\chi}_1^0\right) = 0$ GeV, $m\left(\tilde{\tau}_1\right) = 95$ GeV, $m\left(\tilde{\chi}_1^{\pm}\right) = m\left(\tilde{\chi}_2^0\right) = 100$ GeV	LSP000_Stau095_Chargino100_1M/
$pp \longrightarrow \tilde{\chi}_1^{\pm} + \tilde{\chi}_2^0 + 2$ jets $\longrightarrow 3\tau + 2$ jets $m\left(\tilde{\chi}_1^0\right) = 0$ GeV, $m\left(\tilde{\tau}_1\right) = 100$ GeV, $m\left(\tilde{\chi}_1^{\pm}\right) = m\left(\tilde{\chi}_2^0\right) = 200$ GeV	LSP000_Stau100_Chargino200_1M/
$pp \longrightarrow \tilde{\chi}_1^{\pm} + \tilde{\chi}_2^0 + 2$ jets $\longrightarrow 3\tau + 2$ jets $m\left(\tilde{\chi}_1^0\right) = 0$ GeV, $m\left(\tilde{\tau}_1\right) = 150$ GeV, $m\left(\tilde{\chi}_1^{\pm}\right) = m\left(\tilde{\chi}_2^0\right) = 300$ GeV	LSP000_Stau150_Chargino300_1M/
$pp \longrightarrow \tilde{\chi}_1^{\pm} + \tilde{\chi}_2^0 + 2$ jets $\longrightarrow 3\tau + 2$ jets $m\left(\tilde{\chi}_1^0\right) = 0$ GeV, $m\left(\tilde{\tau}_1\right) = 195$ GeV, $m\left(\tilde{\chi}_1^{\pm}\right) = m\left(\tilde{\chi}_2^0\right) = 200$ GeV	LSP000_Stau195_Chargino200_1M/
$pp \longrightarrow \tilde{\chi}_1^{\pm} + \tilde{\chi}_2^0 + 2$ jets $\longrightarrow 3\tau + 2$ jets $m\left(\tilde{\chi}_1^0\right) = 0$ GeV, $m\left(\tilde{\tau}_1\right) = 200$ GeV, $m\left(\tilde{\chi}_1^{\pm}\right) = m\left(\tilde{\chi}_2^0\right) = 400$ GeV	LSP000_Stau200_Chargino400_1M/
$pp \longrightarrow \tilde{\chi}_1^{\pm} + \tilde{\chi}_2^0 + 2$ jets $\longrightarrow 3\tau + 2$ jets $m\left(\tilde{\chi}_1^0\right) = 0$ GeV, $m\left(\tilde{\tau}_1\right) = 250$ GeV, $m\left(\tilde{\chi}_1^{\pm}\right) = m\left(\tilde{\chi}_2^0\right) = 500$ GeV	LSP000_Stau250_Chargino500_1M/
$pp \longrightarrow \tilde{\chi}_1^{\pm} + \tilde{\chi}_2^0 + 2$ jets $\longrightarrow 3\tau + 2$ jets $m\left(\tilde{\chi}_1^0\right) = 0$ GeV, $m\left(\tilde{\tau}_1\right) = 295$ GeV, $m\left(\tilde{\chi}_1^{\pm}\right) = m\left(\tilde{\chi}_2^0\right) = 300$ GeV	LSP000_Stau295_Chargino300_1M/
$pp \longrightarrow \tilde{\chi}_1^{\pm} + \tilde{\chi}_2^0 + 2$ jets $\longrightarrow 3\tau + 2$ jets $m\left(\tilde{\chi}_1^0\right) = 0$ GeV, $m\left(\tilde{\tau}_1\right) = 395$ GeV, $m\left(\tilde{\chi}_1^{\pm}\right) = m\left(\tilde{\chi}_2^0\right) = 400$ GeV	LSP000_Stau395_Chargino400_1M/
$pp \longrightarrow \tilde{\chi}_1^{\pm} + \tilde{\chi}_2^0 + 2$ jets $\longrightarrow 3\tau + 2$ jets $m\left(\tilde{\chi}_1^0\right) = 0$ GeV, $m\left(\tilde{\tau}_1\right) = 495$ GeV, $m\left(\tilde{\chi}_1^{\pm}\right) = m\left(\tilde{\chi}_2^0\right) = 500$ GeV	LSP000_Stau495_Chargino500_1M/
$pp \longrightarrow \tilde{\chi}_1^{\pm} + \tilde{\chi}_2^0 + 2$ jets $\longrightarrow 3\tau + 2$ jets $m\left(\tilde{\chi}_1^0\right) = 50$ GeV, $m\left(\tilde{\tau}_1\right) = 75$ GeV, $m\left(\tilde{\chi}_1^{\pm}\right) = m\left(\tilde{\chi}_2^0\right) = 100$ GeV	LSP050_Stau075_Chargino100_1M/
$pp \longrightarrow \tilde{\chi}_1^{\pm} + \tilde{\chi}_2^0 + 2$ jets $\longrightarrow 3\tau + 2$ jets $m\left(\tilde{\chi}_1^0\right) = 50$ GeV, $m\left(\tilde{\tau}_1\right) = 95$ GeV, $m\left(\tilde{\chi}_1^{\pm}\right) = m\left(\tilde{\chi}_2^0\right) = 100$ GeV	LSP050_Stau095_Chargino100_1M/
$pp \longrightarrow \tilde{\chi}_1^{\pm} + \tilde{\chi}_2^0 + 2$ jets $\longrightarrow 3\tau + 2$ jets $m\left(\tilde{\chi}_1^0\right) = 50$ GeV, $m\left(\tilde{\tau}_1\right) = 125$ GeV, $m\left(\tilde{\chi}_1^{\pm}\right) = m\left(\tilde{\chi}_2^0\right) = 200$ GeV	LSP050_Stau125_Chargino200_1M/
$pp \longrightarrow \tilde{\chi}_1^{\pm} + \tilde{\chi}_2^0 + 2$ jets $\longrightarrow 3\tau + 2$ jets $m\left(\tilde{\chi}_1^0\right) = 50$ GeV, $m\left(\tilde{\tau}_1\right) = 175$ GeV, $m\left(\tilde{\chi}_1^{\pm}\right) = m\left(\tilde{\chi}_2^0\right) = 300$ GeV	LSP050_Stau175_Chargino300_1M/
$pp \longrightarrow \tilde{\chi}_1^{\pm} + \tilde{\chi}_2^0 + 2$ jets $\longrightarrow 3\tau + 2$ jets $m\left(\tilde{\chi}_1^0\right) = 50$ GeV, $m\left(\tilde{\tau}_1\right) = 195$ GeV, $m\left(\tilde{\chi}_1^{\pm}\right) = m\left(\tilde{\chi}_2^0\right) = 200$ GeV	LSP050_Stau195_Chargino200_1M/
$pp \longrightarrow \tilde{\chi}_1^{\pm} + \tilde{\chi}_2^0 + 2$ jets $\longrightarrow 3\tau + 2$ jets $m\left(\tilde{\chi}_1^0\right) = 50$ GeV, $m\left(\tilde{\tau}_1\right) = 225$ GeV, $m\left(\tilde{\chi}_1^{\pm}\right) = m\left(\tilde{\chi}_2^0\right) = 400$ GeV	LSP050_Stau225_Chargino400_1M/
$pp \longrightarrow \tilde{\chi}_1^{\pm} + \tilde{\chi}_2^0 + 2$ jets $\longrightarrow 3\tau + 2$ jets $m\left(\tilde{\chi}_1^0\right) = 50$ GeV, $m\left(\tilde{\tau}_1\right) = 275$ GeV, $m\left(\tilde{\chi}_1^{\pm}\right) = m\left(\tilde{\chi}_2^0\right) = 500$ GeV	LSP050_Stau275_Chargino500_1M/
$pp \longrightarrow \tilde{\chi}_1^{\pm} + \tilde{\chi}_2^0 + 2$ jets $\longrightarrow 3\tau + 2$ jets $m\left(\tilde{\chi}_1^0\right) = 50$ GeV, $m\left(\tilde{\tau}_1\right) = 295$ GeV, $m\left(\tilde{\chi}_1^{\pm}\right) = m\left(\tilde{\chi}_2^0\right) = 300$ GeV	LSP050_Stau295_Chargino300_1M/
$pp \longrightarrow \tilde{\chi}_1^{\pm} + \tilde{\chi}_2^0 + 2$ jets $\longrightarrow 3\tau + 2$ jets $m\left(\tilde{\chi}_1^0\right) = 50$ GeV, $m\left(\tilde{\tau}_1\right) = 395$ GeV, $m\left(\tilde{\chi}_1^{\pm}\right) = m\left(\tilde{\chi}_2^0\right) = 400$ GeV	LSP050_Stau395_Chargino400_1M/
$pp \longrightarrow \tilde{\chi}_1^{\pm} + \tilde{\chi}_2^0 + 2$ jets $\longrightarrow 3\tau + 2$ jets $m\left(\tilde{\chi}_1^0\right) = 50$ GeV, $m\left(\tilde{\tau}_1\right) = 495$ GeV, $m\left(\tilde{\chi}_1^{\pm}\right) = m\left(\tilde{\chi}_2^0\right) = 500$ GeV	LSP050_Stau495_Chargino500_1M/
$pp \longrightarrow \tilde{\chi}_1^{\pm} + \tilde{\chi}_2^0 + 2$ jets $\longrightarrow 3\tau + 2$ jets $m\left(\tilde{\chi}_1^0\right) = 150$ GeV, $m\left(\tilde{\tau}_1\right) = 175$ GeV, $m\left(\tilde{\chi}_1^{\pm}\right) = m\left(\tilde{\chi}_2^0\right) = 200$ GeV	LSP150_Stau175_Chargino200_1M/
$pp \longrightarrow \tilde{\chi}_1^{\pm} + \tilde{\chi}_2^0 + 2$ jets $\longrightarrow 3\tau + 2$ jets $m\left(\tilde{\chi}_1^0\right) = 250$ GeV, $m\left(\tilde{\tau}_1\right) = 275$ GeV, $m\left(\tilde{\chi}_1^{\pm}\right) = m\left(\tilde{\chi}_2^0\right) = 300$ GeV	LSP250_Stau275_Chargino300_1M/
$pp \longrightarrow \tilde{\chi}_1^{\pm} + \tilde{\chi}_2^0 + 2$ jets $\longrightarrow 3\tau + 2$ jets $m\left(\tilde{\chi}_1^0\right) = 350$ GeV, $m\left(\tilde{\tau}_1\right) = 375$ GeV, $m\left(\tilde{\chi}_1^{\pm}\right) = m\left(\tilde{\chi}_2^0\right) = 400$ GeV	LSP350_Stau375_Chargino400_1M/
$pp \longrightarrow \tilde{\chi}_1^{\pm} + \tilde{\chi}_2^0 + 2$ jets $\longrightarrow 3\tau + 2$ jets $m\left(\tilde{\chi}_1^0\right) = 450$ GeV, $m\left(\tilde{\tau}_1\right) = 475$ GeV, $m\left(\tilde{\chi}_1^{\pm}\right) = m\left(\tilde{\chi}_2^0\right) = 500$ GeV	LSP450_Stau475_Chargino500_1M/

Table A.18: Signal simulated samples.

A.5 Main distributions at 13 TeV

This section features all the important analysis distributions for signal region and the other featured control regions.

Signal region

2 tight-isolated τ_h

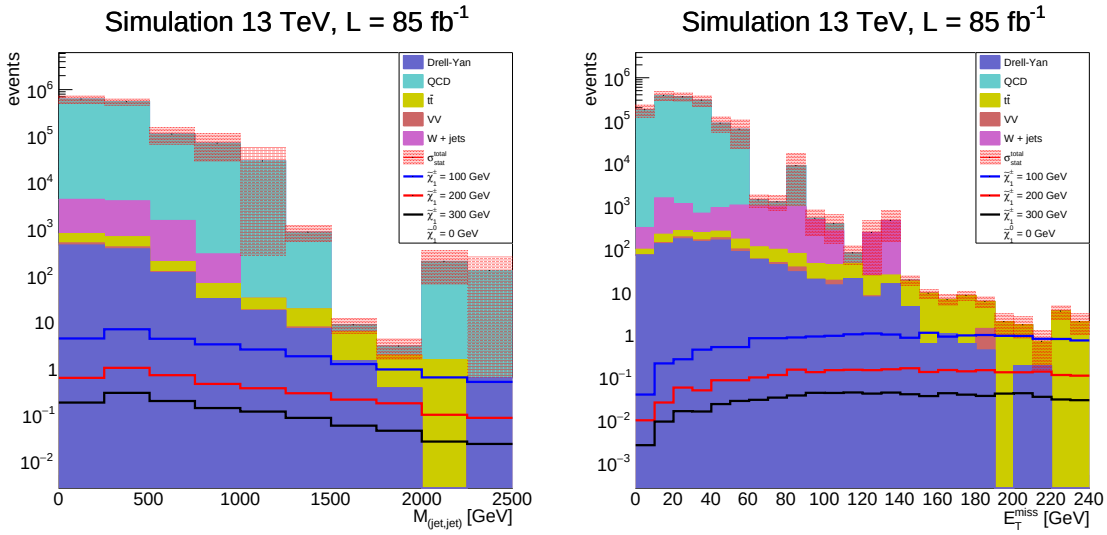

Figure A.1: (Left) Di-jet invariant mass distribution and (Right) and $\not{E}_T$ distribution of selected signal and all MC background samples in signal region.

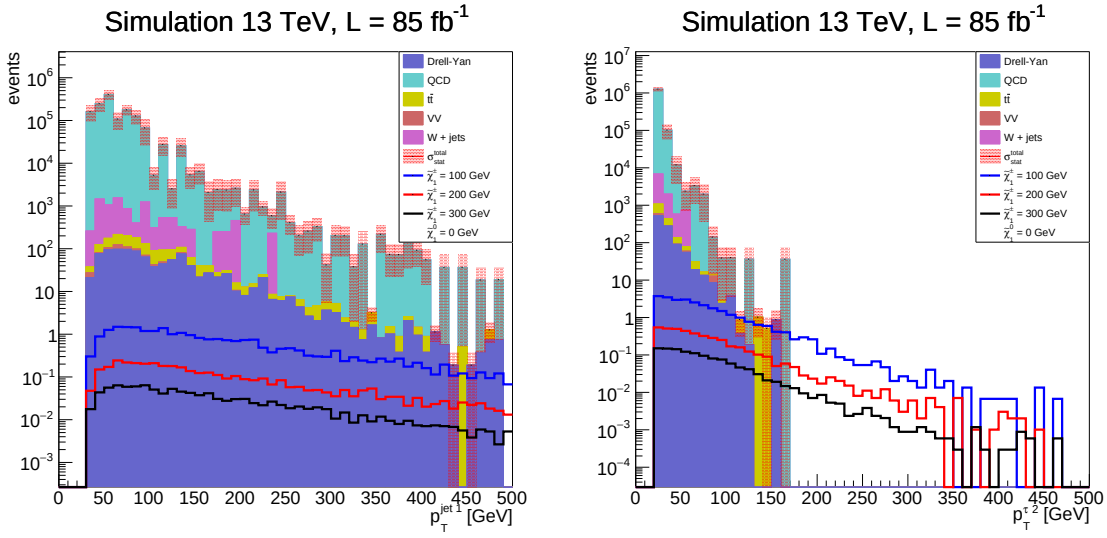

Figure A.2: (Left) Leading jet p_T distribution and (Right) and second leading τ_h p_T distribution of selected signal and all MC background samples in signal region.

Control region 2

2 tight-isolated τ_h, inverted VBF selection

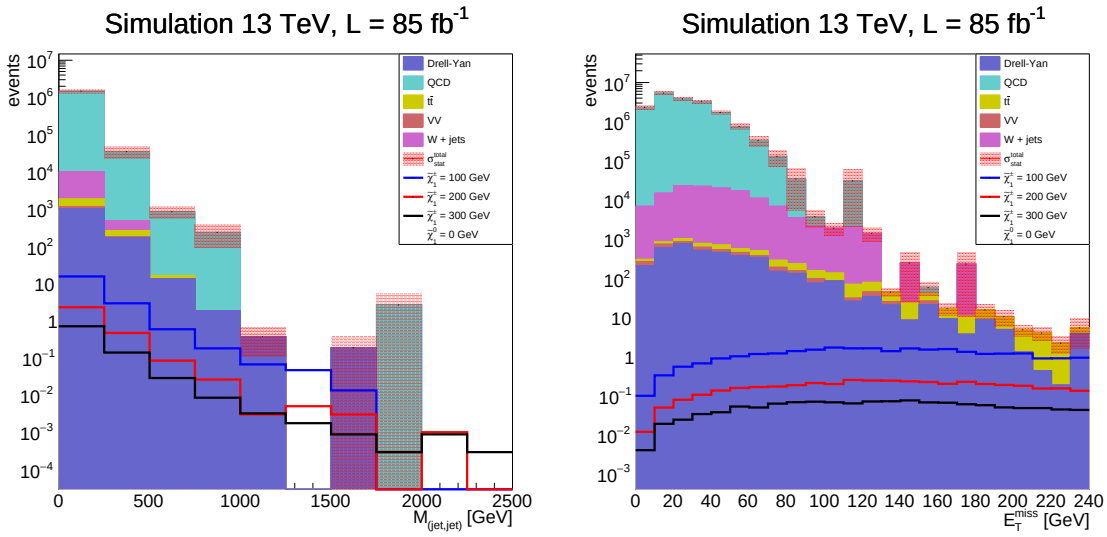

Figure A.3: (Left) Di-jet invariant mass distribution and (Right) and $\not{E}_T$ distribution of selected signal and all MC background samples in control region 2.

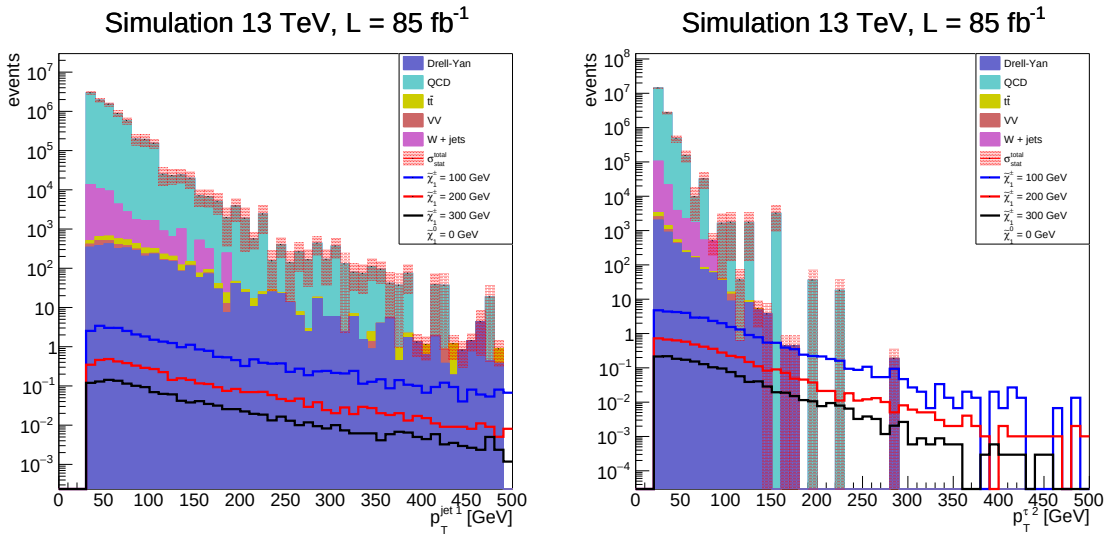

Figure A.4: (Left) Leading jet p_T distribution and (Right) and second leading τ_h p_T distribution of selected signal and all MC background samples in control region 2.

Control region 3

2 loose-isolated τ_h (inclusive)

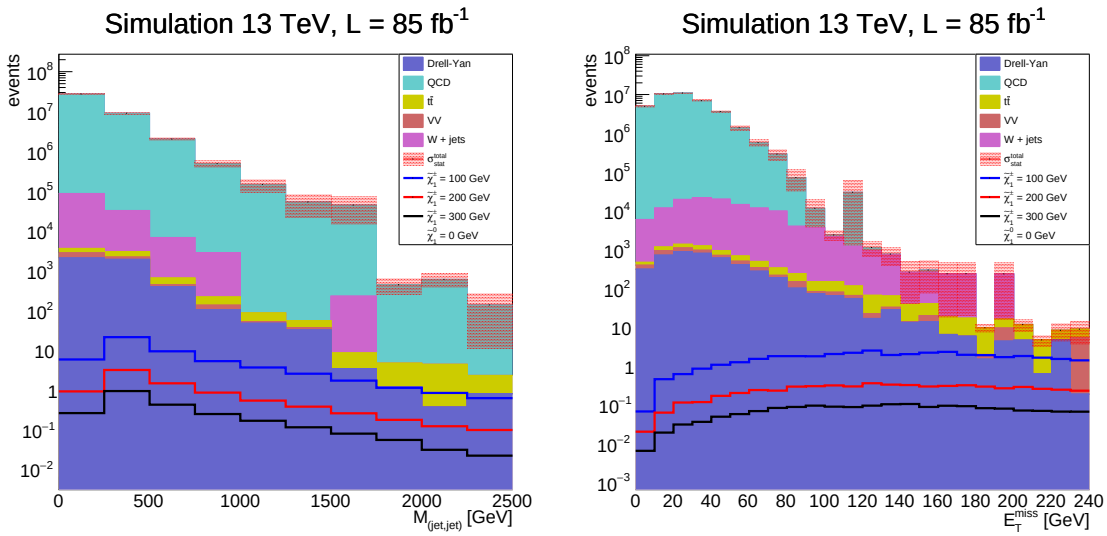

Figure A.5: (Left) Di-jet invariant mass distribution and (Right) and $\not{E}_{\mathrm{T}}$ distribution of selected signal and all MC background samples in control region 3.

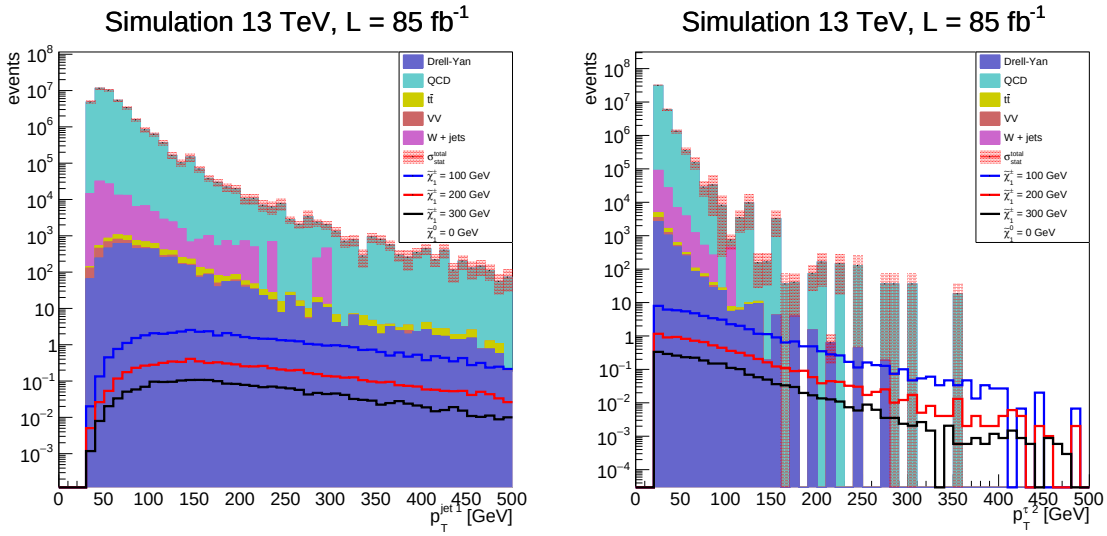

Figure A.6: (Left) Leading jet p_{T} distribution and (Right) and second leading τ_{h} p_{T} distribution of selected signal and all MC background samples in control region 3.

Control region 4

2 loose-isolated τ_h (inclusive), inverted VBF selection

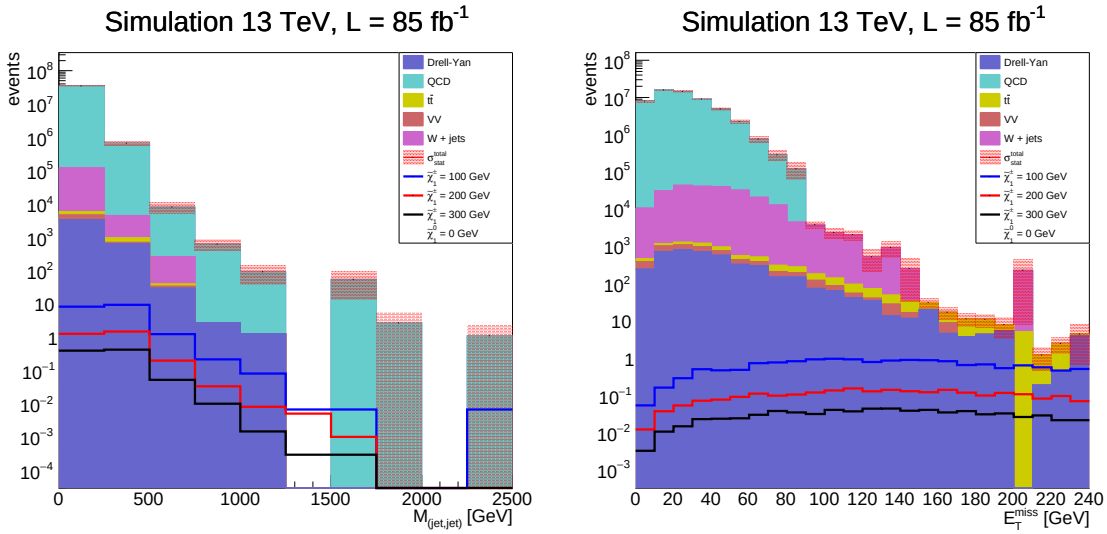

Figure A.7: (Left) Di-jet invariant mass distribution and (Right) and $\not{E}_T$ distribution of selected signal and all MC background samples in control region 4.

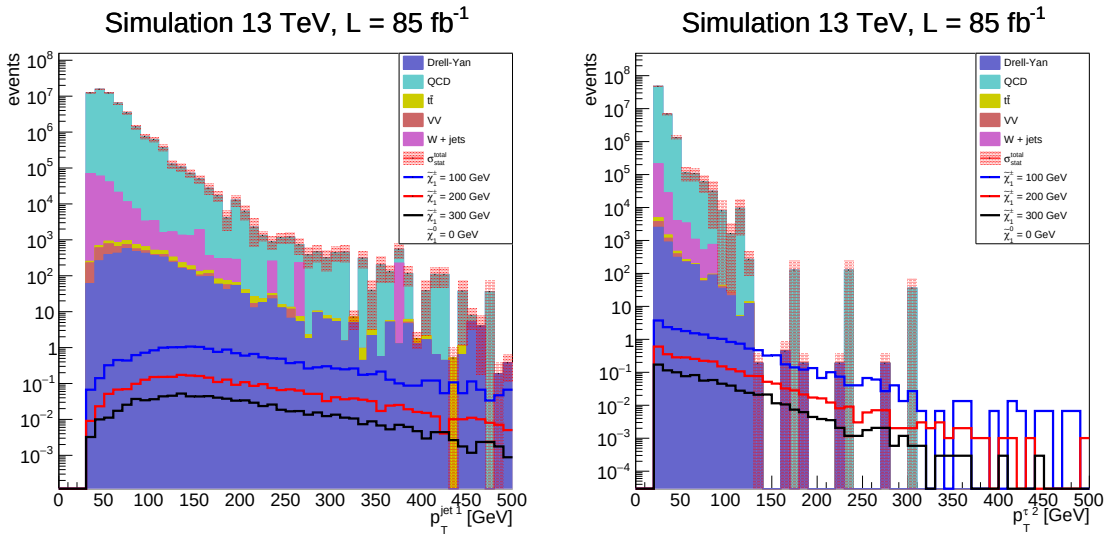

Figure A.8: (Left) Leading jet p_T distribution and (Right) and second leading τ_h p_T distribution of selected signal and all MC background samples in control region 4.

A.6 Signal cross-section limits at 13 TeV

This section shows the final results for the sensitivity study done on 13 TeV simulated samples as function of the invariant mass of the di-jet candidate, $\not{E}_{\mathrm{T}}$ and the reconstructed τ_{h} p_{T}. The different benchmark points were choses in term of different theoretical assumptions (fixed- and average-$\tilde{\tau}_1$-mass) and scenarios (uncompressed mass and compressed mass spectrum) for $\tilde{\chi}_1^{\pm}$ and $\tilde{\chi}_1^0$ masses of 100, 200, 300 400 and 500 GeV. Given the trivial assumption that the cross section limit is strictly correlated to the reconstructed τ_{h} p_{T} all the below results are shown considering a cut of 20 GeV over this variable.

Uncompressed scenario, fixed-$\tilde{\tau}_1$ mass

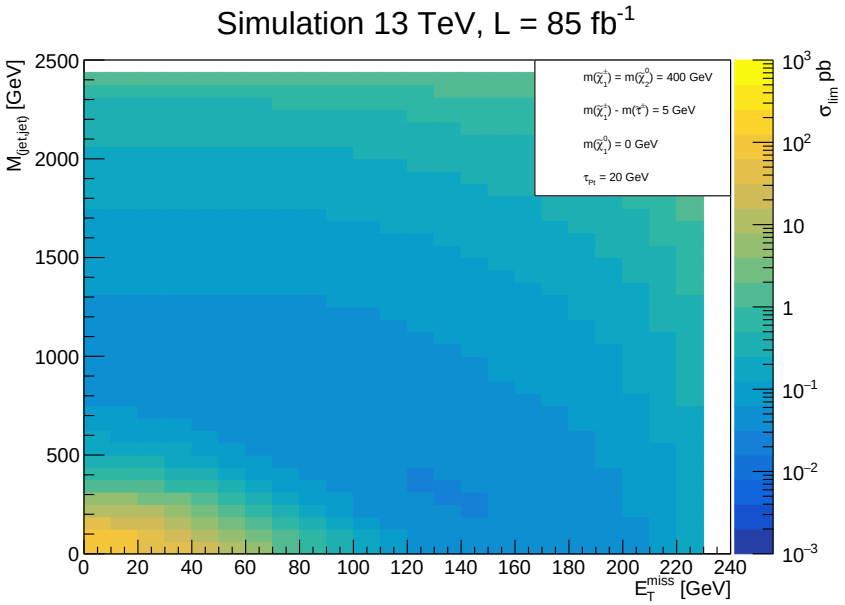

Figure A.9: Cross section limit as function of m_{jj} and $\not{E}_{\mathrm{T}}$ for $\mathrm{m}(\tilde{\chi}_1^{\pm}) = \mathrm{m}(\tilde{\chi}_2^0) = 400$ GeV, $\mathrm{m}(\tilde{\tau}_1) = 395$ GeV, and $\mathrm{m}(\tilde{\chi}_1^0) = 0$ GeV and an offline selection on $p_{\mathrm{T}}(\tau_{\mathrm{h}}) < 20$ GeV.

$m(\tilde{\chi}_1^\pm) = m(\tilde{\tau}_1) = 5$ GeV; $m(\tilde{\chi}_1^0) = 0$ GeV			
$\sigma_{lim}^{min} \pm (stat.) \pm (MCsyst.) \pm (VBFsyst.)$ [pb]	$m(\tilde{\chi}_1^\pm) = m(\tilde{\chi}_2^0)$ [GeV]	m_{jj} [GeV]	$\not{E}_T$ [GeV]
$0.033 \pm 0.002^{+0.003+0.001}_{-0.004-0.001}$	< 100	< 250	< 130
$0.033 \pm 0.002^{+0.003+0.001}_{-0.004-0.001}$	< 200	< 250	< 130
$0.034 \pm 0.002^{+0.003+0.001}_{-0.004-0.001}$	< 300	< 312.5	< 120
$0.030 \pm 0.001^{+0.002+0.001}_{-0.003-0.000}$	< 400	< 312.5	< 130
$0.030 \pm 0.001^{+0.003+0.001}_{-0.003-0.000}$	< 500	< 250	< 130

Table A.19: Cross section limit minimum reached at the given cuts for m_{jj}, $\not{E}_T$ and an increasing $\tilde{\chi}_1^\pm = \tilde{\chi}_2^0$ for the uncompressed mass spectra and fixed-$\tilde{\tau}_1$ mass benchmark point.

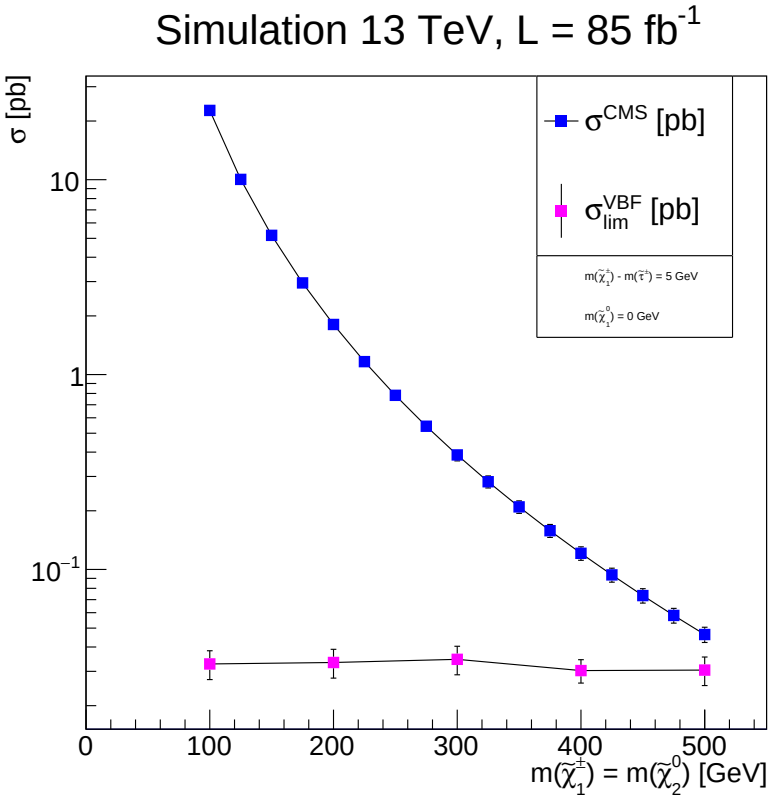

Figure A.10: Comparison between the cross section limit taken from the study over the uncompressed mass spectra and fixed-$\tilde{\tau}_1$ mass benchmark point and the official CMS cross sections calculated using the `resummino` code from B. Fuks et al with CTEQ6.6 and MSTW2008nlo90cl PDFs [112].

Compressed scenario, fixed-$\tilde{\tau}_1$ mass

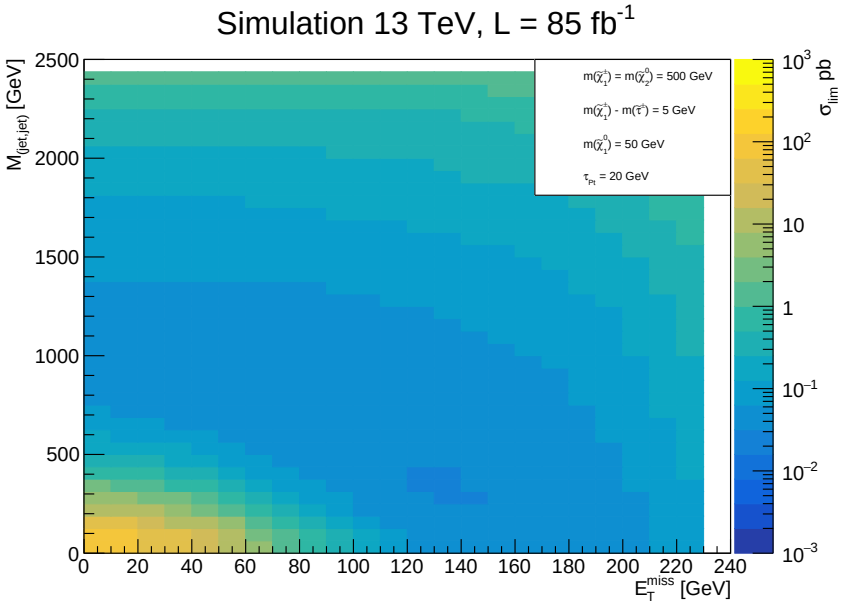

Figure A.11: Cross section limit as function of m_{jj} and $\not{E}_{\mathrm{T}}$ for $\mathrm{m}(\tilde{\chi}_1^{\pm}) = \mathrm{m}(\tilde{\chi}_2^0) = 500$ GeV, $\mathrm{m}(\tilde{\tau}_1) = 495$ GeV, and $\mathrm{m}(\tilde{\chi}_1^0) = 50$ GeV and an offline selection on $p_{\mathrm{T}}(\tau_{\mathrm{h}}) < 20$ GeV.

$\mathrm{m}(\tilde{\chi}_1^{\pm}) = \mathrm{m}(\tilde{\tau}_1) = 5$ GeV; $\mathrm{m}(\tilde{\chi}_1^{\pm})$ - $\mathrm{m}(\tilde{\chi}_1^0) = 50$ GeV			
$\sigma_{lim}^{min} \pm (stat.) \pm (MCsyst.) \pm (VBFsyst.)$ [pb]	$\mathrm{m}(\tilde{\chi}_1^{\pm}) = \mathrm{m}(\tilde{\chi}_2^0)$ [GeV]	m_{jj} [GeV]	$\not{E}_{\mathrm{T}}$ [GeV]
$0.033 \pm 0.002^{+0.003+0.001}_{-0.004-0.001}$	< 100	< 250	< 130
$0.033 \pm 0.002^{+0.003+0.001}_{-0.004-0.001}$	< 200	< 312.5	< 120
$0.033 \pm 0.001^{+0.002+0.001}_{-0.003-0.000}$	< 300	< 312.5	< 130
$0.031 \pm 0.001^{+0.002+0.001}_{-0.003-0.001}$	< 400	< 250	< 130
$0.030 \pm 0.001^{+0.002+0.001}_{-0.003-0.000}$	< 500	< 312.5	< 130

Table A.20: Cross section limit minimum reached at the given cuts for m_{jj}, $\not{E}_{\mathrm{T}}$ and an increasing $\tilde{\chi}_1^{\pm} = \tilde{\chi}_2^0$ for the compressed mass spectra and fixed-$\tilde{\tau}_1$ mass benchmark point.

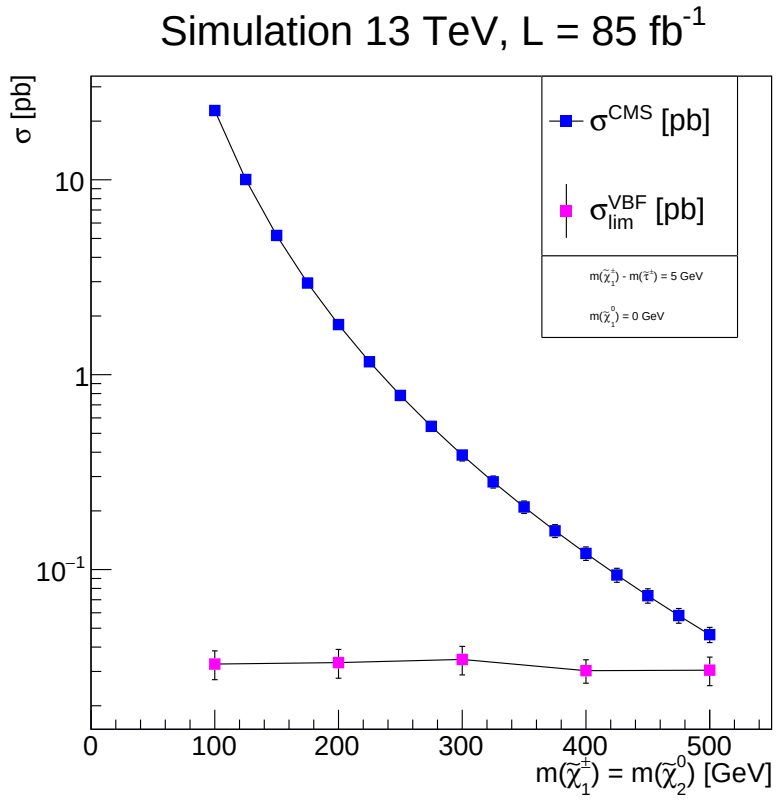

Figure A.12: Comparison between the cross section limit taken from the study over the compressed mass spectra and fixed-$\tilde{\tau}_1$ mass benchmark point and the official CMS cross sections calculated using the `resummino` code from B. Fuks et al with CTEQ6.6 and MSTW2008nlo90cl PDFs [112].

Uncompressed scenario, average-$\tilde{\tau}_1$ mass

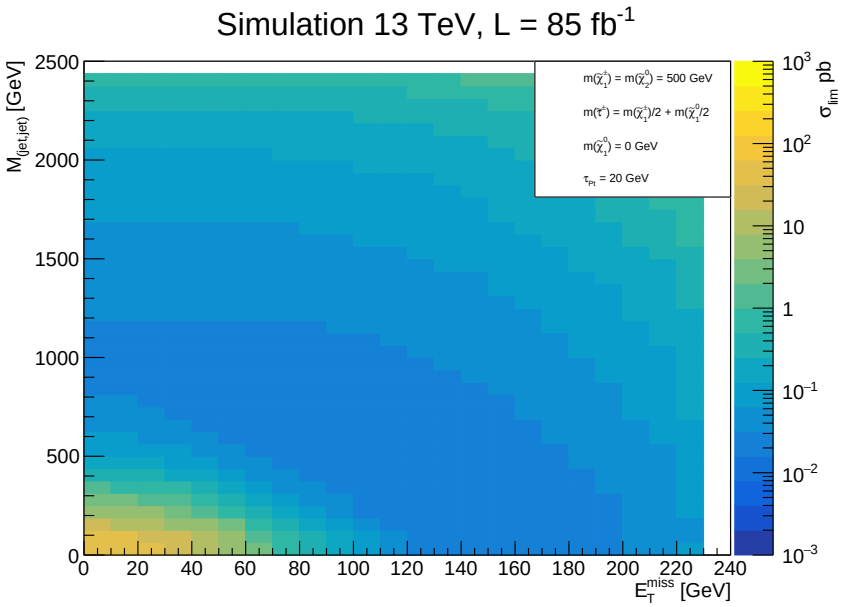

Figure A.13: Cross section limit as function of m_{jj} and $\not{E}_{\mathrm{T}}$ for $\mathrm{m}(\tilde{\chi}_1^{\pm}) = \mathrm{m}(\tilde{\chi}_2^0) = 500$ GeV, $\mathrm{m}(\tilde{\tau}_1) = 250$ GeV, and $\mathrm{m}(\tilde{\chi}_1^0) = 0$ GeV and an offline selection on $p_{\mathrm{T}}(\tau_{\mathrm{h}}) < 20$ GeV.

$\mathrm{m}(\tilde{\tau}_1) = 0.5\ \mathrm{m}(\tilde{\chi}_1^0) + 0.5\ \mathrm{m}(\tilde{\chi}_1^{\pm})$; $\mathrm{m}(\tilde{\chi}_1^0) = 0$ GeV			
$\sigma_{lim}^{min} \pm (stat.) \pm (MCsyst.) \pm (VBFsyst.)$ [pb]	$\mathrm{m}(\tilde{\chi}_1^{\pm}) = \mathrm{m}(\tilde{\chi}_2^0)$ [GeV]	m_{jj} [GeV]	$\not{E}_{\mathrm{T}}$ [GeV]
$0.083 \pm 0.005^{+0.007+0.003}_{-0.009-0.001}$	< 100	< 312.5	< 120
$0.036 \pm 0.002^{+0.003+0.001}_{-0.004-0.001}$	< 200	< 375	< 110
$0.024 \pm 0.001^{+0.002+0.001}_{-0.003-0.000}$	< 300	< 250	< 130
$0.019 \pm 0.001^{+0.002+0.001}_{-0.002-0.000}$	< 400	< 250	< 130
$0.017 \pm 0.001^{+0.002+0.001}_{-0.002-0.000}$	< 500	< 250	< 130

Table A.21: Cross section limit minimum reached at the given cuts for m_{jj}, $\not{E}_{\mathrm{T}}$ and an increasing $\tilde{\chi}_1^{\pm} = \tilde{\chi}_2^0$ for the uncompressed mass spectra and average-$\tilde{\tau}_1$ mass benchmark point.

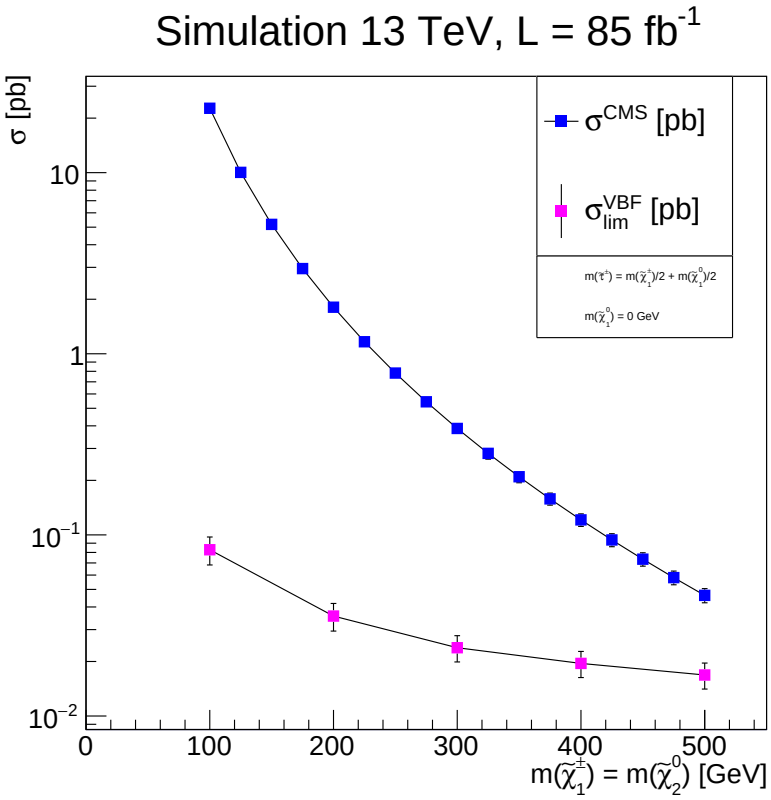

Figure A.14: Comparison between the cross section limit taken from the study over the uncompressed mass spectra and average-$\tilde{\tau}_1$ mass benchmark point and the official CMS cross sections calculated using the `resummino` code from B. Fuks et al with CTEQ6.6 and MSTW2008nlo90cl PDFs [112].

Compressed scenario, average-$\tilde{\tau}_1$ mass

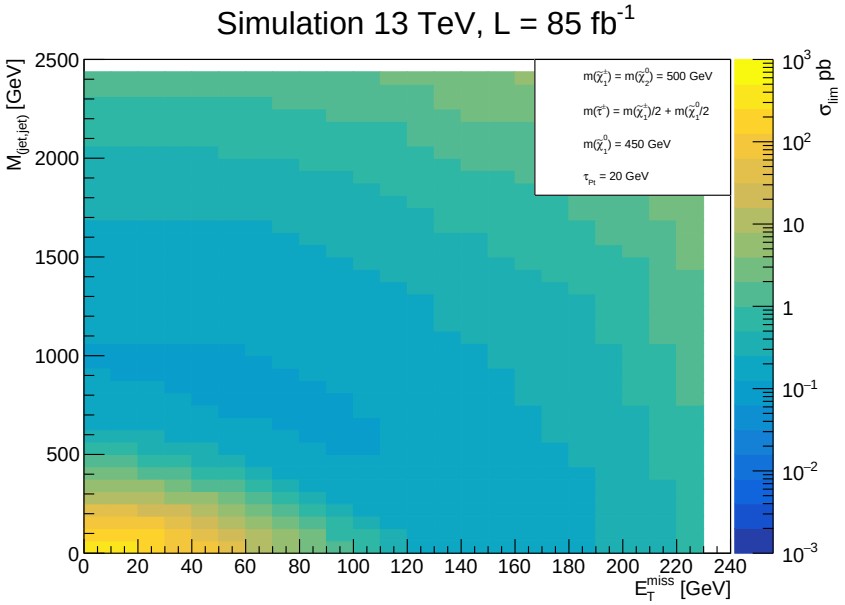

Figure A.15: Cross section limit as function of m_{jj} and $\not{E}_{\mathrm{T}}$ for $\mathrm{m}(\tilde{\chi}_1^{\pm}) = \mathrm{m}(\tilde{\chi}_2^0) = 500$ GeV, $\mathrm{m}(\tilde{\tau}_1) = 475$ GeV, and $\mathrm{m}(\tilde{\chi}_1^0) = 450$ GeV and an offline selection on $p_{\mathrm{T}}(\tau_{\mathrm{h}}) < 20$ GeV.

$\mathrm{m}(\tilde{\tau}_1) = 0.5\ \mathrm{m}(\tilde{\chi}_1^0) + 0.5\ \mathrm{m}(\tilde{\chi}_1^{\pm})$; $\mathrm{m}(\tilde{\chi}_1^{\pm})$ - $\mathrm{m}(\tilde{\chi}_1^0) = 50$ GeV			
$\sigma_{lim}^{min} \pm (stat.) \pm (MCsyst.) \pm (VBFsyst.)$ [pb]	$\mathrm{m}(\tilde{\chi}_1^{\pm}) = \mathrm{m}(\tilde{\chi}_2^0)$ [GeV]	m_{jj} [GeV]	$\not{E}_{\mathrm{T}}$ [GeV]
$0.153 \pm 0.011^{+0.012+0.005}_{-0.014-0.002}$	< 100	< 500	< 100
$0.148 \pm 0.011^{+0.014+0.005}_{-0.017-0.002}$	< 200	< 375	< 110
$0.157 \pm 0.011^{+0.013+0.005}_{-0.015-0.002}$	< 300	< 562.5	< 90
$0.150 \pm 0.011^{+0.014+0.005}_{-0.016-0.002}$	< 400	< 312.5	< 120
$0.115 \pm 0.007^{+0.010+0.004}_{-0.012-0.002}$	< 500	< 750	< 60

Table A.22: Cross section limit minimum reached at the given cuts for m_{jj}, $\not{E}_{\mathrm{T}}$ and an increasing $\tilde{\chi}_1^{\pm} = \tilde{\chi}_2^0$ for the compressed mass spectra and average-$\tilde{\tau}_1$ mass benchmark point.

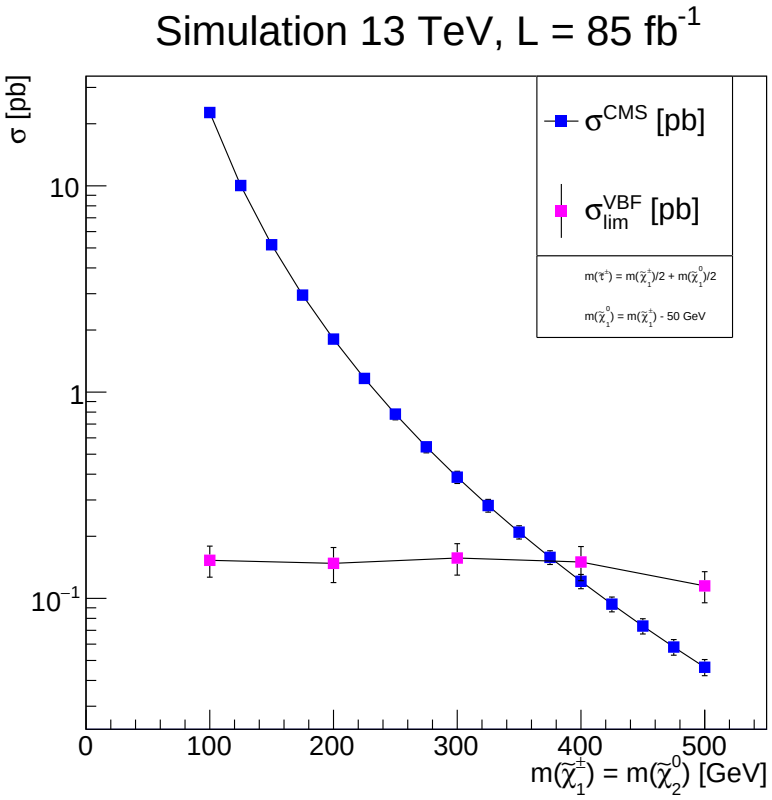

Figure A.16: Comparison between the cross section limit taken from the study over the compressed mass spectra and average-$\tilde{\tau}_1$ mass benchmark point and the official CMS cross sections calculated using the `resummino` code from B. Fuks et al with CTEQ6.6 and MSTW2008nlo90cl PDFs [112].

B Acknowledgments

More than study on Supersymmetry this PhD was my research for my adult life. I am proud of myself that I went over this very important chapter of my life. Many are the people that I met along the way during those years and several are the ones that I have to thank.

Thanks to Christian for his constant supervising, for the several lectures you gave until the end and for the music advices.

Thanks to Peter that took over the supervising in the last year of the thesis path.

Thanks to the members of the Committee that joined in the day of my Disputation.

Thanks to Jori and Benedict not only for being incredible friends but also for giving hospitality when I didn't have nowhere to go. To you two guys I owe you a bit on peace of mind during the summer-winter 2017. And thanks for all the advices you gave over the final steps of the thesis, also the legal ones.

Thanks to Simon, Marek and Lara for being the best adventure-misadventure partners of my last years. Thanks also to Anka and Ola for being the sidekicks of those amazing experiences. Many are the things we did and I will treasure each one of them.

Thanks to Sonja for all the time spent together. Thanks again for taking my defenses when injustice knocked at the door. And thanks one more time for the hospitality anytime I needed.

Thanks to the rest of the gang Pascal, Anne, Manu, Steffen, Franzi, Jacek, Tini, Daniel and Sasha. I owe you the best nights of the last year. I hope our friendship will grow stronger than ever.

Thanks to Steffi for our time in the name of lightness.

Thanks to Lumen for being the light beacon towards positiveness.

Thanks to Erk and Eva for their friendship, born in an unconventional way and steadily growing.

Thanks to the Hoffmann and Vanelderen family. You all belong to a big chunk of my heart.

Thanks to Adrian, Sam, Paolo for the preparation in the last steps of the PhD.

Thanks to my clan of gamers and long term friends, Ciucciamerlazzi. I wish us ten thousand years of silliness, irreverent talks, meaningless online battles and laughs.

Thanks to Jenni for the peace of mind, love and support she showed me during this last period. Blessed is the day we met.

A special thanks goes to my entire big family. I could not have not done any of this without your support, love, emergency parachutes, advices and countless moments together. I never felt far from all of you even though we are not living anymore in the same country. Forever yours.

Erklärung der Urheberschaft

Hiermit versichere ich an Eides statt, die vorliegende Dissertationsschrift selbst verfasst und keine anderen als die angegebenen Hilfsmittel und Quellen benutzt zu haben.

Die eingereichte schriftliche Fassung entspricht der auf dem elektronischen Speichermedium.

Die Dissertation wurde in der vorgelegten oder einer ähnlichen Form nicht schon einmal in einem früheren Promotionsverfahren angenommen oder als ungenügend beurteilt.

Ort, Datum Unterschrift

Bibliography

[1] H. Spiesberger, M. Spira, and P.M. Zerwas. The Standard model: Physical basis and scattering experiments. 2000. To be published in 'Scattering', P. Sabatier, editor. Academic Press, London, 2000.

[2] Georges Aad et al. Observation of a new particle in the search for the Standard Model Higgs boson with the ATLAS detector at the LHC. *Phys. Lett.*, B716:1–29, 2012.

[3] Serguei Chatrchyan et al. Observation of a new boson at a mass of 125 GeV with the CMS experiment at the LHC. *Phys. Lett.*, B716:30–61, 2012.

[4] Claudio Campagnari and Melissa Franklin. The Discovery of the top quark. *Rev. Mod. Phys.*, 69:137–212, 1997.

[5] N. Agafonova et al. Discovery of τ Neutrino Appearance in the CNGS Neutrino Beam with the OPERA Experiment. *Phys. Rev. Lett.*, 115(12):121802, 2015.

[6] Review of particle physics. *PHYSICAL REVIEW D*, 86(1):1504, 2012.

[7] W. de Boer, C. Sander, V. Zhukov, A. V. Gladyshev, and D. I. Kazakov. Egret excess of diffuse galactic gamma rays as tracer of dark matter. *Astron. Astrophys.*, 444:51, 2005.

[8] Anatoly Klypin, John Holtzman, Joel Primack, and Eniko Regos. Structure formation with cold plus hot dark matter. *Astrophys. J.*, 416:1–16, 1993.

[9] Gerard Jungman, Marc Kamionkowski, and Kim Griest. Supersymmetric dark matter. *Phys. Rept.*, 267:195–373, 1996.

[10] Y. Fukuda et al. Evidence for oscillation of atmospheric neutrinos. *Phys. Rev. Lett.*, 81:1562–1567, 1998.

[11] D. J. Miller and A. P. Morais. Supersymmetric SU(5) Grand Unification for a Post Higgs Boson Era. *JHEP*, 10:226, 2013.

[12] P. Athron, S. F. King, D. J. Miller, S. Moretti, and R. Nevzorov. LHC Signatures of the Constrained Exceptional Supersymmetric Standard Model. *Phys. Rev.*, D84:055006, 2011.

[13] Stephen P. Martin. A Supersymmetry primer. 1997. [Adv. Ser. Direct. High Energy Phys.18,1(1998)].

[14] Savas Dimopoulos and Howard Georgi. Softly Broken Supersymmetry and SU(5). *Nucl. Phys.*, B193:150–162, 1981.

[15] Savas Dimopoulos and David W. Sutter. The Supersymmetric flavor problem. *Nucl. Phys.*, B452:496–512, 1995.

[16] Nathaniel Craig. The State of Supersymmetry after Run I of the LHC. In *Beyond the Standard Model after the first run of the LHC Arcetri, Florence, Italy, May 20-July 12, 2013*, 2013.

[17] John Ellis. Supersymmetric Fits after the Higgs Discovery and Implications for Model Building. *Eur. Phys. J.*, C74:2732, 2014.

[18] A. Djouadi et al. The Minimal supersymmetric standard model: Group summary report. In *GDR (Groupement De Recherche) - Supersymetrie Montpellier, France, April 15-17, 1998*, 1998.

[19] V. Barger et al. Report of the SUGRA Working Group for run II of the Tevatron. 2000.

[20] Howard Baer, Chih-hao Chen, Manuel Drees, Frank Paige, and Xerxes Tata. Supersymmetry reach of Tevatron upgrades: The Large tan Beta case. *Phys. Rev.*, D58:075008, 1998.

[21] Howard Baer, Chih-hao Chen, Manuel Drees, Frank Paige, and Xerxes Tata. Probing minimal supergravity at the CERN LHC for large tan Beta. *Phys. Rev.*, D59:055014, 1999.

[22] A. Bartl, W. Majerotto, and W. Porod. Large Higgs boson exchange contribution in three-body neutralino decays. *Phys. Lett.*, B465:187–192, 1999.

[23] A. Djouadi and Y. Mambrini. Three body decays of SUSY particles. *Phys. Lett.*, B493:120–126, 2000.

[24] A. Djouadi, Y. Mambrini, and M. Muhlleitner. Chargino and neutralino decays revisited. *Eur. Phys. J.*, C20:563–584, 2001.

[25] Mike Lamont. The lhc from commissioning to operation. In Christine Petit-Jean-Genaz, editor, *Proceedings of the 2nd International Particle Accelerator Conference IPAC11*, pages 11 – 15, San Sebastián, Spain, 2011. `http://www.jacow.org/`.

[26] The Large Hadron Collider. Jan 2014.

[27] D. Marlow. CMS Luminosity Public Results, 2017. `https://twiki.cern.ch/twiki/bin/view/CMSPublic/LumiPublicResults`.

[28] G. Weiglein et al. Physics interplay of the LHC and the ILC. *Phys. Rept.*, 426:47–358, 2006.

[29] G. Aad et al. The ATLAS Experiment at the CERN Large Hadron Collider. *JINST*, 3:S08003, 2008.

[30] The CMS experiment at the CERN LHC. *JINST*, 3:S08004, 2008.

[31] Jr. Alves, A.Augusto et al. The LHCb Detector at the LHC. *JINST*, 3:S08005, 2008.

[32] K. Aamodt et al. The ALICE experiment at the CERN LHC. *JINST*, 3:S08002, 2008.

[33] O. Adriani et al. The LHCf detector at the CERN Large Hadron Collider. *JINST*, 3:S08006, 2008.

[34] G. Anelli et al. The TOTEM experiment at the CERN Large Hadron Collider. *JINST*, 3:S08007, 2008.

[35] S. Schael. The CMS silicon strip detector - mechanical structure and alignment system. *Nucl. Instrum. Meth.*, A511:52–57, 2003.

[36] Vardan Khachatryan et al. Jet energy scale and resolution in the CMS experiment in pp collisions at 8 TeV. *JINST*, 12(02):P02014, 2017.

[37] CMS, the Compact Muon Solenoid. Muon technical design report. 1997.

[38] S Chatrchyan et al. Performance of the CMS Drift Tube Chambers with Cosmic Rays. *JINST*, 5:T03015, 2010.

[39] *CMS The TriDAS Project Technical Design Report, Volume 1: The Trigger Systems*, volume 6 of *Technical Design Report CMS*. CERN, Geneva, 2000. CMS-TDR-006-1. CERN-LHCC-2000-038.

[40] Vardan Khachatryan et al. The CMS trigger system. *JINST*, 12(01):P01020, 2017.

[41] CMS: The computing project. Technical design report. 2005.

[42] C. Charlot. CMS software and computing. *Nucl. Instrum. Meth.*, A502:353–357, 2003.

[43] Particle-Flow Event Reconstruction in CMS and Performance for Jets, Taus, and MET. 2009.

[44] Commissioning of the Particle-flow Event Reconstruction with the first LHC collisions recorded in the CMS detector. 2010.

[45] Tracking and primary vertex results in first 7 TeV collisions. *CMS Physics Analysis Summary*, CMS-PAS-TRK-10-005, 2010.

[46] W. Erdman. Offline primary vertex reconstruction with deterministic annealing clustering. *CMS Internal Note*, 2011.

[47] S. Baffioni, C. Charlot, F. Ferri, D. Futyan, P. Meridiani, I. Puljak, C. Rovelli, R. Salerno, and Y. Sirois. Electron reconstruction in cms. *The European Physical Journal C*, 49(4):1099–1116, 2007.

[48] Wolfgang Adam, R. Frhwirth, Are Strandlie, and T. Todor. Reconstruction of Electrons with the Gaussian-Sum Filter in the CMS Tracker at the LHC. 2005.

[49] Andreas Hocker et al. TMVA - Toolkit for Multivariate Data Analysis. *PoS*, ACAT:040, 2007.

[50] Performance of electron reconstruction and selection with the cms detector in proton-proton collisions at s = 8 tev. *Journal of Instrumentation*, 10(06):P06005, 2015.

[51] Serguei Chatrchyan et al. Performance of CMS muon reconstruction in *pp* collision events at $\sqrt{s} = 7$ TeV. *JINST*, 7:P10002, 2012.

[52] M. Cacciari, G. P. Salam, and G. Soyez. The anti-kt jet clustering algorithm. *JHEP*, 0804:063, 2008.

[53] Jet Performance in pp Collisions at 7 TeV. 2010.

[54] CMS Collaboration. Pileup Jet Identification. 2013.

[55] Determination of Jet Energy Calibration and Transverse Momentum Resolution in CMS. *Journal of Instrumentation*, 6:P11002, 2011.

[56] Matteo Cacciari, Gavin P. Salam, and Gregory Soyez. The Catchment Area of Jets. *JHEP*, 04:005, 2008.

[57] Matteo Cacciari and Gavin P. Salam. Pileup subtraction using jet areas. *Phys. Lett.*, B659:119–126, 2008.

[58] Matteo Cacciari, Gavin P. Salam, and Gregory Soyez. The anti-k_{T} jet clustering algorithm. *Journal of High Energy Physics*, 2008(04):063, 2008.

[59] Serguei Chatrchyan et al. Identification of b-quark jets with the CMS experiment. *JINST*, 8:P04013, 2013.

[60] Performance of the b-jet identification in CMS. 2011.

[61] Performance Measurement of b tagging Algorithms Using Data containing Muons within Jets. Technical Report CMS-PAS-BTV-07-001, CERN, Geneva.

[62] D. Ferencek. Methods to apply b-tagging efficiency scale factors: Event reweighting using scale factors only. *CMS Twiki*, , 2015.

[63] Vardan Khachatryan et al. Performance of the CMS missing transverse momentum reconstruction in pp data at $\sqrt{s} = 8$ TeV. *JINST*, 10(02):P02006, 2015.

[64] Martin L. Perl et al. Evidence for Anomalous Lepton Production in e+ - e- Annihilation. *Phys. Rev. Lett.*, 35:1489–1492, 1975.

[65] K. A. Olive et al. Review of Particle Physics. *Chin. Phys.*, C38:090001, 2014.

[66] Serguei Chatrchyan et al. Performance of tau-lepton reconstruction and identification in CMS. *JINST*, 7:P01001, 2012.

[67] Vardan Khachatryan et al. Reconstruction and identification of lepton decays to hadrons and at CMS. *JINST*, 11(01):P01019, 2016.

[68] Georges Aad et al. Search for direct production of charginos and neutralinos in events with three leptons and missing transverse momentum in $\sqrt{s} = 7$ TeV *pp* collisions with the ATLAS detector. *Phys. Lett.*, B718:841–859, 2013.

[69] Georges Aad et al. Search for anomaly-mediated supersymmetry breaking with the ATLAS detector based on a disappearing-track signature in pp collisions at $\sqrt{s} = 7$ TeV. *Eur. Phys. J.*, C72:1993, 2012.

[70] Serguei Chatrchyan et al. Search for anomalous production of multilepton events in pp collisions at $\sqrt{s} = 7$ TeV. *JHEP*, 06:169, 2012.

[71] Howard Baer, B. W. Harris, and Mary Hall Reno. Next-to-leading order slepton pair production at hadron colliders. *Phys. Rev.*, D57:5871–5874, 1998.

[72] J. D. Bjorken. Rapidity gaps and jets as a new physics signature in very high-energy hadron hadron collisions. *Phys. Rev.*, D47:101–113, 1993.

[73] Bhaskar Dutta, Alfredo Gurrola, Will Johns, Teruki Kamon, Paul Sheldon, and Kuver Sinha. Vector Boson Fusion Processes as a Probe of Supersymmetric Electroweak Sectors at the LHC. *Phys. Rev.*, D87(3):035029, 2013.

[74] I. Hinchliffe and F. E. Paige. Measurements in SUGRA models with large tan beta at CERN LHC. *Phys. Rev.*, D61:095011, 2000.

[75] Kim Griest and David Seckel. Three exceptions in the calculation of relic abundances. *Phys. Rev.*, D43:3191–3203, 1991.

[76] Marcela Carena, Stefania Gori, Nausheen R. Shah, and Carlos E. M. Wagner. A 125 GeV SM-like Higgs in the MSSM and the $\gamma\gamma$ rate. *JHEP*, 03:014, 2012.

[77] Anindya Datta and Katri Huitu. Characteristic slepton signal in anomaly mediated SUSY breaking models via gauge boson fusion at the CERN LHC. *Phys. Rev.*, D67:115006, 2003.

[78] Vardan Khachatryan et al. Search for supersymmetry in the vector-boson fusion topology in proton-proton collisions at $\sqrt{s} = 8$ TeV. *JHEP*, 11:189, 2015.

[79] Riccardo A. Manzoni. Search for a higgs boson decaying into a di-tau pair in the double hadronic final state, 2014. PhD Thesis, Universita degli Studi di Milano Bicocca, Milan, Italy.

[80] Johan Alwall, Michel Herquet, Fabio Maltoni, Olivier Mattelaer, and Tim Stelzer. MadGraph 5 : Going Beyond. *JHEP*, 06:128, 2011.

[81] Stefano Frixione, Paolo Nason, and Carlo Oleari. Matching NLO QCD computations with Parton Shower simulations: the POWHEG method. *JHEP*, 11:070, 2007.

[82] Micha Czakon, Paul Fiedler, and Alexander Mitov. Total Top-Quark Pair-Production Cross Section at Hadron Colliders Through $O(\alpha\frac{4}{S})$. *Phys. Rev. Lett.*, 110:252004, 2013.

[83] Kirill Melnikov and Frank Petriello. Electroweak gauge boson production at hadron colliders through O(alpha(s)**2). *Phys. Rev.*, D74:114017, 2006.

[84] Ryan Gavin, Ye Li, Frank Petriello, and Seth Quackenbush. FEWZ 2.0: A code for hadronic Z production at next-to-next-to-leading order. *Comput. Phys. Commun.*, 182:2388–2403, 2011.

[85] John M. Campbell and R. K. Ellis. MCFM for the Tevatron and the LHC. *Nucl. Phys. Proc. Suppl.*, 205-206:10–15, 2010.

[86] K. Arnold et al. VBFNLO: A Parton level Monte Carlo for processes with electroweak bosons. *Comput. Phys. Commun.*, 180:1661–1670, 2009.

[87] K. Arnold et al. VBFNLO: A Parton Level Monte Carlo for Processes with Electroweak Bosons – Manual for Version 2.5.0. 2011.

[88] J. Pumplin, D. R. Stump, J. Huston, H. L. Lai, Pavel M. Nadolsky, and W. K. Tung. New generation of parton distributions with uncertainties from global QCD analysis. *JHEP*, 07:012, 2002.

[89] Pavel M. Nadolsky, Hung-Liang Lai, Qing-Hong Cao, Joey Huston, Jon Pumplin, Daniel Stump, Wu-Ki Tung, and C. P. Yuan. Implications of CTEQ global analysis for collider observables. *Phys. Rev.*, D78:013004, 2008.

[90] Torbjorn Sjostrand, Stephen Mrenna, and Peter Z. Skands. PYTHIA 6.4 Physics and Manual. *JHEP*, 05:026, 2006.

[91] N. Davidson, G. Nanava, T. Przedzinski, E. Richter-Was, and Z. Was. Universal Interface of TAUOLA Technical and Physics Documentation. *Comput. Phys. Commun.*, 183:821–843, 2012.

[92] S. Agostinelli et al. GEANT4: A Simulation toolkit. *Nucl. Instrum. Meth.*, A506:250–303, 2003.

[93] S. Abdullin, P. Azzi, F. Beaudette, P. Janot, and A. Perrotta. The fast simulation of the CMS detector at LHC. *J. Phys. Conf. Ser.*, 331:032049, 2011.

[94] W. Adam et al. PAT: The CMS physics analysis toolkit. *J. Phys. Conf. Ser.*, 219:032017, 2010.

[95] A. Pozdnyakov. The ntuple maker, 2014. `https://twiki.cern.ch/twiki/bin/view/CMS/UserCodeNWUntupleProducer`.

[96] Denis Rathjens. Jet energy calibration and a search for supersymmetry with vector boson fusion channel like sign di-hadronic-tau final states, 2015. PhD Thesis, Universität Hamburg, Hamburg, Germany.

[97] A. D. Martin, W. J. Stirling, R. S. Thorne, and G. Watt. Parton distributions for the LHC. *Eur. Phys. J.*, C63:189–285, 2009.

[98] Maria Ubiali. NNPDF1.0 parton set for the LHC. *Nucl. Phys. Proc. Suppl.*, 186:62–65, 2009.

[99] Michiel Botje et al. The PDF4LHC Working Group Interim Recommendations. 2011.

[100] G. Nanava and Z. Was. How to use SANC to improve the PHOTOS Monte Carlo simulation of bremsstrahlung in leptonic W boson decays. *Acta Phys. Polon.*, B34:4561–4570, 2003.

[101] Gabriela Miu and Torbjorn Sjostrand. W production in an improved parton shower approach. *Phys. Lett.*, B449:313–320, 1999.

[102] CMS Collaboration. Absolute Calibration of the Luminosity Measurement at CMS: Winter 2012 Update. 2012.

[103] O. Bouhali A. Cabrera A. C elik J. Cumalat C. Davis A. Delannoy N. Dhingra W. Flanagan A. Florez A. Gurrola W. Johns A. Kalsi D. Kim T. Kamon E. Luiggi S. Malik D. Marconi S. Maruyama K. Mazumdar A. Melo R. Montalvo M. Narain Y. Oh D. Rathjens C. Sander P. Sheldon J. Singh C. Avila, V. Bhatnagar and L. Vanelderen. Search for ewkinos produced in vector boson fusion processes with sqrt(s) = 8 tev. *CMS Analysis Note*, CMS-AN-12-321, 2014. Internal documentation.

[104] Tau identification in CMS. 2011.

[105] Sayipjamal Dulat, Tie-Jiun Hou, Jun Gao, Joey Huston, Jon Pumplin, Carl Schmidt, Daniel Stump, and C. P. Yuan. Intrinsic Charm Parton Distribution Functions from CTEQ-TEA Global Analysis. *Phys. Rev.*, D89(7):073004, 2014.

[106] Workbook for miniaod files. *CMS Wiki*, 2016. .

[107] Tauid for 13 tev run: recommendation from the tau pog. *CMS Wiki*, 2016. https://twiki.cern.ch/twiki/bin/viewauth/CMS/TauIDRecommendation13TeV, Topic revision: r15.

[108] Recommendation for using b-tag objects in physics analyses. *CMS Wiki*, 2016. https://twiki.cern.ch/twiki/bin/viewauth/CMS/BtagRecommendation, Topic revision: r23.

[109] Giovanni Punzi. Sensitivity of searches for new signals and its optimization. *eConf*, C030908:MODT002, 2003. [,79(2003)].

[110] Oliver S. Bruning. LHC luminosity and energy upgrade: A feasibility study. 2002.

[111] Nlo-nll wino-like chargino-neutralino (n2c1) cross sections. *CMS Wiki*, 2015. .

[112] Benjamin Fuks, Michael Klasen, David R. Lamprea, and Marcel Rothering. Precision predictions for electroweak superpartner production at hadron colliders with Resummino. *Eur. Phys. J. C*, 73:2480, 2013.